

Spring 5-2016

Study of Hybrid Magneto-Active Propellant Management Device for Slosh Damping

Leander Paul
Embry-Riddle Aeronautical University

Follow this and additional works at: <https://commons.erau.edu/edt>



Part of the [Aerodynamics and Fluid Mechanics Commons](#)

Scholarly Commons Citation

Paul, Leander, "Study of Hybrid Magneto-Active Propellant Management Device for Slosh Damping" (2016). *Doctoral Dissertations and Master's Theses*. 230.
<https://commons.erau.edu/edt/230>

This Thesis - Open Access is brought to you for free and open access by Scholarly Commons. It has been accepted for inclusion in Doctoral Dissertations and Master's Theses by an authorized administrator of Scholarly Commons. For more information, please contact commons@erau.edu.

STUDY OF HYBRID MAGNETO-ACTIVE PROPELLANT MANAGEMENT
DEVICE FOR SLOSH DAMPING

A Thesis

Submitted to the Faculty

of

Embry-Riddle Aeronautical University

by

Leander Paul

In Partial Fulfillment of the

Requirements for the Degree

of

Master of Science in Aerospace Engineering

May 2016

Embry-Riddle Aeronautical University

Daytona Beach, Florida

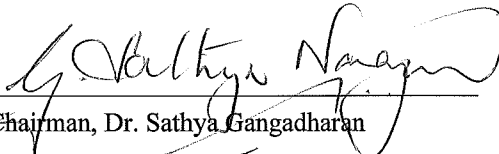
STUDY OF HYBRID MAGNETO-ACTIVE PROPELLANT MANAGEMENT
DEVICE FOR SLOSH DAMPING

by


Leander Paul

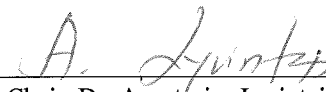
A Thesis prepared under the direction of the candidate's committee chairman, Dr. Sathya Gangadharan, Department of Mechanical Engineering, and has been approved by the members of the thesis committee. It was submitted to the School of Graduate Studies and Research and was accepted in partial fulfillment of the requirements for the degree of Master of Science in Aerospace Engineering.

THESIS COMMITTEE

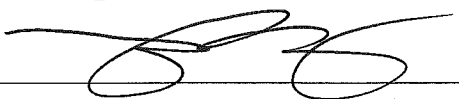

Chairman, Dr. Sathya Gangadharan


Co-Chair, Dr. Mark Ricklick

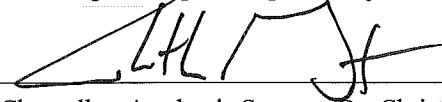

Member, Dr. Sirish Namilae


Department Chair, Dr. Anastasios Lyrintzis
or Graduate Program Coordinator, Dr. Eric Perrell

5/2/16
Date


Dean of College of Engineering, Dr. Maj Mirmirani

5/3/16
Date


Vice Chancellor, Academic Support, Dr. Christopher Grant

5/4/16
Date

ACKNOWLEDGMENTS

I thank the Lord Almighty for his blessings and protection. I thank my parents, Mr. Vincent Paul Rosario and Mrs. Ruby Kerolin Arokkia Mary for their love, support, guidance, encouragement and blessings in every step that I have taken in my life.

I would like to thank Embry-Riddle Aeronautical for making my dream a reality. I humbly thank my advisor Dr. Sathya Gangadharan for his guidance and endless support, my co-chair Dr. Mark Ricklick for his expert support and guidance in STAR-CCM+ and committee member Dr. Sirish Namilae for his research support.

I thank the faculty of Aerospace Engineering for imparting valuable knowledge and extending great support in terms of research especially Dr. Daewon Kim for research help and Dr. Virginie Rollin for granting me access to use the Scanning Electron Microscope with Energy Dispersive X-Ray Spectroscopy that was acquired with resources from the National Science Foundation (NSF) Major Research Instrumentation (MRI) grant # 1337742. An extended thank you to staff members Mr. Mike Potash for his expert assistance in electronics and Mr. Bill Russo for his assistance in experiment setup.

I would like to acknowledge Metglas[®] Inc. for providing the sample material used in this research, AEROTECH[®] for providing technical support and CD-Adapco[™] for providing license for their proprietary CFD software Star-CCM+. Finally, I would like to thank my colleague's Vijay Santhanam, Balaji Sivasubramanian, Priyadarshan Sundararaju, Nirmal Kumar Sanjeevi, Archana Krishnan and Soumya Das for their help and support in my research.

TABLE OF CONTENTS

LIST OF TABLES	vii
LIST OF FIGURES	viii
SYMBOLS	xi
ABBREVIATIONS	xii
ABSTRACT	xiii
1. Introduction	1
1.1. Slosh Phenomenon	1
1.2. Slosh Management	3
1.3. Magneto-Active Propellant Management Device (MAPMD)	7
2. Problem Statement	9
3. Material Selection	11
3.1. Requirements	11
3.2. Study of Commercially Available Materials	11
3.2.1. Stainless Steel	11
3.2.2. Metglas 2605SA1	12
3.2.3. Mu-Metal	12
3.2.4. Superalloy	13
3.2.5. Amumetal	13
3.2.6. Hipernom	13
3.3. Material Choice	13
3.4. Metglas 2605SA1 Surface Analysis	15
3.4.1. Metglas under Shear	16
3.4.2. Study of Cut Edges Under SEM	17
3.4.3. Element Composition	19
4. Experimental Approach	23
4.1. MAPMD Manufacturing Process	23
4.2. Slosh Test Bed Setup at ERAU	24
4.3. Data Acquisition	26
4.4. Experimental Test Cases and Test Parameters	27
4.5. Force on the Membrane	28
4.6. Experiment Setup	31
4.7. Load Cell Calibration	32

5. Computational Approach	34
5.1. Computational Phases	34
5.2. Modal Analysis.....	34
5.3. Computational Fluid Dynamics	36
5.3.1. About Computational Fluid Dynamics.....	36
5.3.2. Assumptions in Computational Fluid Dynamics	38
5.3.3. Modeling of Membrane and Tank	39
5.4. Importing Geometry into STAR-CCM+	41
5.5. Meshing Procedure	42
5.5.1. Mesh Resolution	43
5.5.2. Choice of Mesh	43
5.5.3. Volumetric Control	48
5.5.4. Overset Mesh	49
5.5.5. Regions and Boundary Conditions	50
5.6. Special Features in Meshing.....	52
5.6.1. Subtract	52
5.7. K-Epsilon Turbulence Model.....	54
5.8. Motion Model – Translation.....	55
5.9. DFBI.....	56
5.10. Eulerian Multiphase and VOF	57
5.10.1. Splitting of phases.....	58
5.11. Stopping Criteria	58
5.12. Report Generation	59
5.13. Convergence Criteria	60
5.14. Simulation Cases.....	60
5.15. Initializing the Simulation	62
6. Results and Discussion	63
6.1. Experimental Results	63
6.1.1. Signal De-Noising.....	63
6.1.2. Test Cases Results.....	63
6.1.3. Interpreting Experimental Results	64
6.2. Computational Results	69
6.2.1. Modal Analysis	69
6.2.2. Computational Fluid Dynamics Results.....	74

6.3. Comparison of Experimental and Computational Results	84
6.3.1. Free Slosh Case Comparison	84
6.3.2. Inactive Case Comparison.....	86
6.3.3. Active Case Comparison	88
6.4. Damping Calculation	90
7. Conclusion.....	94
8. Recommendations for Future Work.....	96
REFERENCES	97
A. Calculation of Logarithmic Decrement and Damping Ratio	100
B. Magnitude of Convergence for Simulation Variables.....	101
C. High Performance Computing (HPC) at ERAU	102

LIST OF TABLES

Table 3.1 Types of Metglas with their permeability	12
Table 3.2 Material property comparison.....	14
Table 3.3 Comparison of element composition between Manufacturer Specification and EDX data	22
Table 4.1 Test cases	28
Table 4.2 Test parameters	28
Table 5.1 Chronology of adopted paths in this research.....	45
Table 5.2 Test cases for mesh study	46
Table 5.3 Meshing parameters	54
Table 6.1 Summarization of Meshed and Solid Model Data.....	73
Table 6.2 Damping calculation summary for experimental low slosh condition	91
Table 6.3 Damping calculation summary for experimental high slosh condition	91
Table 6.4 Damping calculation summary for computational low slosh condition	91
Table 6.5 Damping calculation summary for computational high slosh condition	92
Table 6.6 Percentage increase in damping ratio from Free Slosh.....	92
Table 6.7 Logarithmic Decrement comparison between Magnetoactive Micro-Baffles and Magneto-Active Propellant Management Device	92
Table 8.1 Magnitude of convergence for simulation variables.....	101

LIST OF FIGURES

Figure 1.1 Momentum build-up of liquid in a cylindrical container under dynamic oscillating force condition.....	1
Figure 1.2 Slosh waves impacting on the container wall.....	2
Figure 1.3 Placement of passive PMD's along the container wall (Wolf, 2001).....	5
Figure 1.4 Examples of passive PMDs (Grayson, 2005 and Ryu et al., 2006)	6
Figure 1.5 Passive floating baffles inside a container (Ramsay, 2012)	7
Figure 1.6 Reconstructed floating Magnetoactive Micro-Baffles setup	8
Figure 2.1 Conceptual design	9
Figure 3.1 Scanning Electron Microscope FEI™ Quanta 650 present in Embry-Riddle Aeronautical University. SEM setup (left) and EDX setup (right)	15
Figure 3.2 Metglas strip cut under band saw (left) and a knife cutter (right)	16
Figure 3.3 Metglas 2605SA1 sheet bending under scissor cutting edges (left) and final cut with straight edges (right).....	17
Figure 3.4 SEM image of shear edge under band saw.....	18
Figure 3.5 SEM image of shear edge under Scissor	18
Figure 3.6 Comparison of surface element composition	19
Figure 3.7 EDX plot of individual element composition on the bright surface	20
Figure 3.8 EDX plot of individual element composition on the dull surface.....	21
Figure 4.1 Magneto-Active Propellant Management Device (MAPMD).....	24
Figure 4.2 Experimental fuel slosh test facility at ERAU	25
Figure 4.3 National Instruments myDAQ.....	27
Figure 4.4 Experimental setup to measure force on the membrane.....	30
Figure 4.5 Experiment setup to study damping characteristics of MAPMD	32
Figure 5.1 Slosh mode shapes for a fixed diaphragm (Green, et al., 2010)	35

Figure 5.2 Modal Analysis of Mesh and Solid Membrane	35
Figure 5.3 Meshed membrane modeled in CATIA	39
Figure 5.4 Close-up view of individual membrane strands	40
Figure 5.5 CAD geometry of cylinder tank	41
Figure 5.6 Meshed cylinder	44
Figure 5.7 Volume mesh models	45
Figure 5.8 Magnitude of convergence for number of volume mesh cells	47
Figure 5.9 Volumetric block	49
Figure 5.10 Individual strands united to become one whole membrane	51
Figure 5.11 Overset Mesh block between tank wall and membrane	52
Figure 5.12 Mesh in the (x y) plane of the cylinder.....	53
Figure 5.13 Mesh around the membrane	54
Figure 5.14 Motion model	55
Figure 5.15 DFBI settings for initial and active condition	57
Figure 5.16 Field Functions used for phase differentiation	58
Figure 5.17 List of plots.....	59
Figure 6.1 Comparison between Original and De-Noised signal	64
Figure 6.2 Experimental free slosh plot.....	65
Figure 6.3 Experimental inactive low amplitude slosh plot	66
Figure 6.4 Experimental inactive high amplitude plot.....	67
Figure 6.5 Experimental active low amplitude plot.....	68
Figure 6.6 Experimental active high amplitude plot.....	69
Figure 6.7 Mode 1 Displacements exhibited by Meshed Model (left) and Solid Model (right).....	70
Figure 6.8 Mode 2 Displacements exhibited by Meshed Model (left) and Solid Model (right).....	70
Figure 6.9 Mode 3 Displacements exhibited by Meshed Model (left) and Solid Model (right).....	71
Figure 6.10 Mode 4 Displacements exhibited by Meshed Model (left) and Solid Model (right).....	71
Figure 6.11 Mode 5 Displacements exhibited by Meshed Model (left) and Solid Model (right).....	72
Figure 6.12 Mode 6 Displacements exhibited by Meshed Model (left) and Solid Model (right).....	72

Figure 6.13 Frequency vs Stiffness comparison plot of Mesh and Solid MAPMD	74
Figure 6.14 Sample Residuals plot depicting simulation convergence	75
Figure 6.15 Tank motion during simulation plot	76
Figure 6.16 Computational free slosh comparison plot	77
Figure 6.17 Computational low amplitude inactive case study plot	78
Figure 6.18 Slosh peak in focus for computational low amplitude inactive case study	79
Figure 6.19 Computational low amplitude active case study plot	80
Figure 6.20 Slosh peak in focus for computational low amplitude active case study	81
Figure 6.21 Computational high amplitude case study plot	82
Figure 6.22 Slosh peak in focus for computational high amplitude case study	83
Figure 6.23 Computational high amplitude active case study plot	84
Figure 6.24 Low amplitude free slosh comparison plot	85
Figure 6.25 High amplitude free slosh comparison plot	86
Figure 6.26 Inactive case low amplitude comparison plot	87
Figure 6.27 Inactive case high amplitude comparison plot	88
Figure 6.28 Active case low amplitude comparison plot	89
Figure 6.29 Active case high amplitude comparison plot	89
Figure 8.1 Portable Batch System script	102
Figure 8.2 Console window terminal	103

SYMBOLS

\vec{v}	Velocity of the fluid particle
ρ	Density
$\Delta\vec{v}$	Change in velocity
g	Gravity
p	Pressure
μ	Dynamic viscosity
t	Time
a	Amplitude
f	Frequency
k	Coefficient of stiffness
m	Mass
F	Force
μ_0	Permeability of vacuum
N	Number of turns in electromagnet
I	Current
A	Area
l	Distance between membrane and bolt top surface

ABBREVIATIONS

PMD	Propellant Management Device
MAPMD	Magneto-Active Propellant Management Device
CFD	Computational Fluid Dynamics
AC	Alternating Current
EFI	Ed Fagan Inc.
LMA	Linear Motion Actuator
DAQ	Data Acquisition
MATLAB	Matrix Laboratory
SHM	Simple Harmonic Motion
CATIA	Computer Aided Three-Dimensional Interactive Application
CAD	Computer-Aided Design
3D	3-Dimensional
DNS	Direct Numerical Simulation
RANS	Reynolds-Averaged Navier-Stokes equation
DFBI	Dynamic Fluid Body Interaction
DOF	Degree Of Freedom
VOF	Volume Of Fluid
SEM	Scanning Electron Microscope
EDX	Energy Dispersive X-Ray Spectrometer

ABSTRACT

Author: Leander Paul

Title: Study of Hybrid Magneto-Active Propellant Management Device for Slosh Damping

Institution: Embry-Riddle Aeronautical University

Degree: Master of Science in Aerospace Engineering

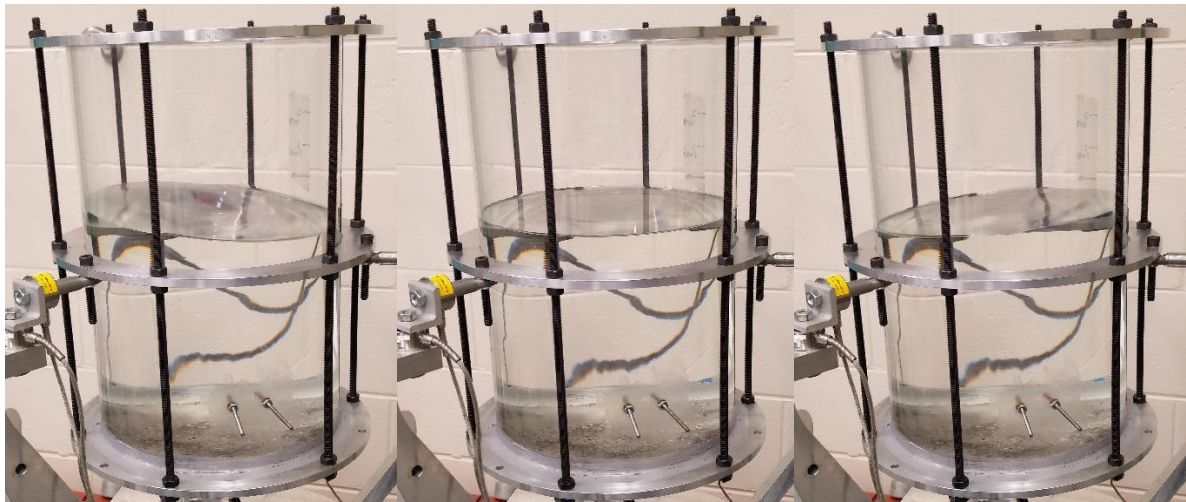
Year: 2016

Sloshing of liquid upon the application of an external force is a natural phenomenon as the free surface is allowed to move without any constraints. Study of slosh is an ongoing research for many decades and many novel inventions in Propellant Management Devices (PMDs) such as the rigid baffles and elastomeric membranes have been implemented to counteract the free surface effect in both passive and active manner. An innovative concept of a hybrid magneto-active membrane known as Magneto-Active Propellant Management Device (MAPMD) to actively control the free surface effect and reduce fuel slosh is explored in this research. Being a hybrid membrane, it would initially offer passive resistance to liquid motion and when activated would form a semi-rigid structural layer suppressing the free surface motion. This would eliminate the use of bulky baffle structures thereby decreasing the overall weight of the tank while increasing its volume. Two configurations of the membrane were made out of Metglas 2605SA1 alloy for this study and were tested for their effectiveness. To justify the hybrid membrane as a viable Propellant Management Device (PMD), proof-of-concept experiments involving low amplitude at 1.8 mm and high amplitude at 3.0 mm actuator displacement were carried out. Computational Fluid Dynamics (CFD) simulations were setup with parameters as that of the experiment to verify and validate the experimental setup. Results of this study demonstrated an overall improvement on the damping effectiveness from the existing hybrid active Propellant Management Device (PMD).

1. Introduction

1.1. Slosh Phenomenon

Study of liquid motion inside a partially filled container has been a keen interest among scientists for many a decades. Liquid surface which remains passive with little to no reaction changes its behavior drastically when the container experiences dynamic conditions. This motion of the free surface leads to the buildup of kinetic energy and momentum over time which is then transferred to the walls of the container upon contact Figure 1.1. This periodic transfer of energy can damage the structural integrity of the tank walls. In the field of engineering, this behavior of liquid free surface poses a major concern as it can affect the normal functioning of the container. Some examples of liquid contained within a dynamic body are naval fairing ships (including tankers), automobiles (motorcycles, cars, tanker trucks, etc.), aircrafts (of all kinds) and spacecraft (rocket/satellite tanks).



(a) Negative Force

(b) Neutral

(c) Positive Force

Figure 1.1 Momentum build-up of liquid in a cylindrical container under dynamic oscillating force condition

Uncontrollable movement of liquid free surface within a container is known as liquid slosh. In the field of Aerospace Engineering, liquid propellants have been used in missiles prior to space launch vehicles. Sloshing of liquid propellant has been identified as a major problem in tanks or vessels containing liquids especially when it is half filled, Figure 1.2. During the process of stage separation, the induced vibration is transferred into the fuel tank impacting forces and moments on the fuel (Varas et al., 2012). This causes the fuel to move around the tank in an uncontrolled oscillatory fashion which leads to the fuel slosh (Gangadharan, 2003).

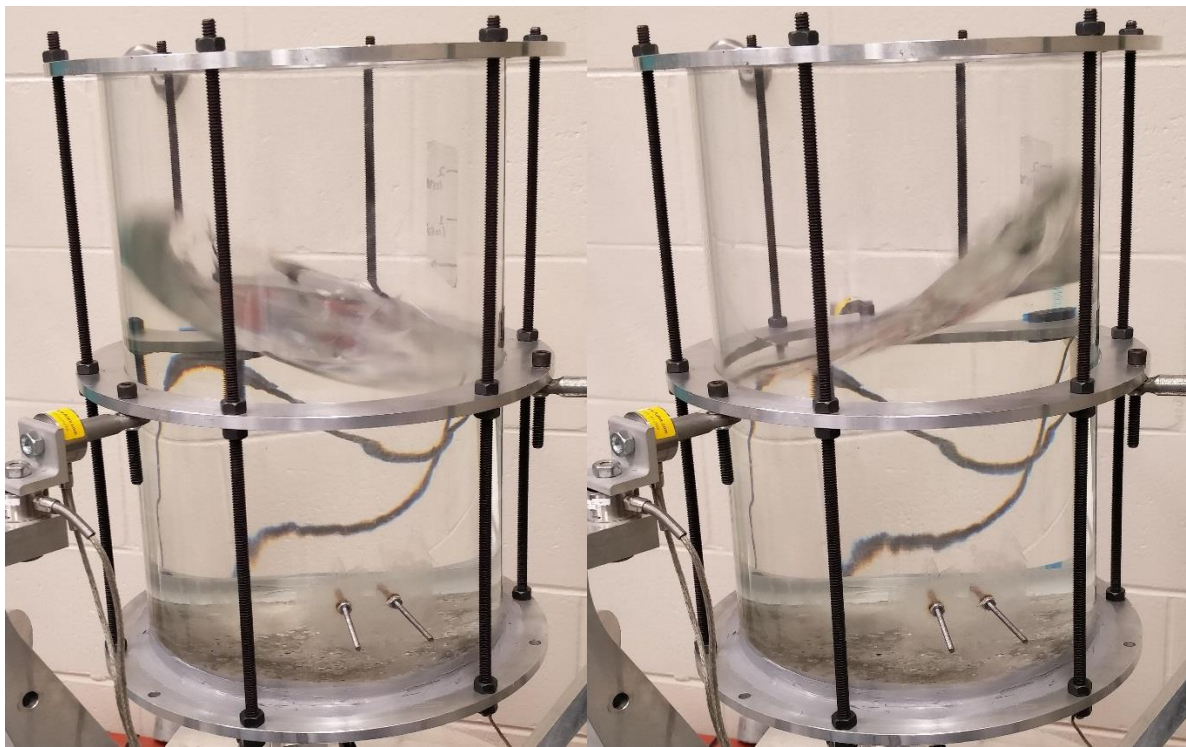


Figure 1.2 Slosh waves impacting on the container wall

The fuel moves as a bulk mass inside the tank wherein the upper portion of the fluid produces larger displacement than the lower portion. Propellant sloshing can also disturb the integrity of the space vehicle due to the buildup of large forces and moments when the liquid propellant is oscillating at its natural frequency in a partially filled tank

(Marsell et al., May 2009). This oscillation could result in structural components failing within the space vehicle or even deviation of the spacecraft from its intended flight path (Abramson, 1966). For example, in a spin stabilized spacecraft, the spinning motion plays a major role in stabilization (Chatman, 2008). In this type of spacecraft, the loss of rotational energy could prove disastrous for the vehicle itself as well as the payload (Marsell et al., 2009). The oscillating fuel is also influenced by the motion of the spacecraft itself and the reduction of fuel in the tank during travel and gravity. These frequencies are situational and are complex to model in an experimental setup.

Sloshing imparts unwanted forces and moments on the tank walls and produces oscillatory forces causing the spacecraft to wobble (Nutation). Nutation increases exponentially with time and if left unattended, can cause trajectory change leading to mission failure. In fact, there have been many reported failures of liquid propelled rockets since 1957 when the mission of Jupiter Intermediate Range Ballistic Missile 1-B was forced to terminate 93 seconds after launch. The recent one being the failure of Falcon One mission in 2007, a circular oscillation with increasing amplitude occurred at 4 minutes 20 seconds after launch that led to the blow up of the spacecraft. Fuel slosh has been a major concern in designing upper stages of spin stabilized space launch vehicles especially under micro-gravity conditions (Sivasubramanian et al., 2015).

1.2. Slosh Management

Liquid oscillations in spinning tanks have been studied in the past, where the response characteristics of oscillations is found to be different in both spinning and non-spinning fuel tanks (Gangadharan, 2003). Prediction of slosh motion becomes difficult and challenging especially when liquid shows boiling phenomena, as with cryogenic fuel,

or when structures like baffles are present inside the tank (Vreeburg, 2005). Anti-sloshing is the process of damping the remnant slosh waves from reaching higher amplitudes (Rosario et al., 2016). Previous experiments have been conducted to visualize the effects of sloshing in tanks varying in shape and size. Various ideas have been implemented to improve the damping of propellant oscillation.

Research has been carried out for many years in minimizing the energy dissipation of the fuel slosh and to prevent the impact of the slosh momentum on the fuel tanks (Loads, Structures Monograph 1968). Scientists have come up with novel inventions to counteract the forces and moments produced by the slosh known as propellant management devices (PMD), where PMD counteracts the forces and moments produced by the slosh (Sivasubramanian et al., 2015). PMD's can be classified into two types: Passive PMDs (such as diaphragm, baffle, etc.) and Active PMDs (such as acoustic membrane, hybrid-active membrane, etc.)

Passive PMDs positioned on the walls of the tanks not only lessen the slosh, but also provides structural integrity to the tank structure. As shown in Figure 1.3, these PMDs are inherently reliable as they do not have any moving parts and a baffle creates a barrier transverse to the fluid. Titanium is one such material used in the manufacturing of baffles which makes them well-suited with any liquid including water and is generally light in weight. Although baffles provide considerable damping effect on the slosh, it adds to the overall structural mass of the tank making it heavier, Figure 1.4 and thus reduces the amount of propellant carried by the tank (Benson et al., 2011).

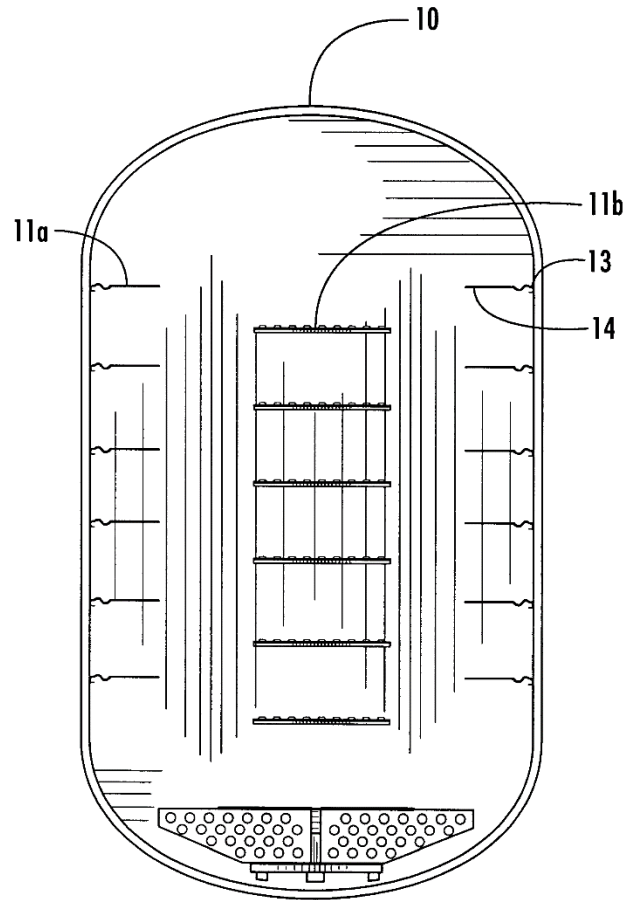


Figure 1.3 Placement of passive PMD's along the container wall (Wolf, 2001)

Active PMDs move along the fluid and are present either on top or within the fluid, Figure 1.5, bringing about restrictive behavior of slosh by the application of an external stimuli. Structures such as elastomeric membranes, resistant to hydrocarbons present in the fuel, are used in conjunction with a metallic substance in the manufacturing of active PMDs. Elastomeric membranes are again subdivided into active and passive membranes. Active membranes limit the rapid motion of the fluid under the influence of an external stimuli as they float on top of the liquid surface. An external magnetic source, although efficient, adds substantial mass to the tank and reduces the propellant payload capacity. On the other hand, passive membranes such as diaphragms, subdue slosh inside

the tank and this depends mainly on the elastic coefficient (Sivasubramanian et al., 2015). Baffles, either active or passive, deliver the essential damping on the slosh but largely adds to the weight of the tank. As weight is a major problem in the field of aeronautics, a compromise has to be found between slosh damping capability and overall structural mass of the tank (Rosario et al., 2016).

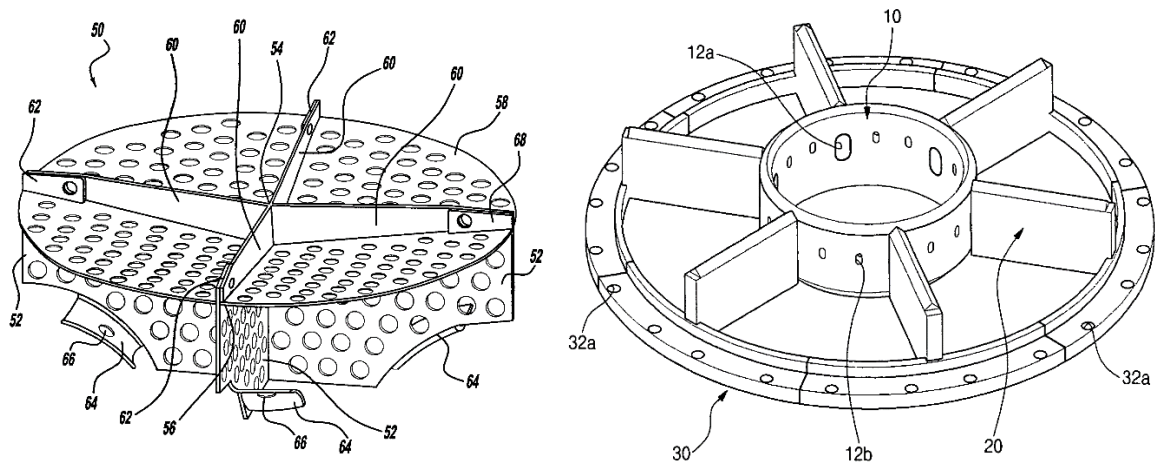


Figure 1.4 Examples of passive PMDs (Grayson, 2005 and Ryu et al., 2006)

Active PMDs move along the fluid and are present either on top or within the fluid, Figure 1.5, bringing about restrictive behavior of slosh by the application of an external stimuli. A recent research in Active PMDs involved counteracting the slosh wave frequency by producing opposing high frequency small amplitude waves (Leuva, 2011).

Structures such as elastomeric membranes, resistant to hydrocarbons present in the fuel, are used in conjunction with a metallic substance in the manufacturing of active PMDs. Elastomeric membranes are again subdivided into active and passive membranes. Active membranes limit the rapid motion of the fluid under the influence of an external

stimuli as they float on top of the liquid surface. An external magnetic source, although efficient, adds substantial mass to the tank and reduces the propellant payload capacity. On the other hand, passive membranes such as diaphragms, subdue slosh inside the tank and this depends mainly on the elastic coefficient (Sivasubramanian et al., 2015). Baffles, either active or passive, deliver the essential damping on the slosh but largely adds to the weight of the tank. As weight is a major problem in the field of aeronautics, a compromise has to be found between slosh damping capability and overall structural mass of the tank (Rosario et al., 2016).

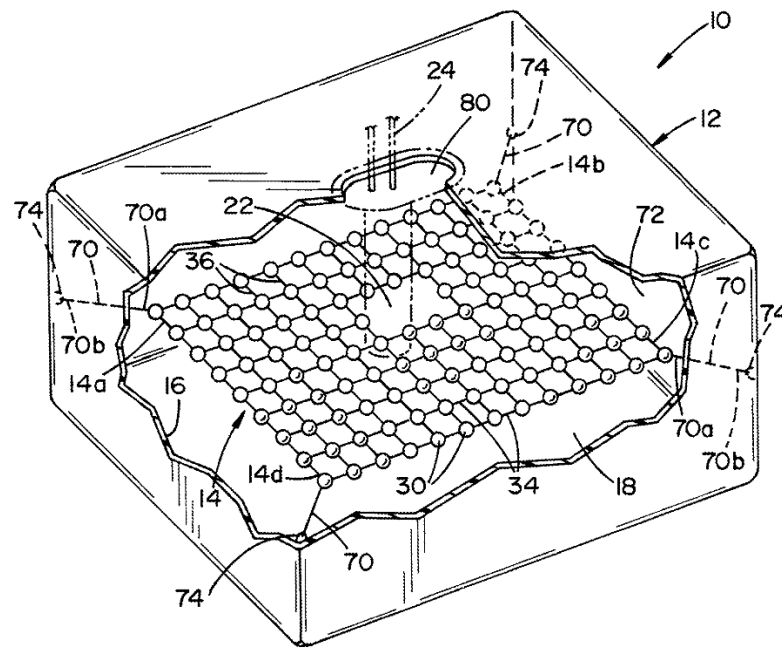


Figure 1.5 Passive floating baffles inside a container (Ramsay, 2012)

1.3. Magneto-Active Propellant Management Device (MAPMD)

The ideation of active control of a hybrid membrane in a slosh tank has been adopted from previous researches that involved implementing floating baffles (Sivasubramanian et al., 2015). These baffles absorb the kinetic energy from the liquid motion and transmit it within the baffles when they collide with one another thus

containing and dispersing the energy evenly, Figure 1.6. A study of liquid slosh on boundary element models has shown that the placement of baffle plays a major role in the reduction of slosh (Santhanam, 2014).



Figure 1.6 Reconstructed floating Magnetoactive Micro-Baffles setup

The concept of floating baffles is incorporated in the modeling of MAPMD. The effective change in diaphragm shape according to variation in magnetic field allows for the damping of free surface effect and slosh at various amplitudes, fill levels and also at various attitudes of the spacecraft in the fuel tank of which the system would be adapted. The versatile shape adaptability of this system makes it very effective when used in microgravity applications (Sivasubramanian et al., 2015). Documentation of the challenges encountered in the design, construction and testing stages and also the proof-of-concept experiments are provided.

2. Problem Statement

Over the years, slosh damping methods has taken a major stride, from big and bulky baffles placed along the tank walls to the floating micro-baffles on the liquid surface. Hence a trend of decrease in size and weight is seen throughout the years. Although smaller in size, complete coverage of liquid surface within the tank is not achieved. Under micro-gravity conditions, passive baffle lining along the wall provides little to no control over liquid movement. In conjunction with the trend in baffle design, a new hybrid baffle design addressing this issue is to be investigated.

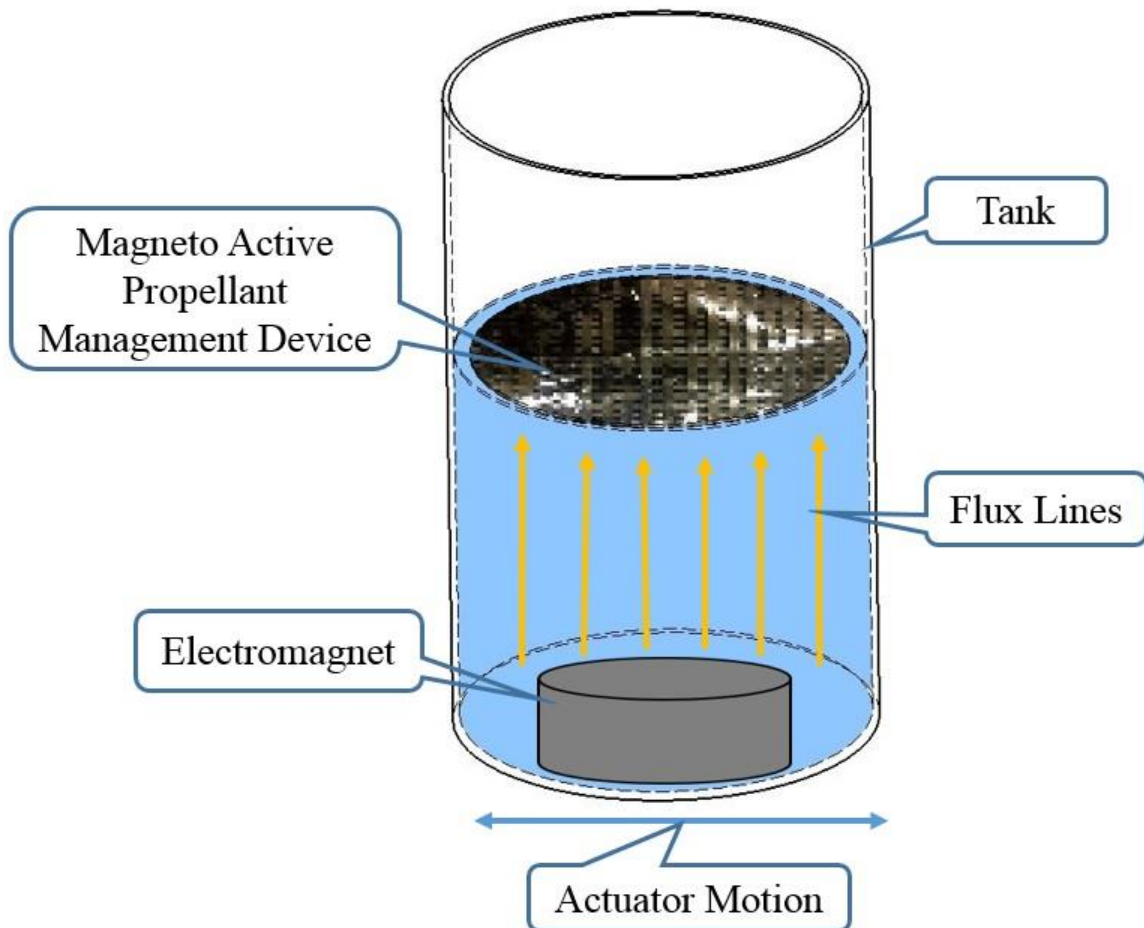


Figure 2.1 Conceptual design

The main goal of this research is to control the liquid free surface effect by the formation of a thin semi-rigid structural layer on the entire liquid surface and the study of the proposed Magneto-Active Propellant Management Device (MAPMD) as a viable hybrid Propellant Management Device (PMD) as shown in Figure 2.1. Theoretically under micro-gravity conditions, this would act as a lid on top of the liquid surface controlling the liquid body movement in the tank.

The main goal of this research is achieved in three steps. The first step involves the theoretical study of materials and explanation for material selection based on the requirements of this research. The second step involves the construction of MAPMD and experimental tests to study the effectiveness of MAPMD design in reducing the said free surface effect. The third step is to replicate the experiment in a CFD environment and study the validity of the experimental setup.

3. Material Selection

3.1. Requirements

This research involves a small scale simulation of a cylindrical tank partially filled with water instead of hydrazine undergoing an excitation thereby replicating a real life scenario of the effects experienced in a cylindrical tank of a spacecraft. To study the effectiveness of hybrid propellant management device proposed in this case, an external magnetic field is applied. Assuming that the magnetic field is applied from outside the tank wall in a real life scenario, the flux must penetrate the tank walls and reach the membrane losing its intensity with distance from its point of origin to the membrane surface. For the membrane to achieve its designed purpose, it must have the ability to support the formation of magnetic field to even the lowest of intensity. In addition to permeability, the material must also be thin and light weight so as to form a layer on top of the liquid surface and be flexible enough to move along with the liquid motion.

3.2. Study of Commercially Available Materials

One of the main criteria for this research requires a highly permeable material. Certain materials, their properties and composition that were considered into for this research are listed below:

3.2.1. Stainless Steel

In micro-baffles experiment conducted at ERAU test facility, stainless steel (martensitic, annealed) was used. Martensitic stainless steel of 400 series, is composed of 11.5%-18% chromium with greater percentage of carbon level. It undergoes heat treatment for hardness and strength levels. A typical 420 stainless steel is magnetic in

both annealed and hardened conditions. The relative permeability of this material varies from 750-950 (H/m). It is also highly corrosive resistant and readily available (Samal et al., 2001).

3.2.2. Metglas 2605SA1

Metglas 2605SA1 is an iron based alloy used in power transformers, motors and devices requiring high permeability. The maximum permeability (annealed) is given as 600,000 (H/m) (Mouhamad et al., 2011). Different Metglas materials, their major constituent and permeability are given in Table 3.1.

Table 3.1 Types of Metglas with their permeability

METGLAS TYPES AND PROPERTIES			
S.No	Material Type	Major Constituent	Permeability μ (H/m) (annealed)
1	Metglas 2605SA1	Iron	600,000
2	Metglas 2605S3A	Iron	35,000
3	Metglas 2826MB	Iron-Nickel	800,000
4	Metglas 2714A	Cobalt	1,000,000

3.2.3. Mu-Metal

Mu-Metal is another material with a composition of 77% nickel, 16% iron, 5% copper and 2% chromium or molybdenum. The magnetic permeability of Mu-Metal is enhanced 40 times when annealed with hydrogen. The biggest advantage of Mu-Metal is its ductility, allowing it to be drawn into sheets. The magnetic permeability of Mu-Metal varies from 80,000-200,000 (H/m) (Dong et al., 2006).

3.2.4. Supermalloy

A specially processed 80% nickel (Ni), 20% iron (Fe) with molybdenum (Mo) alloy is called Supermalloy. Built especially for pulse transformers and ultra-sensitive magnetic amplifiers, this alloy has permeability in the range of 40,000-100,000 (H/m) (Neamțu et al., 2012).

3.2.5. Amumetal

Another high magnetic permeable material to get most magnetic shields, Amumetal is processed with 80% nickel-iron based alloy having permeability in the ranges of 60,000-400,000 (H/m). Amumetal is divided into four types like Amumetal (80% nickel), Amumetal (48% nickel), Cryoperm 10 and ultra-low carbon steel (Ginsburg et al., 2009).

3.2.6. Hipernom

Hipernom is an 80% nickel based alloy along with 15% iron and 4.20% molybdenum. It is a soft magnetic alloy with high permeability. Hipernom is also known as EFI alloy 79. This alloy is used in high quality motor laminations and stepping motors. The permeability of Hipernom is 230,000 (H/m) (Rosario et al., 2016).

3.3. Material Choice

This research is conducted in a closed laboratory environment and for experimental purposes, a material that is non-toxic and safe to handle is to be considered. From the abstract study in a theoretical point of view, Metglas was found to possess favorable properties required for this research such as high magnetic permeability and

small thickness. However, not all of Metglas alloys mentioned in the study were readily available for a comparative study. Based on information and positive feedback from the manufacturer Metglas Inc, Metglas 2605SA1 was considered for this research. As water is used in place of hydrazine due to similar properties and research environment, performance of the Metglas alloy should theoretically hold true for both liquids.

Table 3.2 Material property comparison

Material	Magnetic Permeability (H/m) (max)	Tensile Strength	Resistivity	Modulus of Elasticity	Comments
HY-MU 80	200,000	232 MPa	580 micro ohm-mm	0.217 GPa	-
Permalloy	300,000	551.5 MPa	580 micro ohm-mm	-	Duty cycle is less due to low hardness value.
Co-NETIC	450,000	441.26 MPa	550 micro ohm-mm	172.36 GPa	Higher hardness, higher modulus of elasticity therefore duty cycle is high
Hipernom	230,000	552-620 MPa	-	-	-
Metglas 2714a	1,000,000	1000-2000 MPa	1420 micro ohm -mm	100-110 GPa	Higher hardness, higher modulus of elasticity therefore duty cycle is high. Due to higher resistivity, less eddy losses.

3.4. Metglas 2605SA1 Surface Analysis

Surface Analysis and element composition of Metglas alloy was performed using Scanning Electron Microscope (SEM) with Energy Dispersive X-ray Spectrometer (EDX) available at Embry-Riddle Aeronautical University as shown in Figure 3.1.



Figure 3.1 Scanning Electron Microscope FEI™ Quanta 650 present in Embry-Riddle Aeronautical University. SEM setup (left) and EDX setup (right)

Manufacturing process of hybrid membrane involved cutting of Metglas sheet into thin strips of dimensions 24 x 1 cm each. Resembling that of a sheet metal, different cutting techniques were tried to obtain a cut with even edges avoiding any burrs or bent edges in the process. Difference between the edges produced by the different cutting techniques were studied under SEM.

Either sides of the Metglas sheet has different texture, one side has a bright and shiny texture while the other one has a dull texture. Small samples of either sides were analyzed under EDX to find if there is any difference in element composition from the one specified by the manufacturer.

3.4.1. Metglas under Shear

Metglas sheet was initially cut using a Band saw. This cutting method did not produce even edges and the edges appeared to be rough, uneven and broken at several places. The strip was bent at many locations with a lot of visible macro tears.

Razor sharp knife was then used for the cutting process. This attempt was once again futile with the sheet bending along the cutting edge and the resultant product resembling that of the Band saw product but with less tears, Figure 3.2.

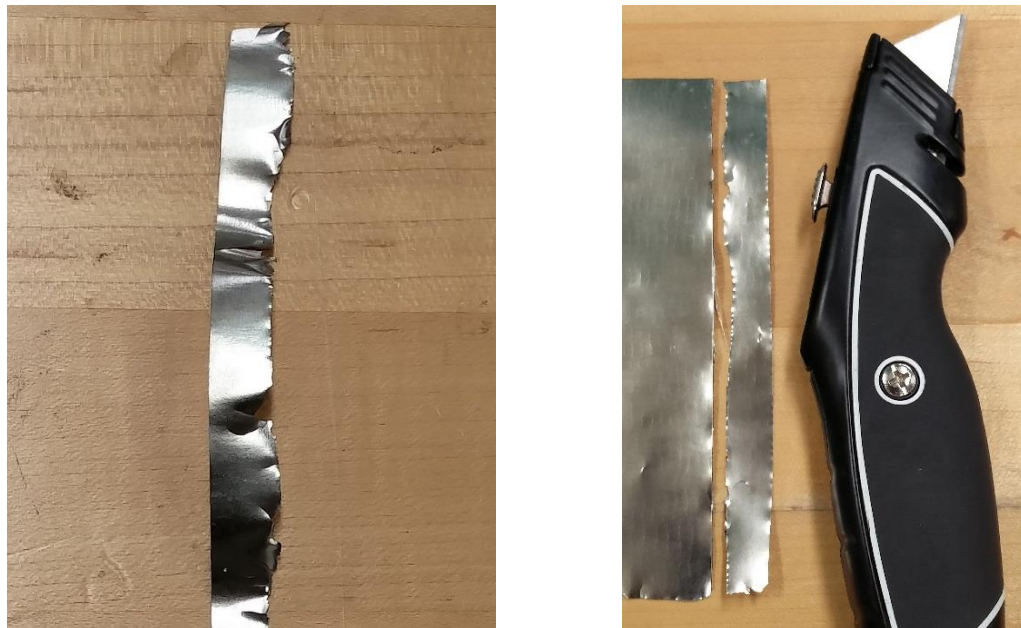


Figure 3.2 Metglas strip cut under band saw (left) and a knife cutter (right)

Final attempts to cut the sheet were made with scissor. This was a tedious process owing to the thickness of the sheet. The sheet would bend at the scissor shearing edges when tried using a regular paper scissor. This required a scissor typically used in a machine shop with the sides screwed firmly against each other and the final product had even cut edges, Figure 3.3.



Figure 3.3 Metglas 2605SA1 sheet bending under scissor cutting edges (left) and final cut with straight edges (right)

3.4.2. Study of Cut Edges Under SEM

Small strips of the alloy with different cut edges were studied under the Scanning Electron Microscope to understand the behavior of the material under shear stress conditions.

Shear Under Band Saw

First strip to be studied under SEM was the one that was cut using Band saw. Magnifying on the cut edge of the strip at $40\ \mu\text{m}$ reveals shear deformation along the grains. This is caused by the cutting blade impacting perpendicular to the grains causing the metal to shear off and bend due to the impacting force, Figure 3.4.

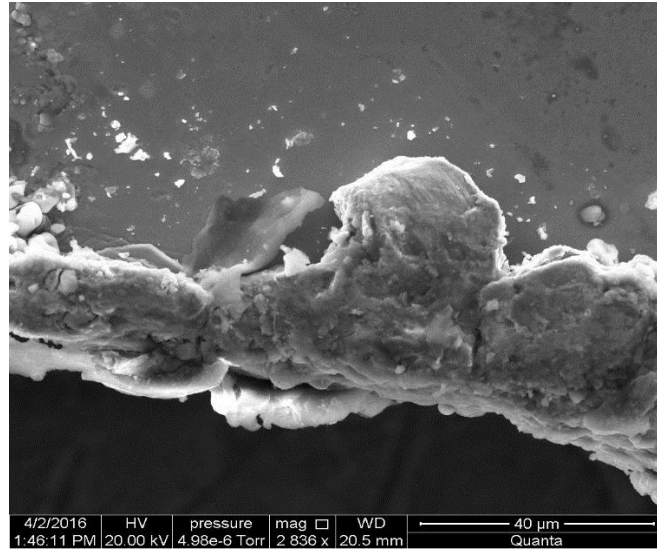


Figure 3.4 SEM image of shear edge under band saw

Shear Under Scissor

At 20 μ m magnification focus along the edge experiencing shear due to scissor, ridge lines are seen. These lines are caused by the rapid expansion and contraction of the metal under shear stress caused by the scissor edges acting as shear punches. This pattern was seen to be along a majority of the strip edge that experienced similar conditions, Figure 3.5.

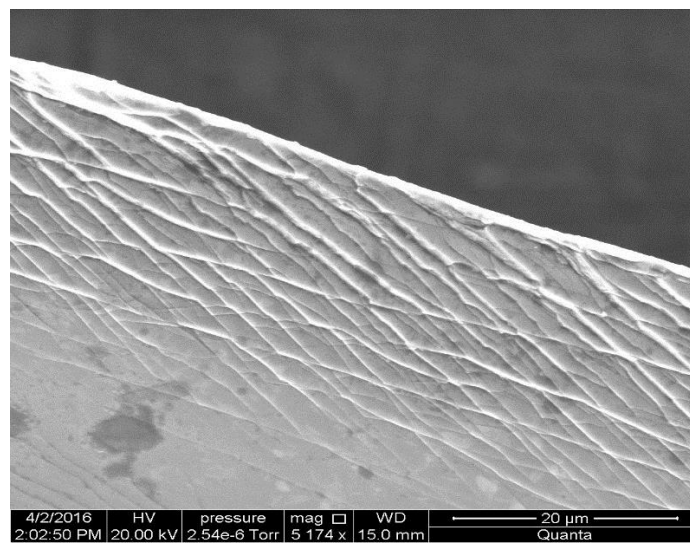


Figure 3.5 SEM image of shear edge under Scissor

3.4.3. Element Composition

Element composition in either sides of the sheet was then analyzed in SEM using Energy Dispersive X-ray Spectrometer (EDX) to find the composition differences if any present. This was carried out to ensure that the element composition was similar on both sides as specified by the manufacturer.

The EDX system provides chemical analysis of the sample material by bombarding electrons on the sample surface at a localized area by means of a focused electron beam. Sampling the reflected electron beam reveals the surface topology and elements present in the localized area of the sample in terms of Atomic Weight percentage (Kanda, 1991).

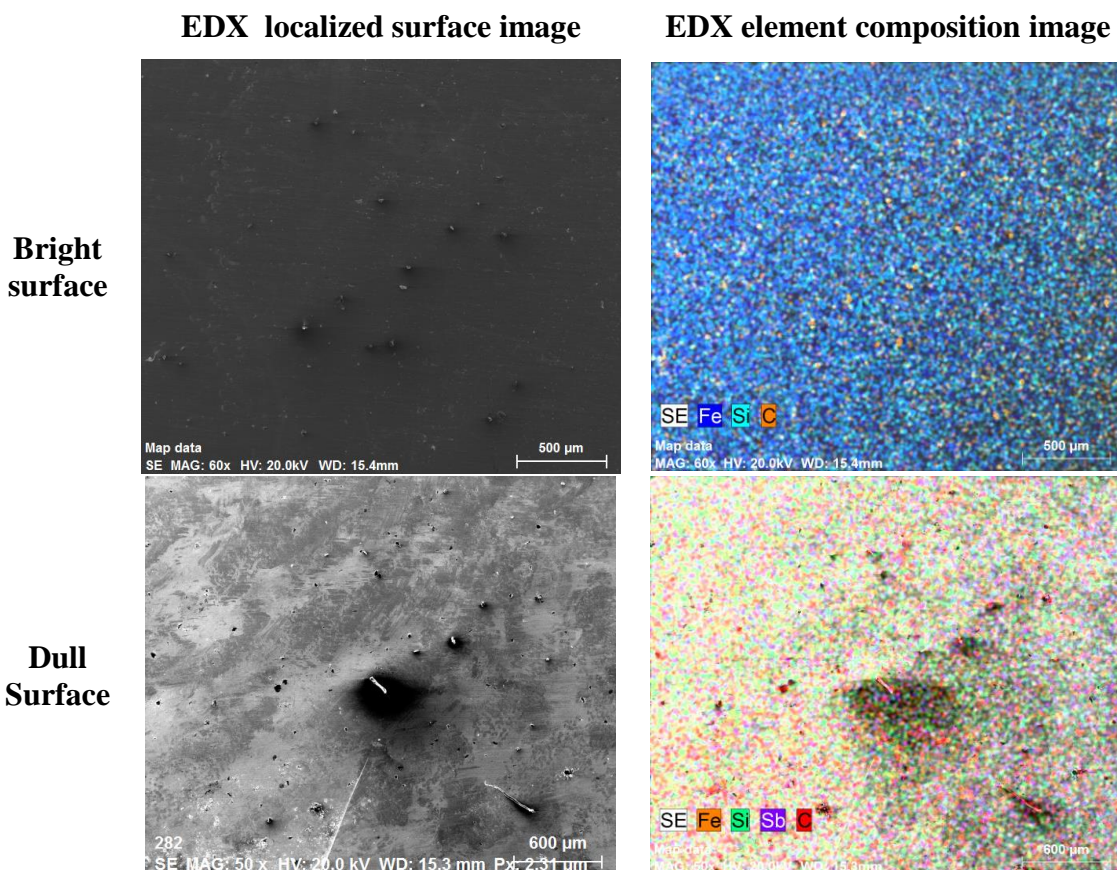


Figure 3.6 Comparison of surface element composition

It can be noted from Figure 3.6 that the major element composition present on either side of the Metglas surface is Iron (Fe) with traces of Carbon (C) and Silicon (SI). The irregularities on the surface seen in the image might have occurred during the sheet manufacturing process, strip cutting process or due to the presence of external impurities. Contrast has been adjusted manually during sampling of the surface in order to reduce the presence of shadows caused by the surface irregularities as the electron beam from the EDX is focused at an angle to the surface instead of perpendicular to it.

Figure 3.7 and Figure 3.8 shows the individual element composition on Bright and Dull surface based on electron distribution in different bands such as K, L, M and N bands respectively.

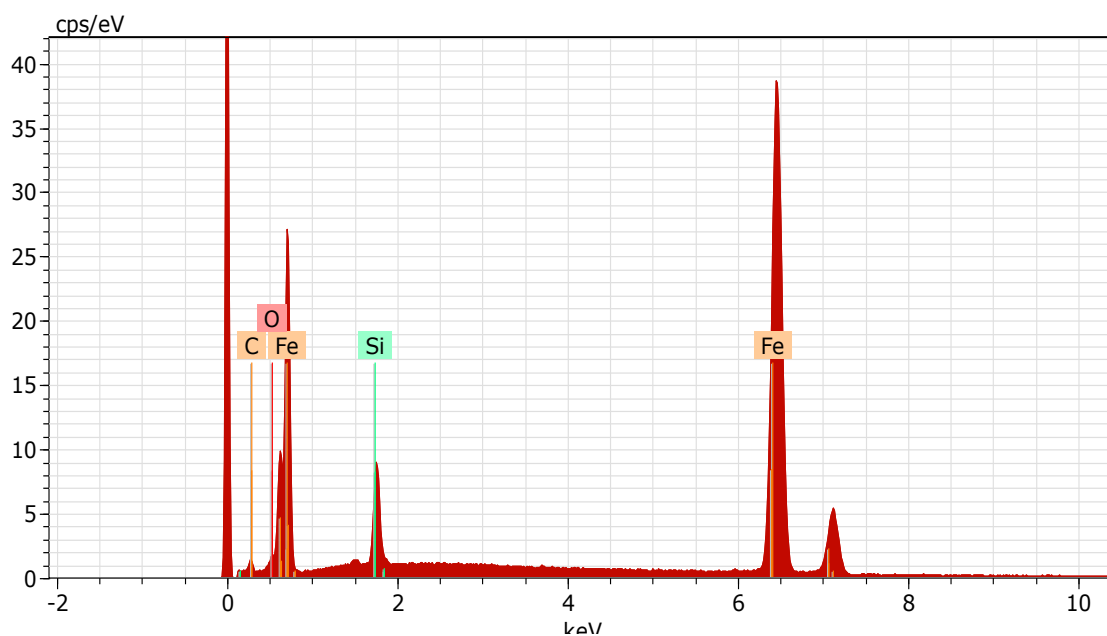


Figure 3.7 EDX plot of individual element composition on the bright surface

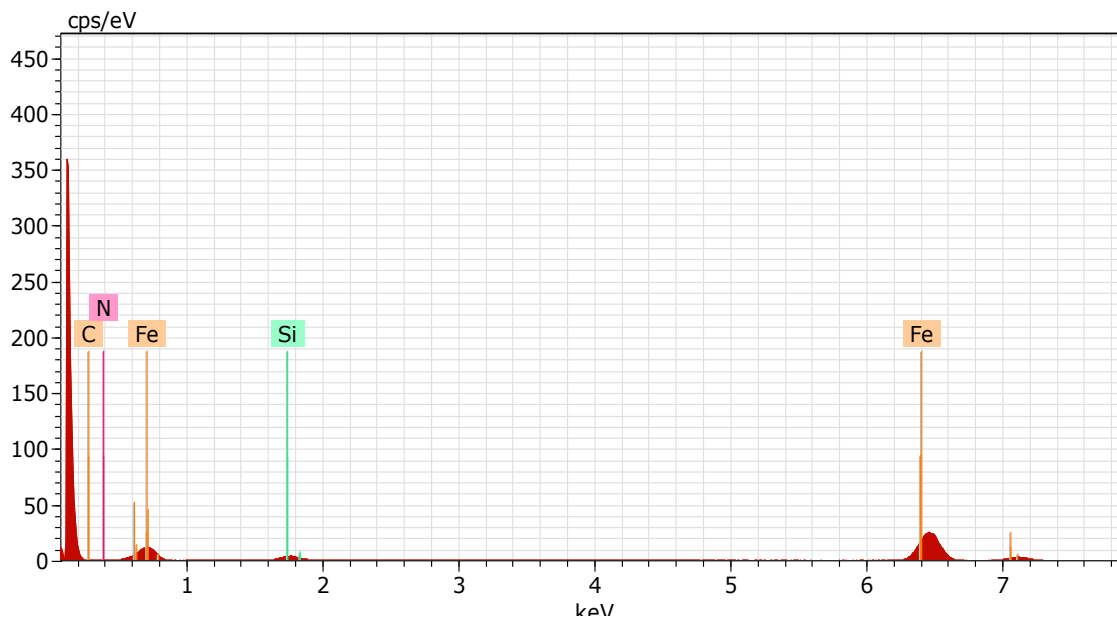


Figure 3.8 EDX plot of individual element composition on the dull surface

Table 3.3 presents the element composition data from EDX present on either sides of the localized surface sample in terms of Atomic Weight percentage. It can be noted that the number of elements present on the sample and percentage of individual element based on its atomic weight is similar to that specified by the manufacturer. Presence of Oxygen (O) and Nitrogen (N) can be attributed to the external impurities present in the sample at the time of surface analysis.

The initial surface analysis was performed to understand the behavior of Metglas 2605SA1 under shear conditions. Due to the differences in texture on either side of the material, element composition study was performed to check for differences. From Table 3.3, it can be noted that the element composition on either sides of the Metgals 2605SA1 alloy is consistent with that of manufacturer specification.

Table 3.3 Comparison of element composition between Manufacturer Specification and EDX data

Elements	Manufacturer Specification (Composition %)	EDX data of Bright Side (Composition %)	EDX data of Dull Side (Composition %)
Fe	85-95	87.48	84.07
B	1-5	-	-
Si	5-10	5.09	4.29
N	-	-	4.21
O	-	1.15	-

4. Experimental Approach

4.1. MAPMD Manufacturing Process

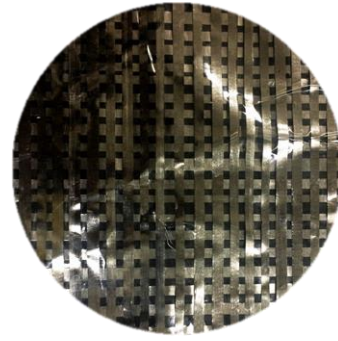
Magneto-Active Propellant Management Device (MAPMD) is a hybrid active membrane consisting of a magneto active material sandwiched between two thin layers of a polymer membrane. In line with the main goal of this study in creating a thin layer on top of the liquid surface, a sheet like membrane model would be sufficient. However, another configuration of the membrane is modeled by shaping it into a mesh like structure where the thickness of the membrane would be doubled along the overlapping regions. The gaps between the weave would assist in weight reduction and hence theoretically the mesh membrane would weigh the same as the sheet membrane.

This magneto active matrix is built out of Metglas 2605SA1 alloy which can be effectively magnetized and demagnetized rapidly due to certain very unique ferromagnetic properties (Sivasubramanian et al., 2015). The sheet is cut into strips of ribbon with each measuring 24 cm in length and 1 cm in width approximately. A mesh matrix is created initially by interweaving the Metglas ribbons to increase rigidity when an external magnetic field is applied.

This matrix is used as an embedded layer within a conventional polymer PMD and is sealed at the edges to make it waterproof. The matrix size and shape are cut to the tank size and are tested for correct fit. Two models, one as a plain sheet and another with the described matrix, are tested for efficiency as shown in Figure 4.1.



(a) MAPMD Sheet



(b) MAPMD Mesh

Figure 4.1 Magneto-Active Propellant Management Device (MAPMD)

These polymers embedded with the matrix inlay would theoretically provide enough block force to absorb the energy transfer in presence of a magnetic field during slosh and provide maximum possible damping of free surface effect and act as hybrid active PMDs.

4.2. Slosh Test Bed Setup at ERAU

The slosh test bed at Embry-Riddle Aeronautical University (ERAU) is an experimental setup consisting of a dynamic force balance with three movable arms attached to a single axis actuator from Aerotech called Linear Motion Actuator (LMA). A pair of FUTEK LCM 300 (Tension and Compression) dynamic load cell is attached at the end of each movable arms. The sensitivity of the load cell is rated at 250 lbs or 1112 N. These load cells measure the forces acting on tank walls and resolve them into forces and moments.

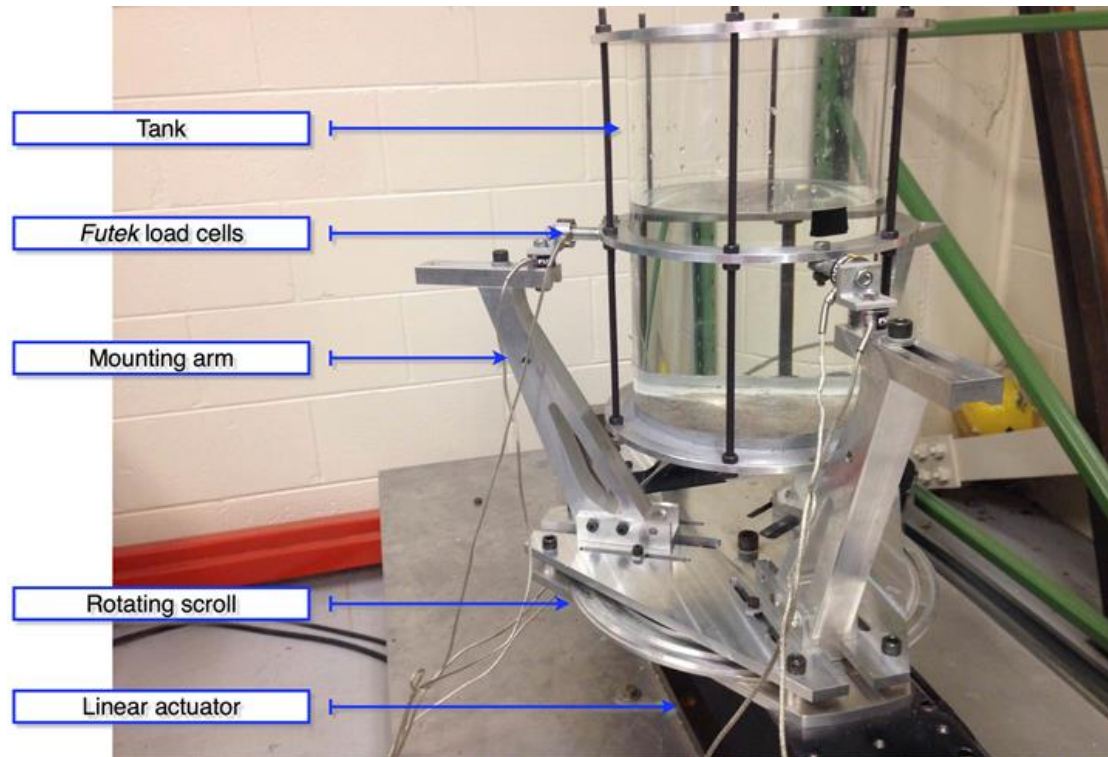


Figure 4.2 Experimental fuel slosh test facility at ERAU

Movement of the arms is made possible by a rotating scroll at the bottom that allows the arms to position and hold tanks of diameters ranging from 8' to 16'. All the tests in this research are conducted in this slosh test bed using a cylindrical tank of 8' diameter and 12' height made of clear acrylic as seen in Figure 4.2.

Motion of the actuator is accomplished by a custom built LabVIEW code coupled with Aerotech's soloist CP software at Embry-Riddle Aeronautical University. External magnetic field is applied by means of a custom built electromagnet which had been previously used in many other experiments.

4.3. Data Acquisition

Data from the load cells are acquired using National Instruments myDAQ as seen in Figure 4.3. As this research aims to provide a proof of concept in slosh damping using MAPMD, only data from two load cells present in the direction of motion of the actuator are collected and analyzed. The DAQ has a resolution of 16 bits a voltage range of ± 10 V supplied across the terminals. This divides the load cell range into (2^{16}) or 65536 parts. From the resolution equation,

$$\frac{V}{2^n + 1} \quad (1)$$

Where V is the input voltage range (volts), n is the bit resolution.

The DAQ provides a resolution of $152 \mu\text{V}$ for every 10 oz. of force. A custom built LabVIEW code is developed which interfaces with the Aerotech Linear Motion Actuator through Aerotech Soloist CP controller. The code allows user to input custom parameters like amplitude, frequency and the number of cycles for controlling the motion of the actuator. The code also interfaces with the load cells through my DAQ for data collection. The collected data is then filtered using a Low Pass Filter provided within the LabVIEW code and is displayed in the form of waveform graphs. The data is split into force and moment readings from the tank wall by the code. This displayed data can be exported as a Microsoft Excel format and later analyzed in MATLAB.

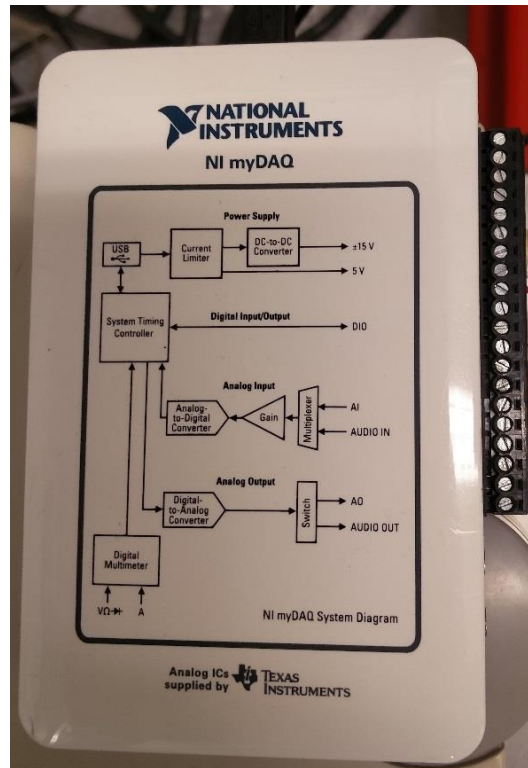


Figure 4.3 National Instruments myDAQ

4.4. Experimental Test Cases and Test Parameters

The experiment is conducted in three phases. The first phase is known as the free slosh characterization in which the baseline sloshing values are taken and analyzed. In the second phase, the slosh test is conducted with inactive MAPMD and the slosh characterization is performed. In this phase, MAPMD placed on top of the liquid surface act as a semi-rigid structural layer and provide passive damping. This experiment is conducted for both sheet as well as meshed membrane.

In the third phase, the magnetic field is applied and MAPMD is controlled to achieve a higher damping ratio and the slosh characterization is once again performed. Again the experiment is conducted for both sheet as well for meshed membrane.

Table 4.1 Test cases

Spherical Tank and Membrane	
Case 1	Free Slosh
Case 2	Slosh with inactive membrane
Case 3	Slosh with active membrane

These three phase experiments are performed for two test conditions, low amplitude and high amplitude slosh. Tanks are excited for 6 seconds in which the slosh reaches its natural frequency for a considered test condition and the simulation continues on until natural damping occurs. The first condition is “low excitation” sloshing. Low sloshing corresponds to the linear motion actuator displacement of 1.8 mm amplitude at which the slosh waves reach a height of 12.5% of the tank diameter. The tank is actuated corresponding to a Simple Harmonic Motion (SHM) whose frequency is 2 Hz and amplitude 1.8 mm. Similarly, the second phase is “high excitation” sloshing. The test conditions are identical except the amplitude of actuation is set at 3 mm at which the slosh waves reach a height of 25% of the tank diameter (Santhanam, 2014).

Table 4.2 Test parameters

	Actuator Displacement (mm)	Frequency (Hz)	Cycles
Low Slosh	1.8	2	12
High Slosh	3.0	2	12

4.5. Force on the Membrane

Simulating the magnetic force acting on the membrane in STAR-CCM+ can be a very tedious task. In order to reduce the complexity of modeling the magnetic field and saving precious computational time, a simple experiment was devised. As the membrane would experience a pull force towards the magnet when it is switched on, the force

experienced by the membrane could be considered as an increase in membrane mass acting on the liquid surface. Adding this mass to that of the membrane would theoretically simulate the pull force on the membrane by the electromagnet in STAR-CCM+.

The experimental setup (Figure 4.4) consists of the hybrid membrane held at four corners of a thin acrylic frame, suspended at 18 cms from base and attached to a FUTEK load cell (LSB 200) with a maximum sensitivity of 50 gms. The load cell is connected to a voltmeter and the output is measured as change in volts. The electromagnet is placed below the center of the membrane setup and is connected to a power supply. This setup replicates the tank setup with the exception of water in between the magnet and the membrane. This however does not affect the resultant force reading as the permeability μ (H/m) of both water and air are relatively similar at 1.256×10^{-6} .

The load cell is first calibrated with precision weights to determine the change in output voltage to difference in loads. The calibration resulted in a change of 310mV reading to a load of 1 gm. The load cell is then attached to a stand at one end and membrane at the other end. Small weights are added to the acrylic frame to balance the membrane horizontally.

The experiment yielded a voltage difference of 0.12 V when the magnet is switched on corresponding to increase in mass of 387.1 mg experienced by the load cell. This mass is then substituted in simulation for “Active MAPMD” condition. As 1 N equals 0.10197 kgs, theoretically the force experienced by the membrane is 0.0037 N.

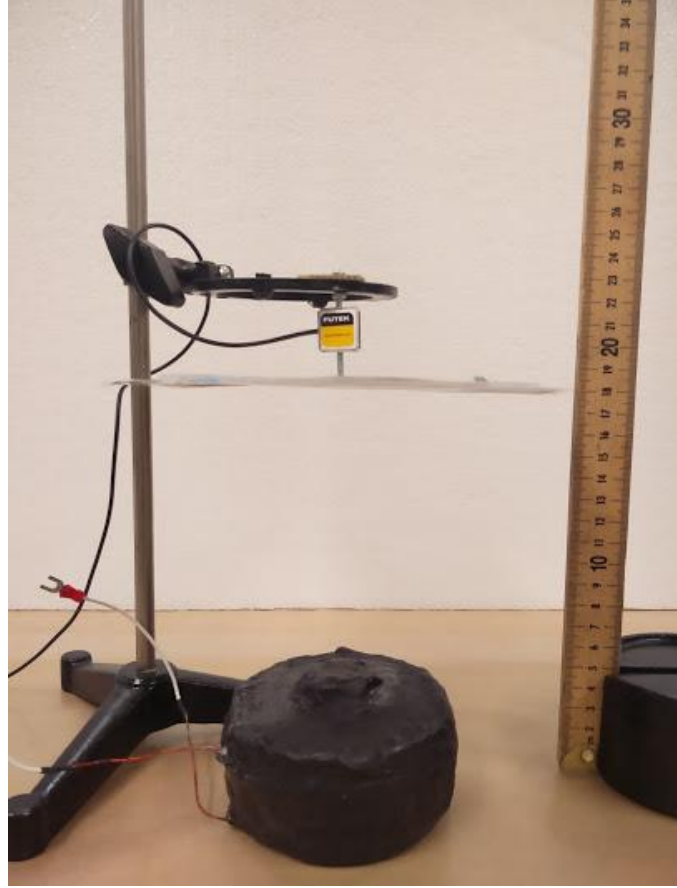


Figure 4.4 Experimental setup to measure force on the membrane

To check the validity of the force calculation by the experiment, known variables such as the current, number of turns in the electromagnet used, distance of the membrane from the electromagnet are provided as input to the force equation:

$$F = \frac{\mu_0 N^2 I^2 A}{2l^2} \quad (2)$$

Where μ_0 is the permeability of vacuum (H/m), N is the number of turns in electromagnet, I is the current supplied to the magnet (Amperes), A is the area on top of the bolt (m^2) and l is the distance of the membrane from the top surface of the bolt (m).

$$F = \frac{(4\pi * 10^{-7}) \times (230)^2 \times (2.3)^2 \times (\pi * 0.013^2)}{2 \times 0.115^2} = 0.0071N$$

From the experiment calculation and above equation, the force calculation is valid as both the results are of similar magnitude.

4.6. Experiment Setup

The experiment setup for studying the slosh damping characteristics of the proposed hybrid membrane consists of the slosh test bed at ERAU in which the tank is partially filled at 60% water level with an electromagnet placed at center of the tank bottom. The electromagnet used in this research has been used in prior research projects like Electro-Active Micro Baffles at ERAU (Santhanam, 2014). It is coated with a layer of sealant making it water proof. It is connected to an external power supply of 12V via a small no. 2 threaded rod that has been inserted through the acrylic tank by a hole drilled an inch apart and two inches from the tank base (Figure 4.5).

Output of the load cells attached to the tank are connected to the National Instruments myDAQ data acquisition unit coupled with a low pass filter. This filter component is essentially a capacitor connected in conjunction with the resistor to form a passive RC low pass filter across the positive and negative DAQ terminals. This filters out the noise signals and allow only data signals to be read by the DAQ. The data signals provide the force and moment acting on the tank walls. Analyzing and calculating the damping coefficient of the slosh data collected after the actuation period of 6 seconds provides the slosh suppression characteristics of the hybrid membrane.

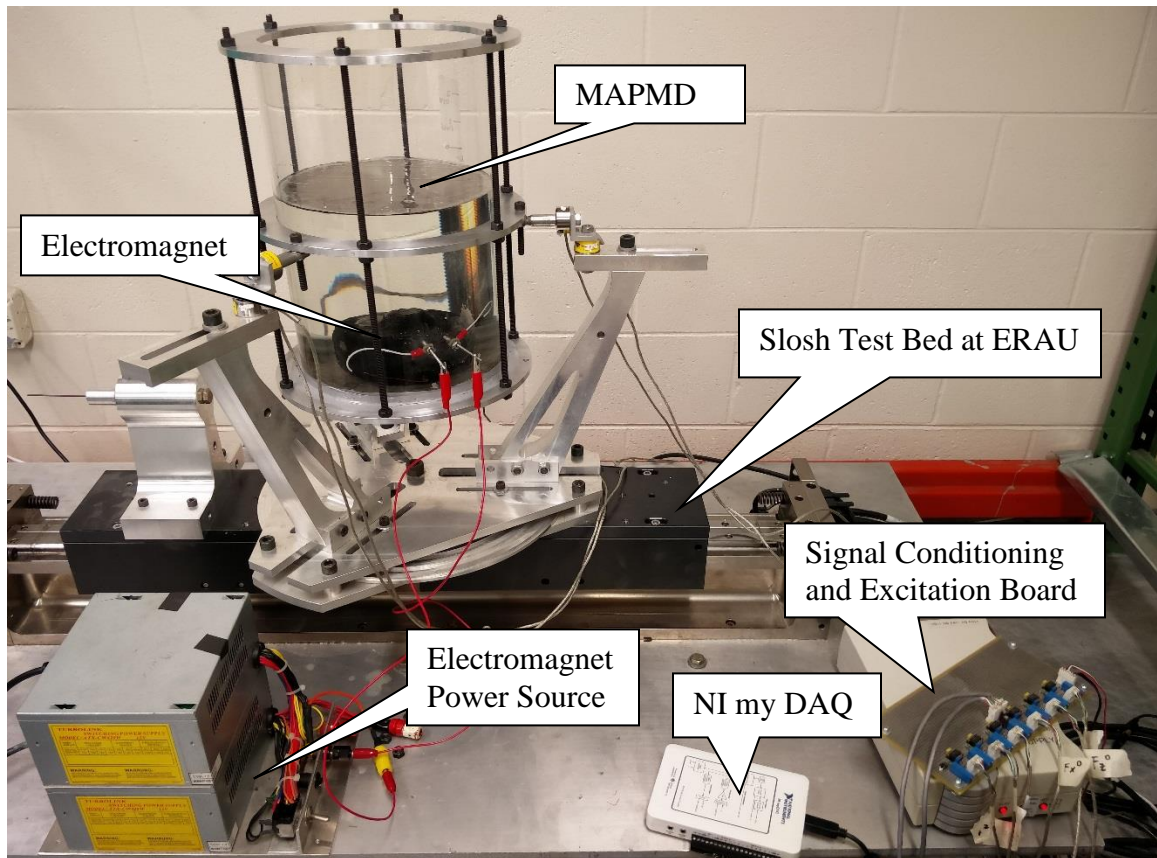


Figure 4.5 Experiment setup to study damping characteristics of MAPMD

4.7. Load Cell Calibration

Calibration is required to understand and analyze the output signals from the load cells. The FUTEK load cells used in this experiment are rated at 250 lbs and for calibration purposes, a minimum load of 25 lb was used. Output from the load cell under no load condition was noted at 0.0724 mV. It is then loaded with 25lb and the reading was noted at 2.09 V. From the calibration tests, it was found that the load cell provides an output of 80 mV/lb.

Change in voltage reading due to the impact of slosh waves on the tank wall is desired to be displayed in terms of Newton in LabVIEW for force calculations. Hence a coefficient must be found in relation to the voltage output so that the readings are

converted to Newton. 1 N corresponds to 0.15 lb force. From calibration tests it was found that a voltage reading of 2.7 mV corresponds to 1 N load. Hence $1/0.0027$ provides a coefficient of 370.4 which was provided in LabVIEW code as a constant multiplied to the data from DAQ. The voltage output displayed in LabVIEW from the load cell is now in terms of Newton.

5. Computational Approach

5.1. Computational Phases

Computational approach to validate and verify the experimental results in this research is split into two phases. The first phase involves performing computational finite element analysis on MAPMD to find out its stiffness constant under static vibration condition for different slosh modes. This phase is carried out for both MAPMD sheet and meshed membrane. Effect of magnetic field on MAPMD is not considered in this case.

The second phase involves computational fluid dynamics where the behavior of MAPMD in conditions similar to those of the experiment is studied in a controlled computational environment. For proof-of-concept purposes, only meshed MAPMD membrane, Figure 4.1 (b), is considered and its results are then compared and verified with that of the experiment.

5.2. Modal Analysis

In this research, MAPMD is constructed as a sheet and as a meshed model to experimentally compare its damping effectiveness. Modal analysis help in determining the mode shapes of a structure under vibration, in this case the MAPMD sheet and meshed membrane. Membranes used in previous researches were fixed along its edges to a partially filled tank wall at a certain tank height. On application of external stimuli, the membrane adheres to the slosh contours and a few well defined slosh modes were studied such as crater, mountain, yin-yang and ridge shapes (Green, et al., 2010) as shown in Figure 5.1.

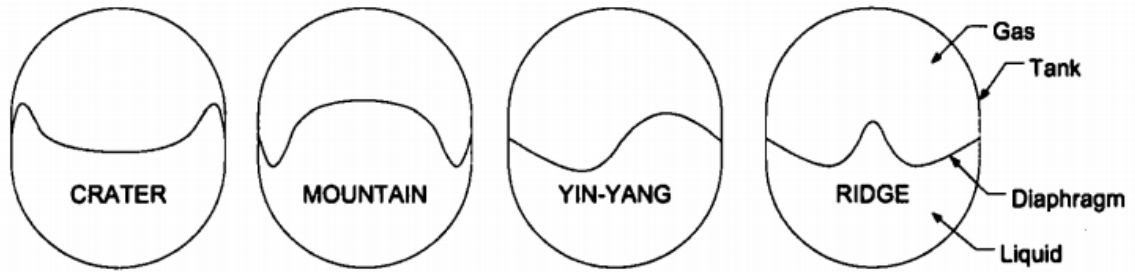


Figure 5.1 Slosh mode shapes for a fixed diaphragm (Green, et al., 2010)

In the first phase of computational approach, MAPMD is modeled as both meshed and solid membrane using CATIA with a diameter of 8' corresponding to that of the tank diameter. In order to avoid complications in simulation, the edges of the geometries were rounded off as shown in Figure 5.2.

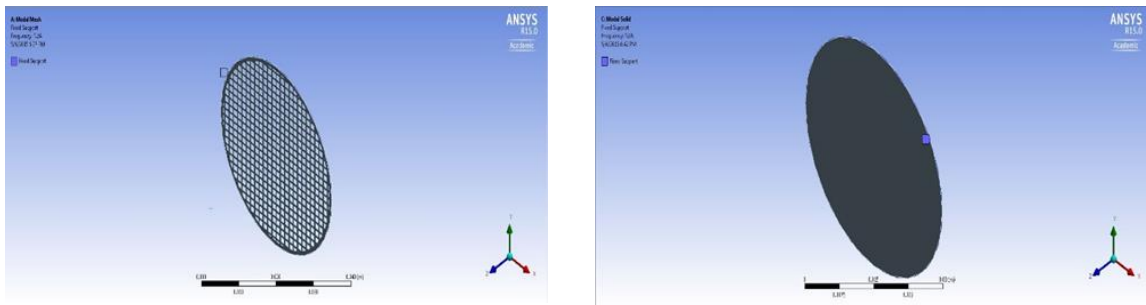


Figure 5.2 Modal Analysis of Mesh and Solid Membrane

Modal Analysis, a static structural analysis, is present under Analysis Systems tab in the Toolbox window of ANSYS Workbench. Simulation is carried out separate for meshed and solid membrane geometry. CAD model from CATIA is imported into the workbench and is constrained along the sides. Material properties such as tensile strength, elastic modulus and density of Metglas 2605SA1 were obtained from the manufacturer. Membrane mass, moment of inertia and the center of gravity is obtained from CATIA. The pressure values were taken as appropriate to the research conditions and were given

as input for different modes of vibration. For proof-of-concept purposes, only 6 different modes of vibration was considered.

On analysis, frequencies for different modes of vibration are obtained from ANSYS and are then plugged into the corresponding frequency equation shown below to calculate the stiffness constant.

$$f = \frac{1}{2\pi} \sqrt{\frac{k}{m}} \quad (3)$$

Where f is the frequency in Hz, k is the stiffness constant in N/m and m is the mass of the membrane in gms.

5.3. Computational Fluid Dynamics

5.3.1. About Computational Fluid Dynamics

The Computational approach resorts to numerical calculus using “Computational Fluid Dynamics” (CFD) software. CFD is an ensemble of numerical methods that allows for finding an approximate solution of a fluid dynamics problem. It involves fluids mechanics equations which are solved computationally. The solution obtained is not an accurate one but is an approximate one since the Navier-Stokes equations are solved computationally by discretization. Some equation terms are too complex to be solved and are replaced by empirical but inaccurate models. It happens especially in turbulent flow regimes (Paul, 2014).

However, with the advancement of computers since 1950s, powerful graphics and 3D interactive capability, the use of CFD has gone beyond research and into industry as a design tool. Current workstations offer enough computational power to provide very satisfying solutions.

Even if the conditions are ideal comparing to the experiment, the simulation is complementary with the experimental study. Experiments provide macro data at certain points in the flow field, while a numerical simulation provides a detailed resolution such as turbulence, viscous forces and velocity. These are some of the reasons why CFD is a powerful and necessary tool to resolve complex dynamic and flow problems such as propellant slosh. Finding the solution of a fluid dynamics problem comes down to solving a differential equation. In the case of a Newtonian fluid, the solution of Navier-Stokes equations is employed. The Navier-Stokes equations are a set of partial differential equations describing the processes of heat and mass transfer. The velocity of the fluid is widely lower than the speed of sound and air is assumed to have constant density. This is the incompressibility hypothesis. Assuming air is incompressible, the Navier-Stokes equations are (where \vec{v} is the velocity of the fluid particle):

$$\frac{\partial \vec{v}}{\partial t} + \overrightarrow{\text{grad}} \vec{v} \cdot \vec{v} = -\frac{1}{\rho} \overrightarrow{\text{grad}} p + \nu \Delta \vec{v} + \vec{g} \quad (4)$$

These equations have no known general analytical solution (i.e. no Direct Numerical Simulation or DNS), but it can be approached. Thus, it is necessary to resort to the Reynolds- averaged Navier-Stokes equations (RANS), which are a very accurate and precise approach alternative to direct calculus.

$$\rho \left(\frac{\partial \bar{v}_i}{\partial t} + \frac{\partial}{\partial x_i} (\bar{v}_i \cdot \bar{v}_j) \right) = \frac{\partial \bar{p}}{\partial x_i} + \frac{\partial}{\partial x_i} (\bar{\tau}_{ij} - (\bar{v}'_i \cdot \bar{v}'_j)) + \rho \bar{g} \quad (5)$$

With $v = \bar{v} + v'$ written in the temporal mean plus fluctuation decomposition.

Owing to the $(\bar{v}'_i \cdot \bar{v}'_j)$ term, a problem in closure appears. This additional term embodies the Reynolds, confines and requires the using of a turbulence model. In this case, the K-Epsilon model is particularly adapted. To solve this problem computationally,

the method of finite volumes is employed. It relies on a geometrical meshing of the domain (surface and volume) in which the fluid flows. Very pertinent in fluid dynamics as it deals with the classical quantities conservation (momentum, energy, mass), this method reckons what goes in and what goes out of a mesh (i.e. of a finite volume). The residuals from the simulation calculating the boundary condition along the mesh grids report the difference between the ingoing and outgoing volume in meshes and assesses the accuracy of the simulation. When the residuals grow above a certain value, the calculation is considered as not convergent and the boundary conditions need to be altered for converging the solution.

5.3.2. Assumptions in Computational Fluid Dynamics

The CFD domain is an idealistic region where many real life factors are not taken into consideration. Thus, several assumptions need to be taken into account to compare both experimental and computational approaches.

- Ideal environmental conditions
- Iso-surface assumptions on the liquid free surface
- Thickness of the tank wall is neglected
- MAPMD membrane is considered as rigid wall for initial analysis
- Owing to the difficulty in modeling the magnetic field and its

effect on the membrane, mass of the membrane is altered for “Active MAPMD” simulation condition.

5.3.3. Modeling of Membrane and Tank

For proof-of-concept purposes, only meshed MAPMD is considered for CFD simulations. The membrane is modeled in CATIA under generative sheet metal design workbench with thickness of 1mm and default bend radius of 2mm. Initially a single wavy like strip with crest and trough is designed along one direction with respect to a reference axis taking into consideration of how a single Metglas ribbon would look like in the interwoven membrane. Parallel to this strip, another one is designed at a distance of 3mm from the axis with the crest and trough positioned opposite to the original strip design. To form a matrix like structure, similar strip designs are carried out perpendicular to the first and second strips at the axis. These individual strips are then patterned to appropriate distances from both sides and directions from the central axis. This would appear as a rectangular mesh pattern. To achieve a circular shape resembling the meshed membrane, operation of pocket from part modeling workbench is carried out Figure 5.3.

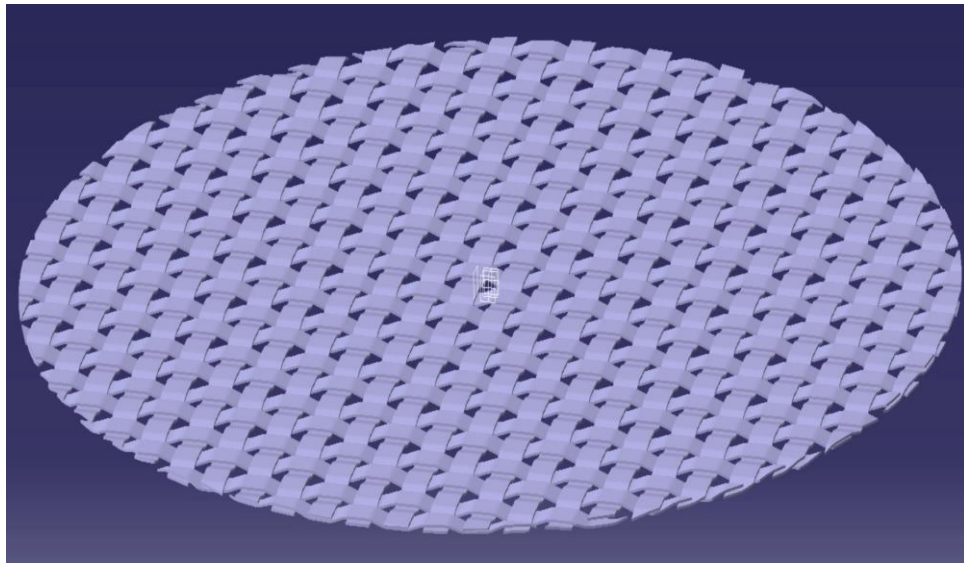


Figure 5.3 Meshed membrane modeled in CATIA

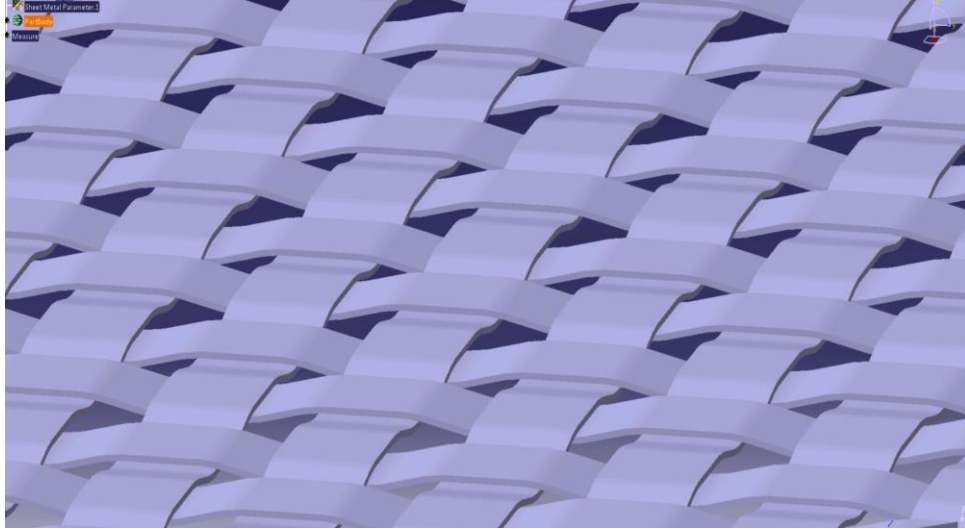


Figure 5.4 Close-up view of individual membrane strands

Modeling of tank is again carried out in CATIA under part modeling workbench. A circular cylindrical tank of 8 inch diameter is drawn and extruded for 12 inches. In appearance, this would resemble a solid cylinder enclosed on both sides. Both the membrane and tank are imported into Star-CCM+ using the feature called import surface mesh.

To avoid misaligning or overlapping of the cylinder and membrane surfaces, a simple technique based on axis referencing is followed. The membrane is designed as a symmetrical model keeping the axis of reference at its center. During the experimental phase, the membrane is placed at the top of liquid surface which is at 60% fill level. In order to replicate this scenario computationally, the tank design is made with the axis of reference placed at the 60% cylinder height which was calculated manually as shown in Figure 5.5. On importing these two geometries simultaneously in Star-CCM+, the membrane would align perfectly at 60% cylinder height just as seen from the laboratory set up.

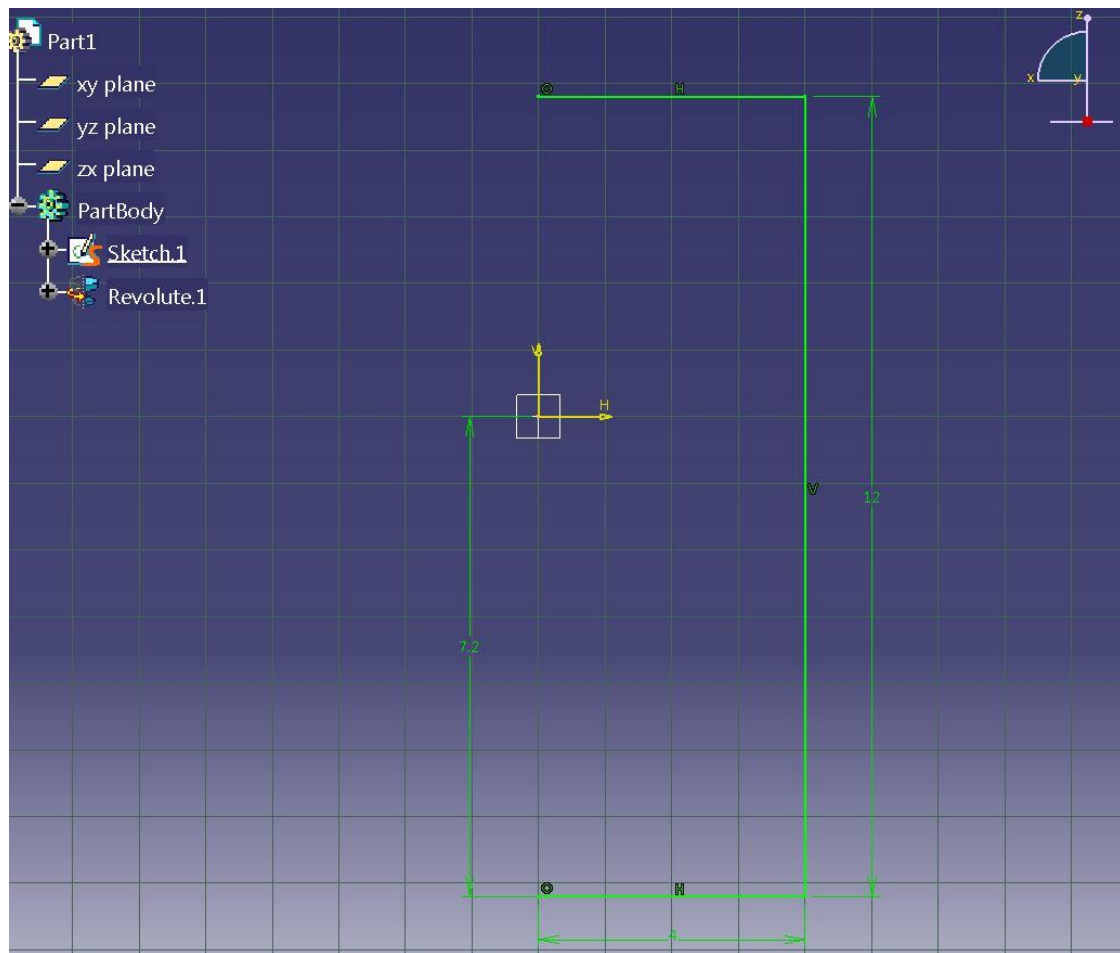


Figure 5.5 CAD geometry of cylinder tank

5.4. Importing Geometry into STAR-CCM+

When importing a geometry into STAR-CCM+, the entire geometry surface is mapped and surface mesh is applied by default. STAR-CCM+ converts the physical geometry into regions where boundary conditions are applied and simulation is initialized. The entire imported geometry is considered as a single region and the surface mesh pattern follows the geometry surface. Mesh quality decreases at sharp, irregular, joint, bent or open surfaces producing sharp skew angles leading to surface mesh error. STAR-CCM+ allows the user to manually edit surface irregularities and adjust the mesh around those complex surfaces using Repair CAD option or Launch Surface Repair

option in the main toolbar. Also, open surfaces can be patched, sharp surfaces be smoothed out, unwanted geometrical shapes inside the CAD model be removed.

The cylinder tank is imported by default as a surface mesh in STAR-CCM+. The geometry surface is checked for design errors using the Launch Surface Repair tool. Prior to meshing, the geometry is split into different parts and labelled appropriately as Tank Top, Tank Wall and Tank Bottom using Split by Patch option. The parts are then assigned to Regions where mesh and physics conditions are applied separately for each part.

As the simulation involves interaction between water and air phases at 60% tank height, fine mesh is required throughout the simulation region for obtaining best results. Varying mesh parameters at a specific portion in a geometry is made possible with the use of volumetric control which is described in later section.

5.5. Meshing Procedure

Mesh is typically described as the discretized representation of the portion involved in computational domain that the physics solvers utilize in providing numerical solutions. Study of mesh is a critical component of any simulation. A good quality mesh is necessary to produce accurate results and provide solution convergence. However, very fine mesh would drastically increase computational time and the opposite is true for a coarse mesh. Computational time also depends on the number of iterations per time-step and hence a relation must be established between them for obtaining the desired result.

One of the main parameter considered in this simulation is the physical time. This parameter helps relate the simulation setup to that of the experiment setup. Mesh size, number of iterations and time-step have to be chosen to obtain a convergent solution for

the considered physical time while maintaining a low computational time. STAR-CCM+ offers two types of meshing, which is Parts-based and Regions-based meshing with each having its own advantages and disadvantages. In this simulation, Regions-based meshing procedure is considered.

5.5.1. Mesh Resolution

From the explanation provided by (Ravelet, 2013 and Schlichting, 2000), it is essential to ensure a good and sufficient resolution in strong gradient regions in order to report the local phenomena as accurately as possible. The delicate geometries present in this simulations are walls, boundary layers, etc. Thus, a finer meshing will be necessary in these particular regions. Also recommended is to generate over a minimum of five to ten cells between two walls. During the Star-CCM+ simulation, to avoid the boundary layer phenomena, a custom Boundary Growth Rate is set within the Boundary nodes of the cylinder tank. Mesh growth rate is taken as Medium.

5.5.2. Choice of Mesh

Star-CCM+ offers several meshing strategies depending on the application. Various volume meshing techniques such as Tetrahedral, Polyhedral, Advancing Layer and Extruder are available. For this research, the meshing models used in all the simulations are Surface Remesher, Trim Cell Mesher and Prism Layer.

The Trimmed Mesher generates a volume mesh by cutting a hexahedral template mesh with the geometry surface. The Prism Layer Mesher adds prismatic cell layers next to wall boundaries. It projects the core mesh back to the wall boundaries to create prismatic cells. This feature is very useful to finely divide the domain close to the walls,

where boundary layer phenomena happen. As per Kynan Maley's conference (Kynan Maley, 2012), the volume meshing is the basic tool that allows the creation of the spatial discretization required to solve CFD problems.



Figure 5.6 Meshed cylinder

The first step is surface preparation, the Wrapper and Remesher constitutes this surface meshing. However, the surface wrapper is used for poor quality and complex CAD geometries (Mikell et al., 1984). As the tank used in the simulation (cylinder) is topologically simple, this tool can be avoided. It is recommended to use the Surface Remesher prior to volume meshing. The second step is the Volume Mesh generation constituted by either a Polyhedral Mesher or a Trim Cell Mesher, and by a Prism layer.

(Kynan Maley, 2012) advises the Polyhedral mesher for general purpose as being reliable and robust, particularly suitable for conjugate heat transfer simulations. The Trimmer is high quality, fast and perfect for large domains. The Polyhedral is also preferred, thanks to its rapidity and the reasons described previously. Figure 5.7 shows the mesh models for background mesh and volumetric control block mesh chosen for this research. Table 5.1 summarizes the chronology of several paths of Volume Meshing on Star-CCM+. The meshing techniques used for this research is presented in bold. Surface mesh dimensions and parameters considered.

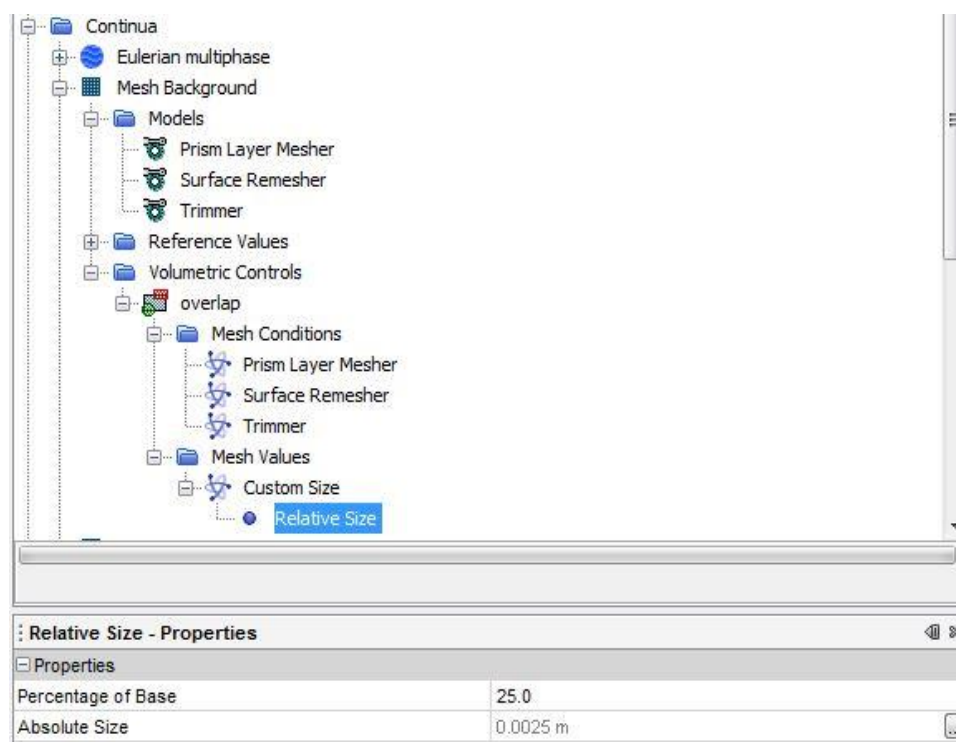


Figure 5.7 Volume mesh models

Table 5.1 Chronology of adopted paths in this research

SURFACE PREPARATION		VOLUME MESH GENERATION	
Wrapper	Remesher	Trim Cell Mesher	Prism Layer
		Polyhedral Mesher	

Mesh Study (Free Slosh)

Mesh study was conducted for 3 cases with varied parameters as seen from table. Several parameters were modified between cases and a few were considered at their default value. Case 1 contained coarse mesh settings with a time step of 0.01 and maximum inner iterations of 5 which is the default value. This was taken as the base condition for mesh refinement in later cases. This case yielded a short simulation time with low continuity convergence in the order of $1e-2$ and irregular amplitude peaks. Also, the short time-step caused loss of fluid inside the container at the end of simulation.

Base size was decreased in case 2 and the mesh quality was further refined. Time-step was increased to 0.001, which is the default value and maximum inner iterations was taken as 6. This condition provided good continuity convergence in the order of $1e-3$ with the obtained amplitude peaks favorable to the experiment

A well refined condition of case 3 with a time-step of 0.0001 led to increase in computational time with no comparable change in final results. Slosh amplitude peaks and continuity condition remained consistent.

Table 5.2 Test cases for mesh study

Parameters	Case1	Case2	Case3
Base Size	1	0.1	0.01
Surface Repair Minimum Quality	0.1	0.01	0.001
Maximum Cell Size	1000	10000	100000
Number of Prism Layers	1	2	5
Minimum Surface Size	10	25	50

Surface Relative Target Size	50	100	150
Volumetric Control Surface Remesher Size	1.0	2.0	5.0
Template Growth Rate	Medium	Medium	Medium
Wrapped Surface Faces	9470	9470	9470
Remeshed Surface Faces	2050	34526	463636
Calculation time for Surface Mesh	5s	15s	2min 30s
Volume Mesh Cells	4277	95356	1791575
Calculation Time for Volume Mesh	8s	1min 10s	3min 25s
Time Step	0.01	0.001	0.0001
Maximum Inner Iterations	5	6	10
Maximum Steps	10000	100000	1000000
Simulation Time (Cluster)	<24hrs	52hrs	>60hrs

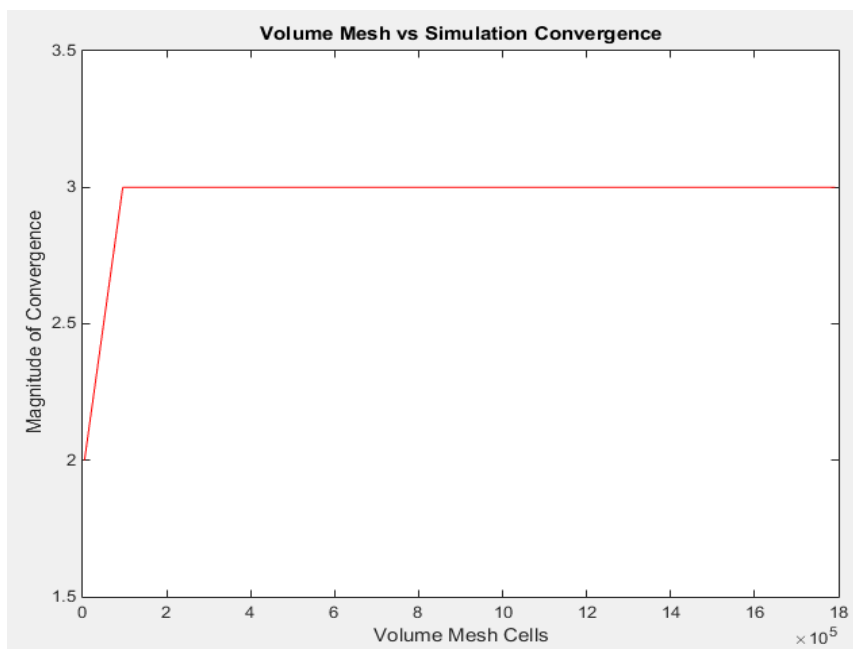


Figure 5.8 Magnitude of convergence for number of volume mesh cells

Based on the study, a mesh containing 95356 nodes and a time-step of 0.001 was found acceptable to this simulation as shown in Figure 5.8. Further refinement led to similar results with increase in computational time.

5.5.3. Volumetric Control

Volumetric controls are an appropriate tool for precise control of mesh size. It allows the user to precisely refine the meshing for both Surface, Volume and Prism Layer Meshes (Kynan, 2012). Figure 5.9 illustrates the volumetric controls of the cylindrical tank. For the tank in study, the volumetric controls are located about 1.8 inches above and below the free surface of the still water. When sloshing, the peaks of water barely reaches higher levels; yet a compromise has to be found between the precision of remeshing and time of computation. Furthermore, the refinement Growth Rate set at Medium enables a smooth transition in meshing between the volumetric controls and the base size of the cylinder mesh. Thus, even beyond 1.8 inches above and below the initial free surface, the mesh slowly increases in size.

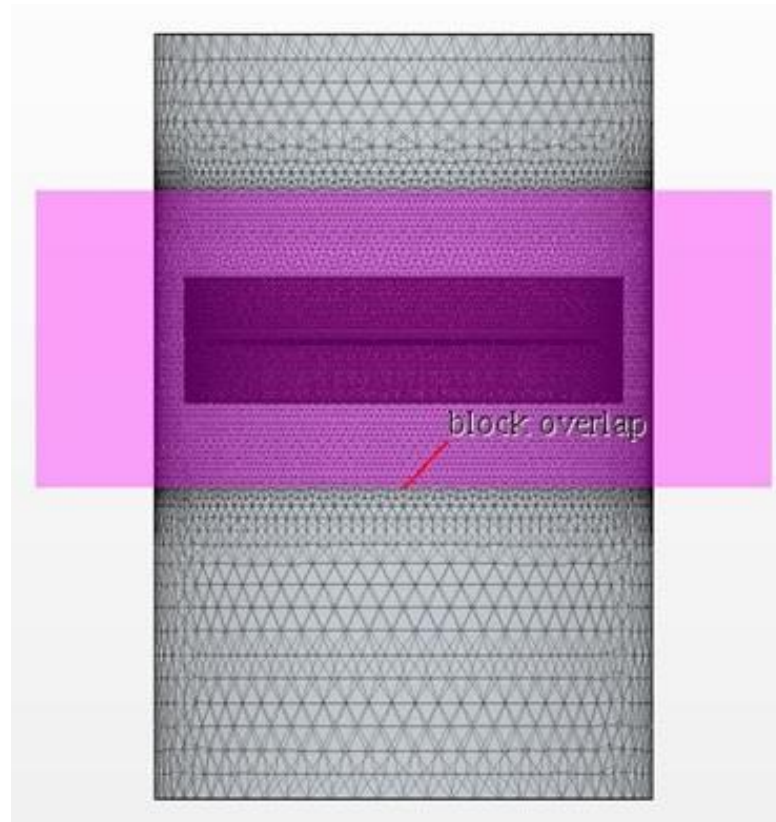


Figure 5.9 Volumetric block

5.5.4. Overset Mesh

Overset Mesh is a powerful tool implemented in Star-CCM+ and is used to discretize the computational domain into various meshes that overlap at different scales. This technique turns out to be very useful in problems with numerous or moving bodies. It is therefore adept for the simulations involving passive membrane. A background region should be created in any study involving an Overset mesh. This region encloses the entire solution domain. Smaller regions can be created within the background region so as to enable a correct overlapping of the meshes. Called ‘Overlap’ in the illustrations, these regions act as links in establishing the junction between background and following region. Eventually, the Overset regions are generated around the bodies and is encapsulated into bigger regions. Only the Overset region moves in accordance to the

body motion and the mesh overlapping is executed and updated at each step of the calculation.

5.5.5. Regions and Boundary Conditions

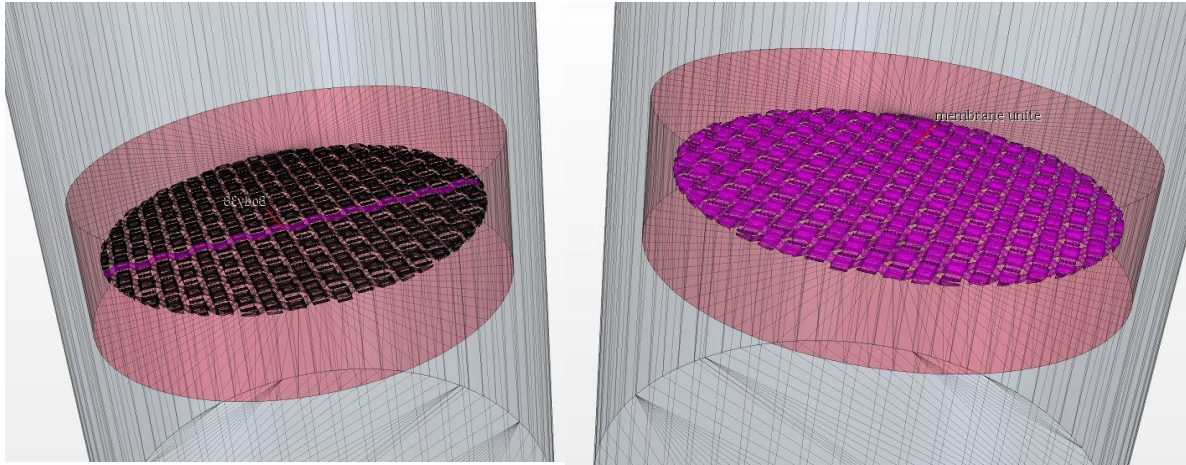
Two different approaches are chosen to simulate the different cases. In the first case, the free slosh does not involve a specific meshing except the volumetric control surrounding the water surface as described earlier. For the second case involving passive membrane, simulation requires resorting to the Star-CCM+ tool Overset Mesh and subtract.

Subtract

In order to simulate stationary MAPMD during sloshing, a Boolean operation is carried out with the initial parts. The command Subtract Parts subtracts a defined shape from the volume of a target part. The surface of the resulting part is formed from segments of the constituent part surfaces. In this simulation, the target part will be the volume of the tank while the extracted shape will be the membrane. A new part is thus created out of the initial tank and holds the imprint of the MAPMD.

Unite

This is another operation used in Star-CCM+ to unite different parts to a single region. In this research it is used to unite the individual strands of the membrane. The MAPMD contains number of individual strands as mentioned earlier in CATIA section. Strands are united together to make them work like one whole membrane Figure 5.10.



(a) Individual Strands

(b) Strands united as a single Membrane

Figure 5.10 Individual strands united to become one whole membrane

Overset Mesh

To enable the motion of rigid bodies such as the MAPMD in this research, overset meshing technique is to be used in the simulation, the principle of which has been previously described. The regions have to be set accordingly.

In this research, woven membrane is taken inside the domain Figure 5.11. The overset mesh region has three types of cells active, acceptor and inactive. Within active cells governing equations are solved. Acceptor cells separate active and inactive cells. Inactive cells becomes active when the overset region moves within the background region. Overset region moves according to the body motion and the overlapping mesh is updated for each step in the simulation.

Drawback of Overset Mesh

The main drawback of this meshing technique is that it requires 4 to 5 cells gap between the overset and background region. This is the primary reason for the membrane being cut in a fashion that it does not touch the cylinder wall. This is region where active,

inactive and acceptor cells couple with each other for the communication and exchange of the data. As described previously, only the overlapping layer of the overset mesh undergoes changes at each step of simulation.

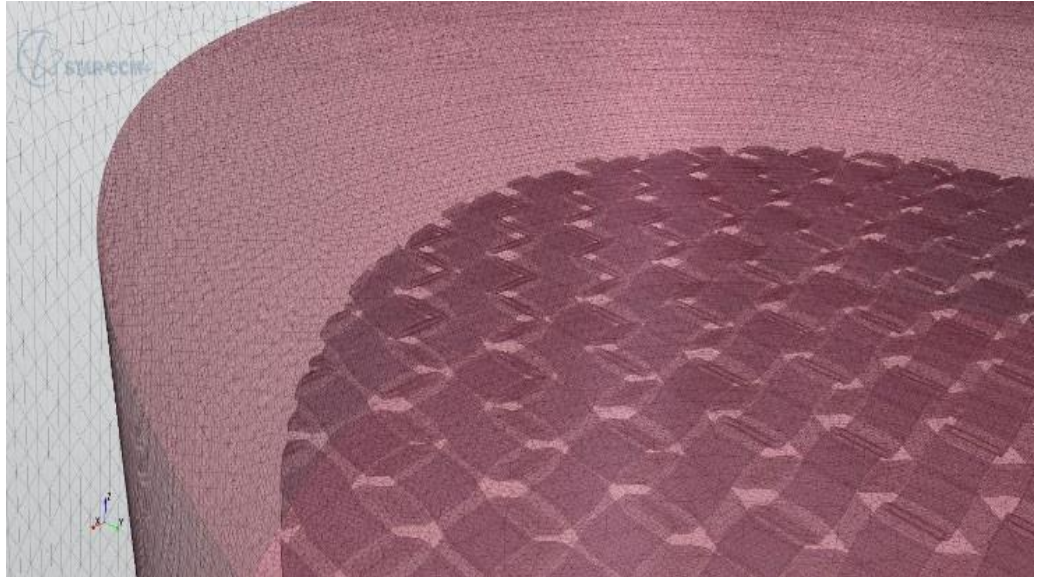


Figure 5.11 Overset Mesh block between tank wall and membrane

5.6. Special Features in Meshing

Meshing requires created regions first. Furthermore, assigning the parent part must be performed before assigning individual part surfaces to a boundary. Now that the regions are created out of some parts, Mesh continua should be created and then applied to these regions.

5.6.1. Subtract

In the case of subtract (stationary membrane), only a single region needs to be created out of the subtract part. Mathematically, this region is the volume of the tank “minus” the imprint of the MAPMD. Thus, a unique mesh is generated for the whole domain. This mesh has proper volumetric controls to be sufficiently fine in the ‘risky’

regions. Figure 5.12 reveals the volumetric controls around the membrane in the (x y) plane. Several simulations have been conducted before running the most accurate one to determine the highest level of water. Given that information, the volumetric control surrounding the water surface can be precisely placed. In this way, the domain is not refined futilely: only the interesting and problematic areas are sharpened, furthermore at the right height. It is essential to ensure an accurate computation. In the case of the stationary membrane and for high amplitude actuation, it appeared that water level did not rise more than 1.1 inch above (or -1.1 inch below) the initial and still water level. The volumetric control chosen was therefore a cylinder whose top is 1.2 inch above initial water free surface and bottom is 1.2 inch below. For the simulation involving the membrane, a view of the mesh surrounding the woven strips and the water surface is presented on Figure 5.13.

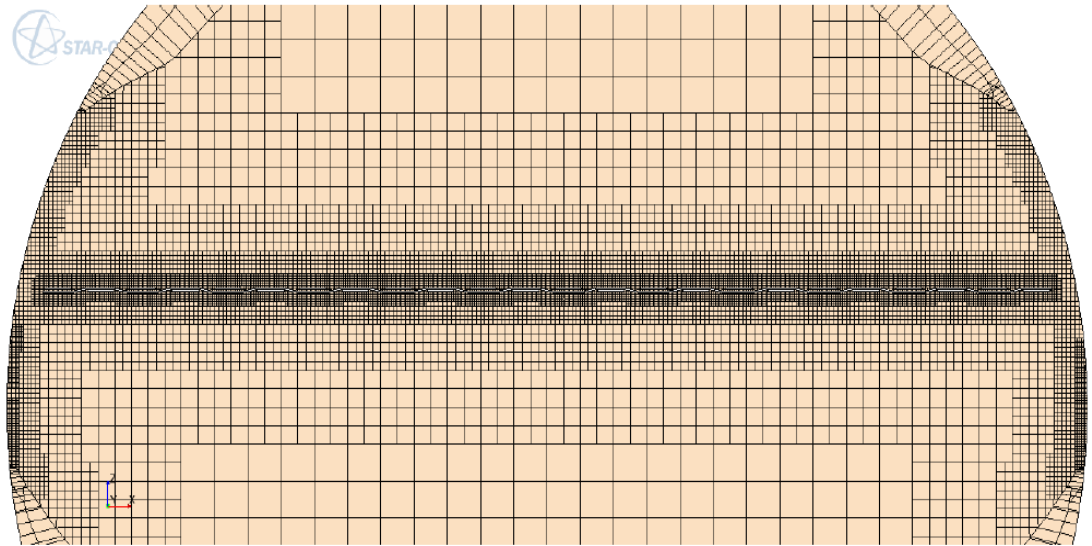


Figure 5.12 Mesh in the (x y) plane of the cylinder

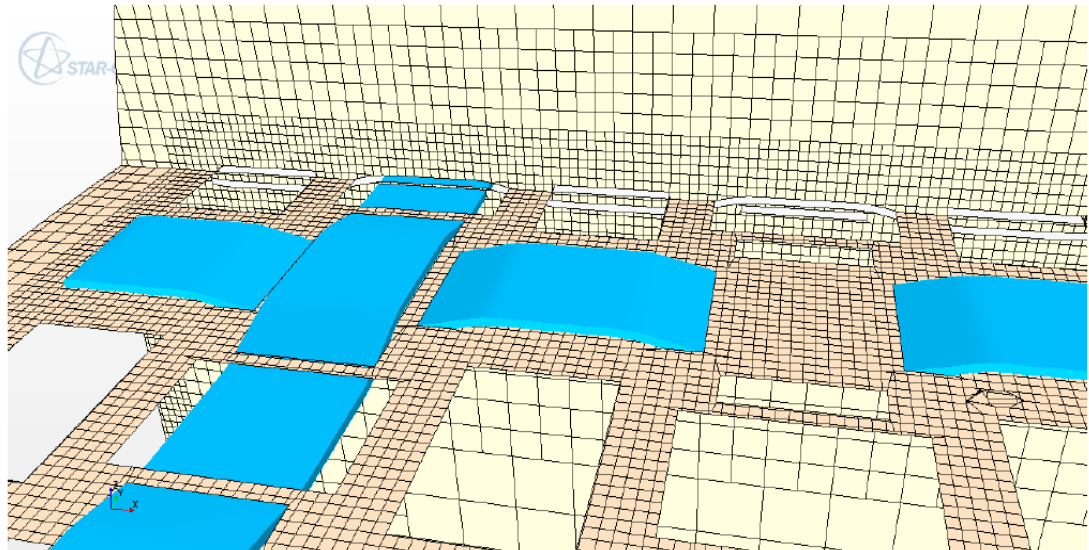


Figure 5.13 Mesh around the membrane

Table 5.3 Meshing parameters

	CYLINDER	MEMBRANE
Models	Prism Layer Mesher Surface Remesher Trimmer (hexahedra)	
Base Size (m)	0.08	0.05
Number of Prism Layers	2	10
Surface Curvature Growth Rate	1.3	1.3
Surface Size Template Growth Rate	Medium	Slow
Volumetric Control Trimmer Relative Size	2%	-
Growth Rate between MAPMD and the Fluid Domain	-	Slow

5.7. K-Epsilon Turbulence Model

The effect of turbulence on the fluid is modeled using the default K-Epsilon turbulence model. Here the transport equations are solved for the turbulent kinetic energy and also for its dissipation rate. The turbulence models in STAR-CCM+ are responsible

for providing closure of the governing equations in the turbulent flows.

Comparing to other turbulence models which computes flow field very accurately, K-Epsilon turbulence model uses Wall functions and offers good convergence rates with relatively less memory requirements. Furthermore, this model has proven to be adapted for performing flow problems around complex geometries.

5.8. Motion Model – Translation

The kind of motion applied to the tank is a longitudinal actuation. A field function is created by extracting the information from a .csv table Figure 5.14. This table displays the longitudinal velocity values for a body in Simple Harmonic Motion (SHM), whose governing equation is:

$$v = 2\pi a f \cos(2\pi f t) \quad (5)$$

Depending on the two phases of the experiments, the amplitude of actuation is either 1.8 mm or 3.0 mm. The frequency is set at 2 Hz for the two phases and the three cases.

Nodes	Values
[-] Motions	
[+] DFBI Rotation and Translation	
[+] High Amp Actuation	
Translation Velocity	\$\$XMotion30
Coordinate System	Laboratory
Managed Coordinate Systems	[]
[+] Superposing Motions	
[+] Low Amp Actuation	
Translation Velocity	\$\$XMotion18
Coordinate System	Laboratory
Managed Coordinate Systems	[]
[+] Superposing Motions	
[+] Stationary	

Figure 5.14 Motion model

5.9. DFBI

Dynamic fluid body interaction allows the body to move according to the forces, moments exerted by the fluid on the body. Six degrees of freedom solver included enables rigid bodies subjected to external forces to move accordingly. This motion is applied to the membrane to compare the result with the experimental approach. Physical parameters of the membrane such as moment of inertia, mass and Centre of mass is manually adjusted. These parameters are taken from CATIA V5. Body mass parameter is set initially at 0.013 kg based on data from CATIA, it is then altered to 0.0133871 kg based on experimental calculation. There are another two parameters in the DFBI, release time and ramp time. It is in best interest to allow some time for the fluid flow to initialize in order to avoid aberrant movements of the rigid body during the very first steps of the simulation. Release Time is the time before calculation of body motion begins. This duration depends on the time model and the mesh size. It should be used carefully since, on one hand, it can avoid the solution from diverging from the first iteration; on the other hand it can delay the movement of the body and distort the realistic validity of the simulation. In an unsteady model, the typical range would be a release after 10 to 50 time steps. Given the time step of 0.001 second and several tests which led to establish a suitable release time, this duration is set at 0.045 s. Ramp Time involves applying the forces and moments proportionally across the interval chosen to reduce the shock effect. It thus facilitates a more robust solution by reducing oscillation and shock effect caused by forces and moments applied to the body at release time. Ramp Time is set at 0.02s as shown in Figure 5.15. Both Release and Ramp time remain constant for both inactive and active simulation conditions.

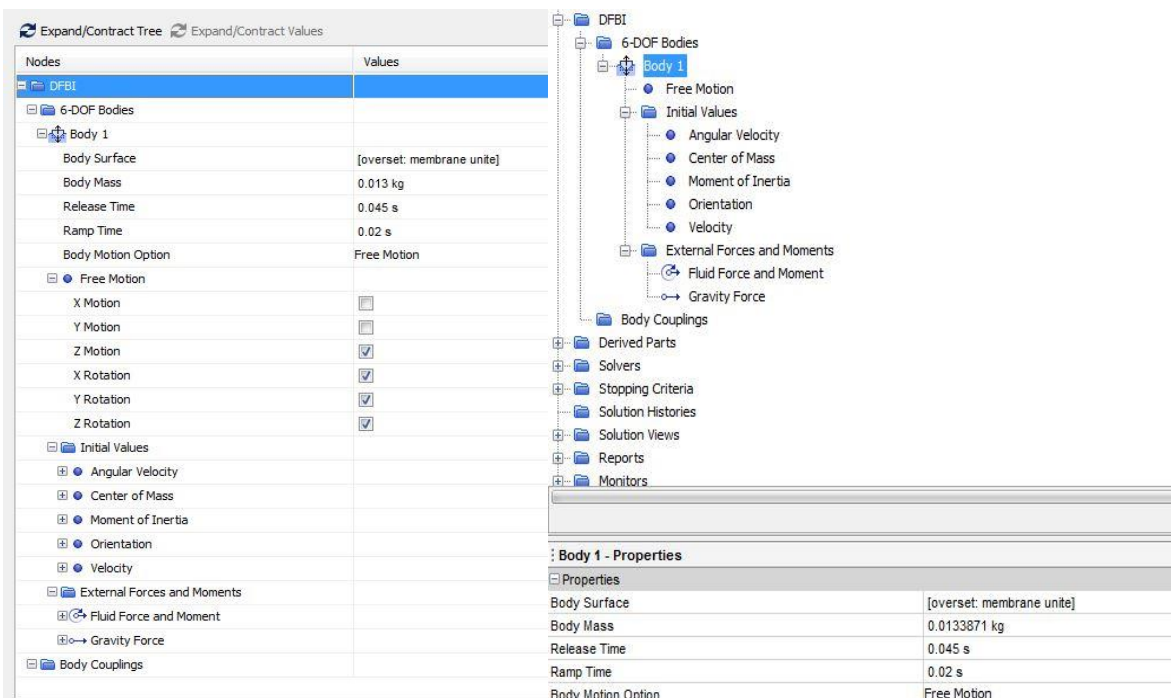


Figure 5.15 DFBI settings for initial and active condition

5.10. Eulerian Multiphase and VOF

The Eulerian Multiphase model is used in Star-CCM+ to reproduce the interaction between two phases present inside the tank: air and water. A phase is a form of matter, within a many-body system, characterized by relatively uniform physical properties. This model takes in account the numerous physical properties of the phases involved and the distinct interfaces between them.

Within the Eulerian Multiphase framework, the Volume of Fluid (VOF) model is applied to the simulation. VOF helps the user simulate immiscible free surfaces - such as the flow of fluid around the membrane.

5.10.1. Splitting of phases

In Star-CCM+, the cylindrical tank is placed so that the initial free surface of the liquid is located on the $z = 0$ plane level. Figure 5.16 shows the field functions `AirInitialVF` and `WaterInitialVF` created in Star-CCM+ and is responsible for describing the location for initial state of the volume of fluid within the simulation environment: water is located below the $z = 0$ plane while air is located above this plane.

Nodes	Values
Field Functions	
<ul style="list-style-type: none"> AirinitialVF <ul style="list-style-type: none"> Function Name: AirinitialVF Type: Scalar Dimensions: Dimensionless Definition: $(\\$Centroid[2] > 0) ? 1:0$ Inverse Distance Weight: <input type="checkbox"/> Assembly Code: $(if (> \\${Centroid}[2] 0) 1 0)$ Ignore Boundary Values: <input type="checkbox"/> WaterinitialVF <ul style="list-style-type: none"> Function Name: WaterinitialVF Type: Scalar Dimensions: Dimensionless Definition: $(\\$Centroid[2] < 0) ? 1:0$ Inverse Distance Weight: <input type="checkbox"/> Assembly Code: $(if (< \\${Centroid}[2] 0) 1 0)$ Ignore Boundary Values: <input type="checkbox"/> 	

Figure 5.16 Field Functions used for phase differentiation

5.11. Stopping Criteria

For periodic flow, an order of 50 to 100 time steps per period is appropriate. As the frequency of actuation is 2 Hz, the period of sloshing is 0.5 s. Therefore, time step of the simulation is considered in the range of 0.01 to 0.005 s. However, after running several simulations with this time step, it appeared that the water level had clearly and

visibly decreased between the beginning and the end of the calculation. As fluid was “lost”, the time steps were probably too high to ensure sufficient accuracy. Eventually, a time step at 0.001 s is found to be an acceptable compromise between rapidity of computation and precision.

5.12. Report Generation

Reports must be created before running the simulation in order to acquire the desired data such as the force exerted on the tank wall, the fluid maximum height, the tank position or the residuals that highlight the accuracy of the calculation. Reports provide summaries of current solution data. They enable engineering quantities such as drag, lift or mass flow to be computed. Monitors enable summary information from the simulation to be sampled and saved in the solution. They are useful for assessing and tracking the behavior of the quantities as the solution evolves. Several monitors are automatically created and appear in the corresponding node (Physical Time, Iteration, Continuity, etc.). This node also includes the monitors related to the K-Epsilon turbulence model. Plots are then generated from reports and offer a visual evolution of the studied quantities Figure 5.17.

Nodes	Values
Plots	
Plots	5
Output Verbosity	<input type="checkbox"/>
<input type="checkbox"/> Cylinder Position Monitor Plot	
<input type="checkbox"/> Force on Cylinder X-axis	
<input type="checkbox"/> Force on Cylinder X-axis Monitor Plot	
<input type="checkbox"/> Maximum Height Monitor Plot	
<input type="checkbox"/> Residuals	

Figure 5.17 List of plots

5.13. Convergence Criteria

Convergence is a critical criteria for any simulation. Simulation in general is an iterative process. Numerical equations are solved at node boundaries for every iteration. A common method for checking convergence is tracking the residuals for each individual variables that are being solved in the simulation. The residuals represent errors of a specific variable that is being solved in the simulation. Initially during the simulation, it is common for the residual value to increase; but if no decrease in residual is observed, then the simulation does not show convergence.

An acceptable rule of thumb for checking errors in a solution is to verify that the convergence lie in 3-5 order of magnitude. This is done by noting the value of the first residual which would be the maximum residual value and noting the drop in magnitude after few hundred iterations. Additionally, monitoring the drop in residual magnitude of other variables that are solved in the simulation would provide a good insight in simulation convergence.

5.14. Simulation Cases

Computational approach is again split into cases for this research. Primary reason for conducting the research as a case study is related to the drawbacks with the Overset Mesh in Star-CCM+.

First case involves free slosh conditions. In this case, physics models such as Eulerian Multiphase and VOF are primarily specified as it does not involve any interaction with a solid body. Apart from volume meshing, a cylindrical block is created along the tank wall and about the region of liquid and air phase interaction. Force on the tank walls due to liquid sloshing is measured from this surface. This is carried out to

replicate the presence of load cells and acquire data in the simulation environment. Iso-surface and Threshold option under Derived Parts section of the Simulation Tree allows the user to visualize the free surface motion.

The second case includes the MAPMD meshed membrane in simulation. In this case, overset mesh is used in conjunction with background volume mesh and DFBI to simulate motion of a solid body and its interaction with a liquid medium. Due to the issues with overset mesh, the membrane size has to be reduced to allow the interactions between Donor and Acceptor cells and hence the case study. In this case, MAPMD of different diameter sizes are compared and their effectiveness in slosh reduction is studied. For proof-of-concept purposes, MAPMD diameter sizes are increased in the order of 5mm starting from 160 mm and ending at 175 mm with a total of 4 cases are simulated. The membrane is considered as Wall throughout the simulation which directly relates to the Inactive membrane experiment case.

In the third case, physics, motion and boundary condition parameters identical to the second case are taken with an exception of physical time. In order to simulate magnetic field and study its effect on the membrane, it would require a complex simulation setup and in turn would drastically increase the computational time. To simplify the situation, magnetic field intensity on the membrane top surface is measured with a help of Tesla meter and converted into magnetic force. This force is then applied on the top surface of the cylinder after the initial actuation period of 6 seconds and the difference in slosh damping by the membrane under the force applied is studied. This case directly relates to the Active membrane experiment case.

5.15. Initializing the Simulation

Parameters are initially set for the simulation to be run and is saved as .sim file. An autosave condition is specified to save the results of the simulation for every 1000 iterations. This saved file can later be used to view results at the particular iteration, check for errors and change the parameters if necessary and be re-run.

This file is then imported into a High Performance Computing (HPC) Cluster available in Embry-Riddle Aeronautical University. The simulation is initialized by submitting a Portable Batch System script to the HPC cluster which specifies the file location and file name to be run. More details on the HPC cluster is provided in Appendix C.

6. Results and Discussion

6.1. Experimental Results

6.1.1. Signal De-Noising

Initial experiment was carried out for low amplitude free slosh case. In this experiment, focus was given towards signal analysis from the load cells. The primary objective of this case is to reduce the amount of noise peaks in the signals which may arise due to various sources present in and around the experiment setup. The forces and moments on the tank walls caused by the slosh may or may not have significant strength for the load cells to sense accurately since the load cells are of industrial standard capable of sensing up to 250 lbs of force or 1112 N.

Signals from the load cells pass through myDAQ and is presented in a readable format through LabVIEW while passing through a Low Pass Filter. This signal is then exported in the form of Microsoft Excel format to be further analyzed in MATLAB.

In MATLAB, further signal analysis is carried out in the hopes of reducing the noise peaks and obtaining a clear result. Butterworth filter is used in the MATLAB code for this purpose. It can be inferred from Figure 6.1 below that the Wavelets De-Noised Signal appears to be a free flowing graph as compared to the broken signal.

6.1.2. Test Cases Results

The load cell measures the force acting on the wall due to slosh waves as well as liquid body motion. This causes the plots to increase and decrease for few cycles before settling. Maximum slosh amplitude is taken from the difference between slosh peaks of higher intensity and the same is true for minimum slosh amplitude for determining

logarithmic decrement. To provide justifiable comparison between experiment and simulation results, logarithmic decrement calculation is performed by considering the slosh amplitude peaks after 6 seconds corresponding to remnant slosh damping.

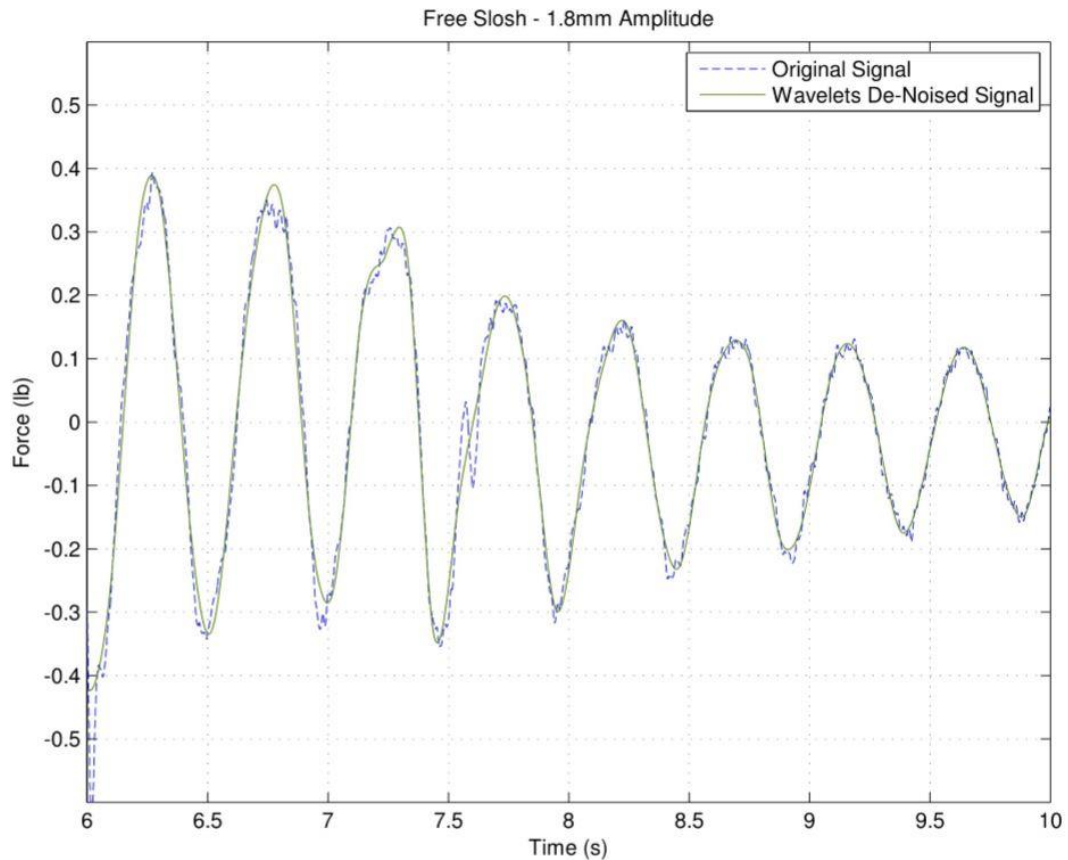


Figure 6.1 Comparison between Original and De-Noised signal

6.1.3. Interpreting Experimental Results

On overview of the experimental results plot, it can be noted that there are two events that are occurring simultaneously. First event is the measured slosh motion occurring at 2 Hz frequency. Second event is the frequency readings from the Aerotech Linear Motion Actuator (LMA) and is an actuator specific one. The two readings are superimposed over one another as slosh occurs due to the actuator motion and is an incidental externality. This occurs for every experimental case involved in this study and

only the slosh readings are taken into consideration for proof-of-concept purposes. The slosh peaks decrease after the actuation period and eventually smoothen out. The remaining spikes in the plot occurring at regular intervals is due to external noise from the actuator system.

For interpretation purposes, the experimental results can be divided into four phases as shown in Figure 6.2. Phase 1 (P1) depicts the initial actuator motion where the load cell measures the inertial forces on the tank as it starts moving with the actuator. Phase 2 (P2) is the natural frequency of the actuator. Phase 3 (P3) is the portion where the actuator stops and the forced frequency of the slosh starts to match the frequency of the actuator. Phase 4 (P4) is the resonant response of the slosh.

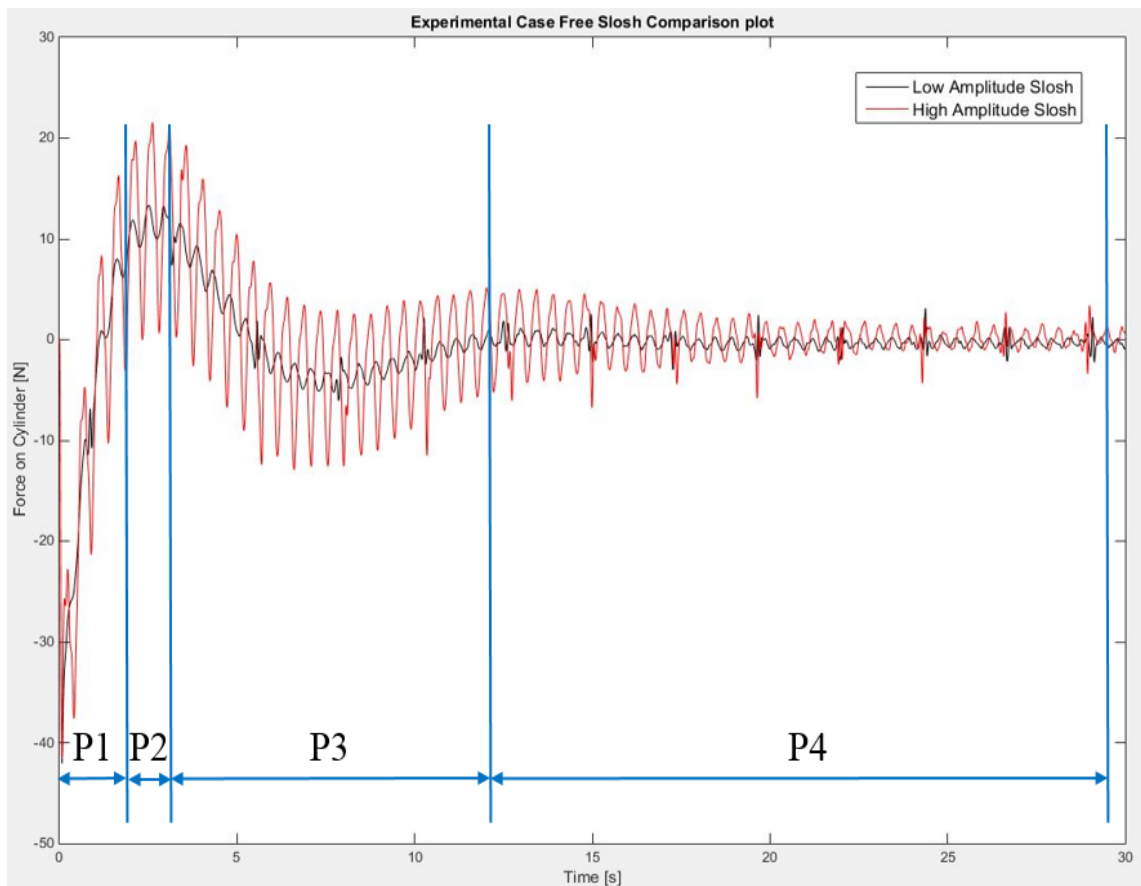


Figure 6.2 Experimental free slosh plot

Inactive Case: Sheet and Meshed Membrane

With the addition of passive baffle in the form of sheet and membrane, liquid surface experiences a semi-rigid surface that partially restricts its motion. Under low amplitude condition, both sheet and meshed membrane provide good damping with peak decrement in the ratio of 0.0838 and 0.1421. Percentage difference between sheet and meshed membrane is 69.57. The high frequency amplitude peaks occurring at regular intervals is due to external vibrations from the actuator system. Slosh waves are damped at a faster rate by the meshed membrane for low slosh condition.

A good co-relation between slosh amplitude peaks is observed for all three phases in high amplitude condition with meshed membrane producing higher damping with the ratio of 0.3664 as compared to the sheet with a ratio of 0.1120. Percentage difference between sheet and meshed membrane is 227.14.

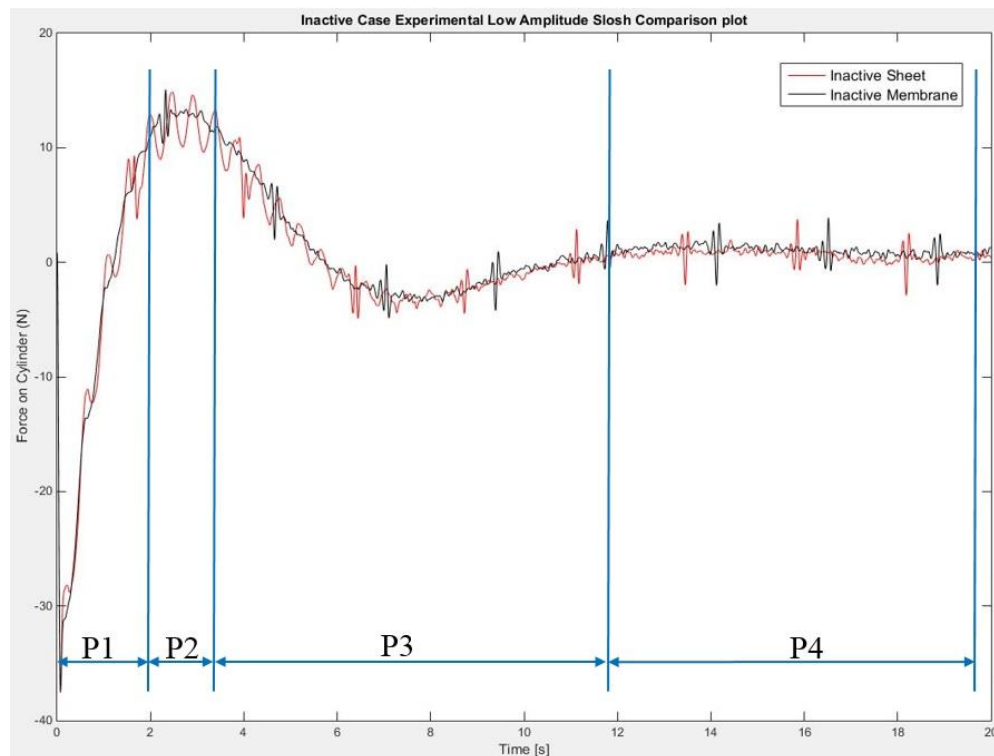


Figure 6.3 Experimental inactive low amplitude slosh plot

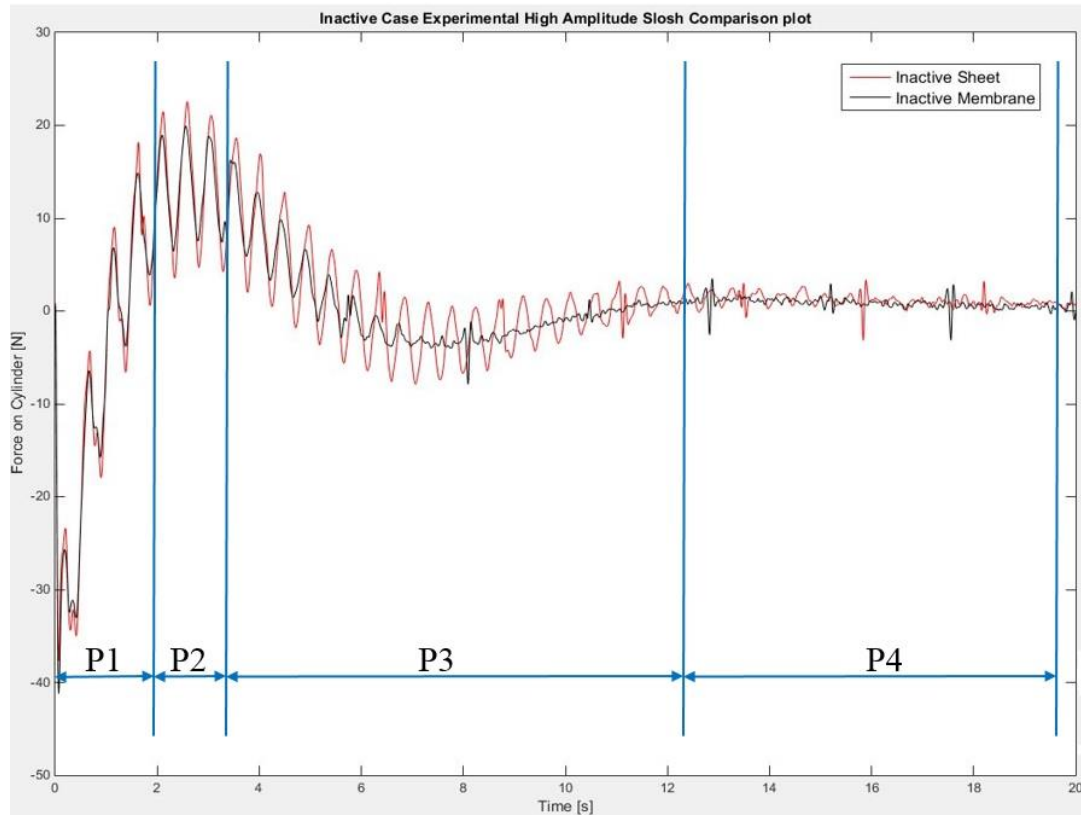


Figure 6.4 Experimental inactive high amplitude plot

Active Case: Sheet and Meshed Membrane

With the application of magnetic field at the end of actuation period, liquid surface experiences a downward push caused by the attraction of the membrane towards the electromagnet. This is similar to a small weighted object floating on top of the liquid surface restricting fluid motion beneath its entire surface area.

The meshed membrane has greater thickness at places where the weave overlaps. This increase in thickness increases its tendency of attraction towards the electromagnet. The added stiffness of the meshed membrane correlates well with the corresponding active damping plots with the decrement ratio of solid membrane in the range of 0.2772 and 0.3094 for low and high amplitude slosh. Logarithmic Decrement of active meshed membrane is in the range of 0.4424 and 0.3698 respectively.

Percentage difference between sheet and meshed membrane is 59.59 for low amplitude and 19.52 for high amplitude slosh.

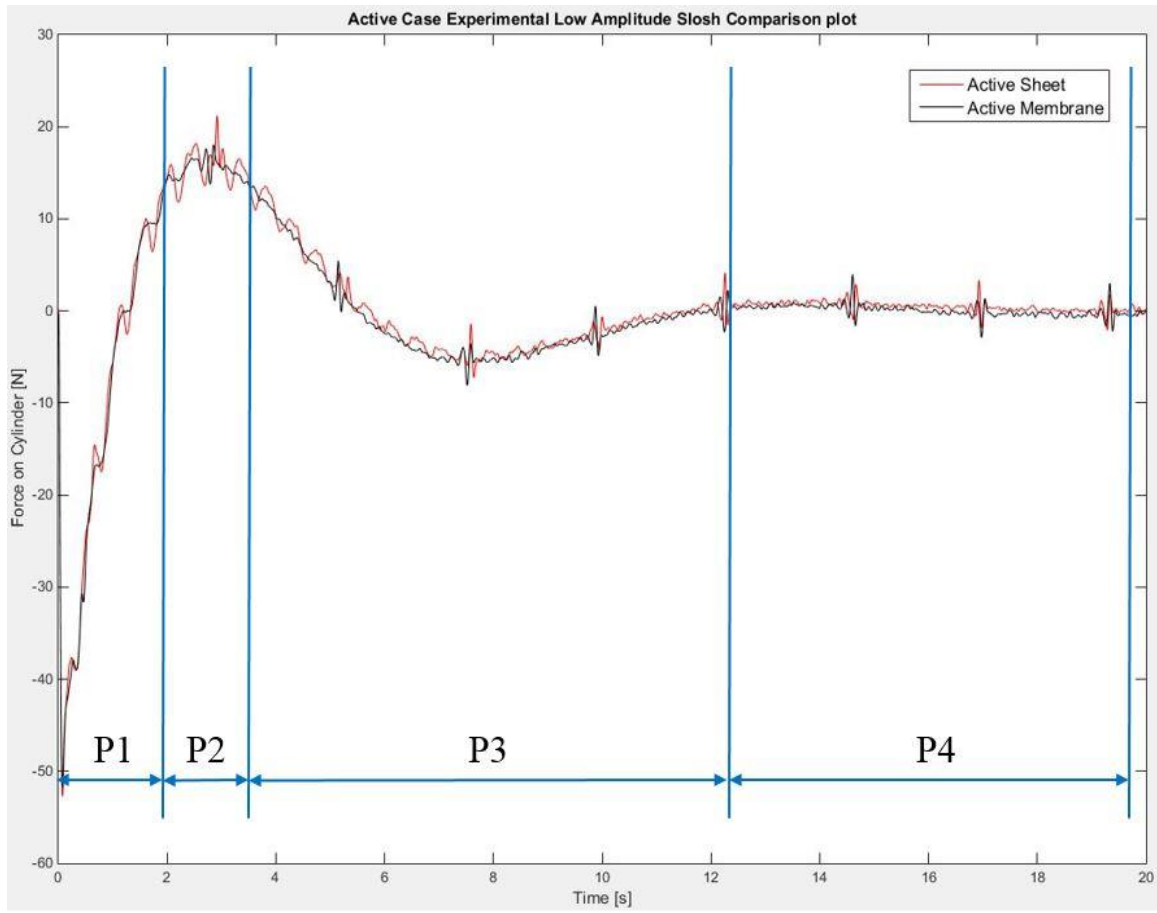


Figure 6.5 Experimental active low amplitude plot

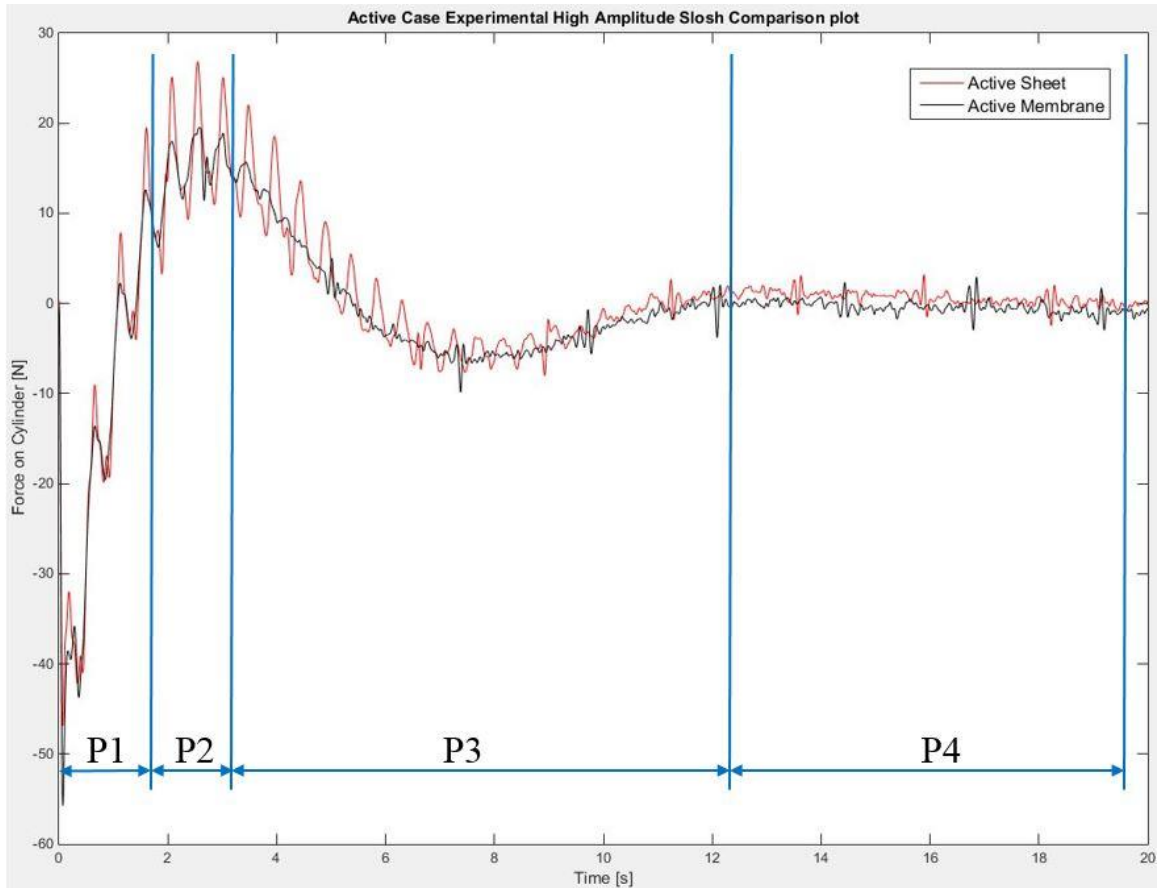


Figure 6.6 Experimental active high amplitude plot

6.2. Computational Results

6.2.1. Modal Analysis

Computational finite element modal analysis was performed to determine the mode shapes and stiffness characteristics of the Metglas MAPMD geometry used in this research. As described in the sections before, physical properties of the material were obtained from the manufacturer and geometry parameters from CATIA.

Mode 1 of the Static Structural Analysis shows the deformation contours of the mesh and solid model resembling a ridge shape that coincides with the deformation pattern of slosh mode.

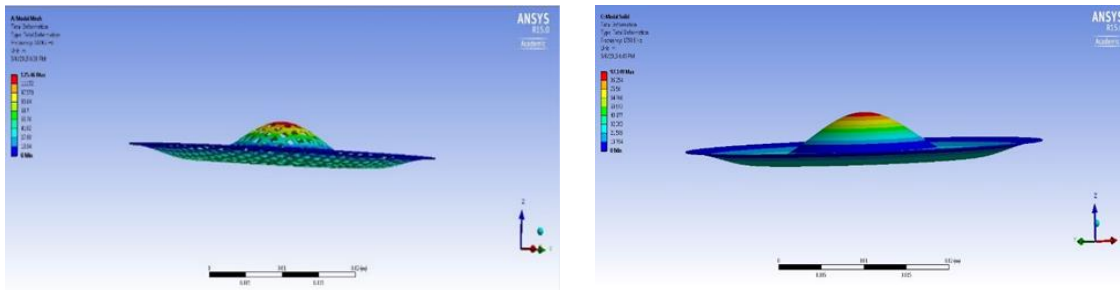


Figure 6.7 Mode 1 Displacements exhibited by Meshed Model (left) and Solid Model (right)

Mode 2 of the Static Structural Analysis shows the deformation contours of the mesh and solid model resembling a mountain shape that coincides with the deformation pattern of slosh mode.

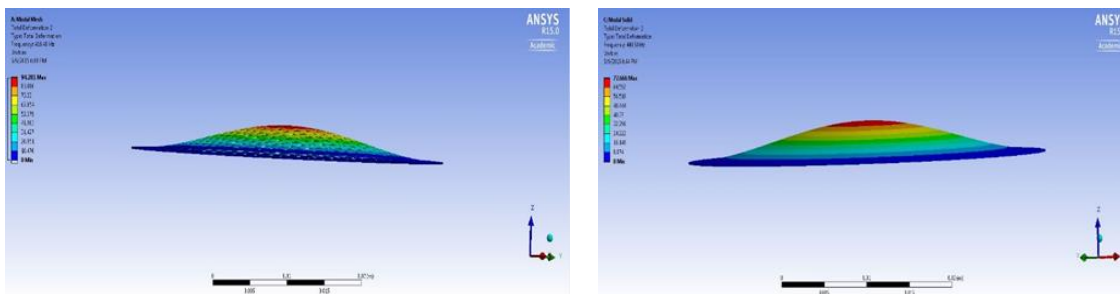


Figure 6.8 Mode 2 Displacements exhibited by Meshed Model (left) and Solid Model (right)

Mode 3 of the Static Structural Analysis shows the deformation contours of the mesh and solid model resembling a yin-yang shape in formation. It may be due to the fact that MAPMD has limited elastic property as compared to that of an elastomeric membrane.

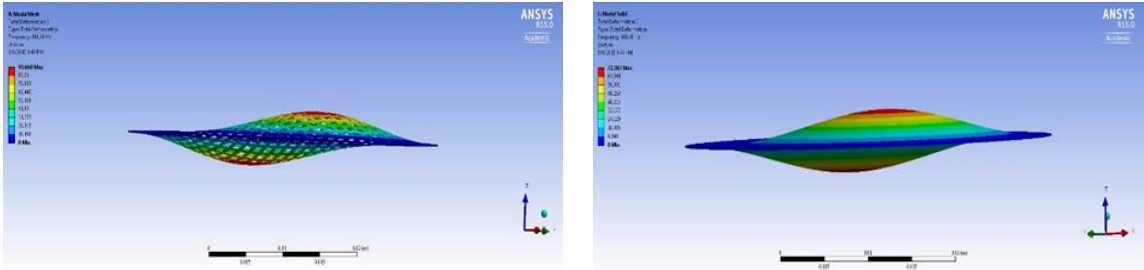


Figure 6.9 Mode 3 Displacements exhibited by Meshed Model (left) and Solid Model (right)

Mode 4 of the Static Structural Analysis shows the deformation contours of the mesh and solid model resembling a complete yin-yang shape that coincides with the deformation pattern of slosh mode.

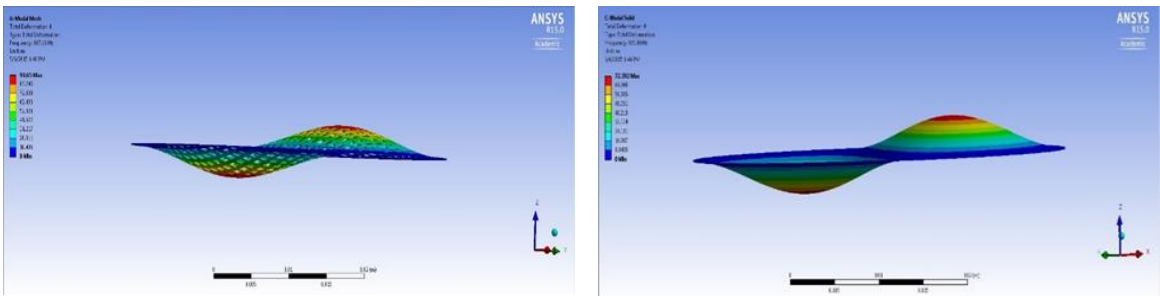


Figure 6.10 Mode 4 Displacements exhibited by Meshed Model (left) and Solid Model (right)

Mode 5 of the Static Structural Analysis shows the deformation contours of the mesh and solid model resembling both yin-yang and crater shapes. It is seen that modes 3 and 5 is an intermediate formation to a specific mode shape. Based on the property and characteristic differences between Metglas and an elastomer, it is safe to say that MAPMD deforms at a different rate than an elastomer for similar physics conditions.

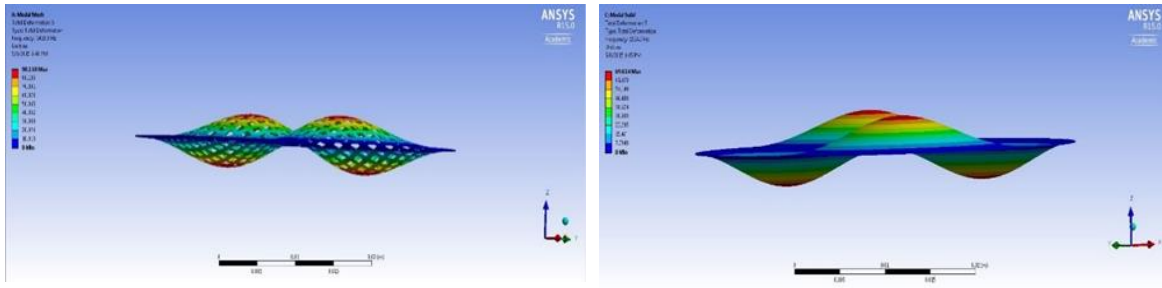


Figure 6.11 Mode 5 Displacements exhibited by Meshed Model (left) and Solid Model (right)

Mode 6 of the Static Structural Analysis shows the deformation contours of the mesh and solid model resembling a crater shape that coincides with the deformation pattern of slosh mode.

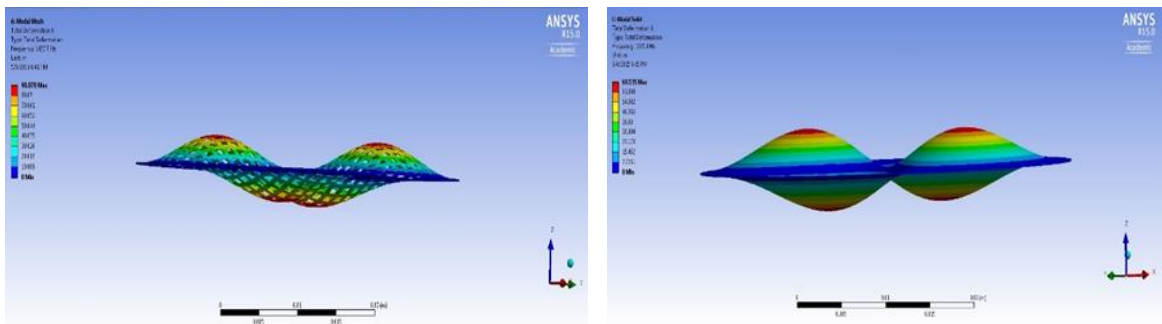


Figure 6.12 Mode 6 Displacements exhibited by Meshed Model (left) and Solid Model (right)

The modal analysis of MAPMD shows that the deformation patterns of mesh and solid membrane are similar but not the same. Mesh geometry offers better resistance to deformation than the Solid one. Summarization of data obtained from ANSYS for different modes and the calculated corresponding stiffness constant is shown on Table 6.1.

Table 6.1 Summarization of Meshed and Solid Model Data

Meshed Model				Solid Model			
Mode	Frequency, Hz	Mass, g	Stiffness, N/m	Mode	Frequency, Hz	Mass, g	Stiffness, N/m
1	416.49	0.68945	4.716624	1	449.58	1.0516	8.382698
2	866.66	0.68945	20.423001	2	935.48	1.0516	36.294338
3	867.16	0.68945	20.446573	3	935.98	1.0516	36.333146
4	1419.9	0.68945	54.819817	4	1534.7	1.0516	97.682519
5	1427.7	0.68945	55.42376	5	1535.9	1.0516	97.835337
6	1624.2	0.68945	71.73004	6	1750.9	1.0516	127

It can be observed from the plot below that solid MAPMD model has higher stiffness than meshed MAPMD model Figure 6.13. It is plausible that ANSYS had considered the mesh model to be a solid body with perforations and further analysis is needed to study this effect.

During experiments, the meshed MAPMD provided better resistance to liquid motion than the solid model thus validating the concept that meshed model offers better resistance to deformation than solid model as seen from the Modal Analysis.

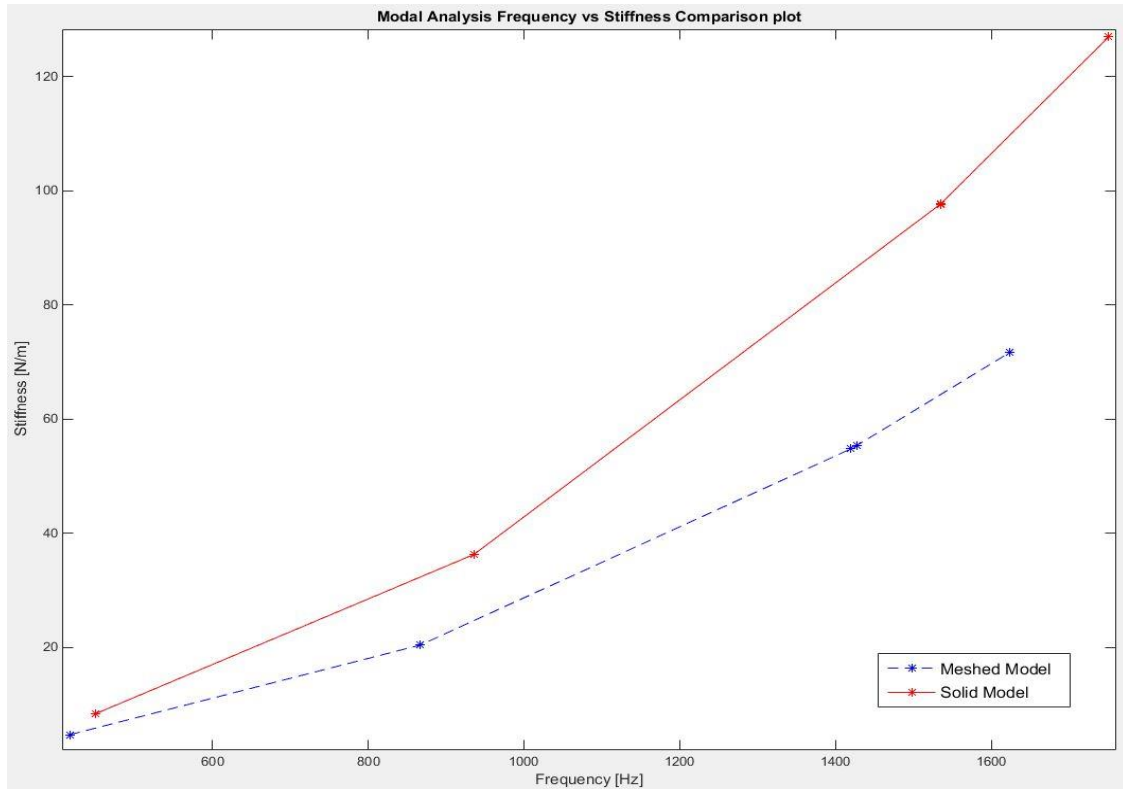


Figure 6.13 Frequency vs Stiffness comparison plot of Mesh and Solid MAPMD

6.2.2. Computational Fluid Dynamics Results

Simulation Convergence

In the carried out simulations, variables such as Continuity, Momentum along x, y and z direction, turbulent dissipation rate, Turbulent Kinetic energy and water force on tank are solved for and hence residuals from iterations are available. The residuals are plotted to check for convergence and errors in the simulation. Being a transient analysis, the residual plot shows a wave pattern with a gradual decrease in phase between peaks leading to a tight and concise pattern towards the end. After a point in time during the simulation, the values of the residuals remain constant. The magnitude of convergence for different variables are provided in Appendix B. The weighted residuals that are solved for in this simulation is shown in Figure 6.14.

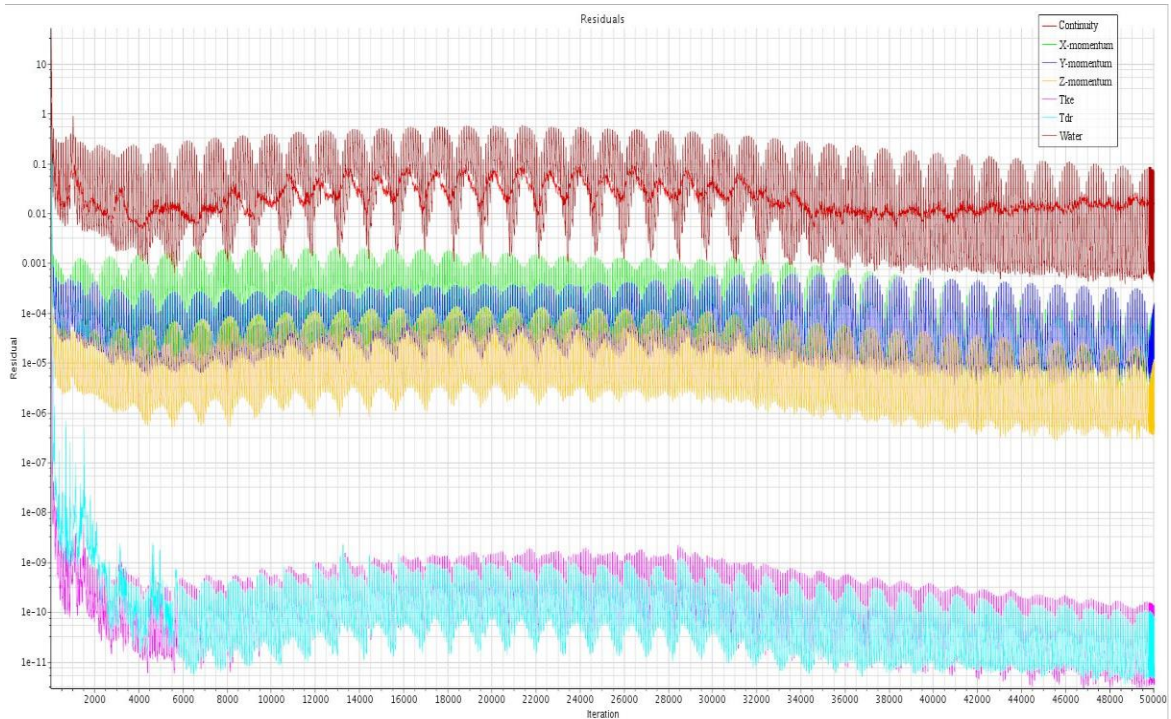


Figure 6.14 Sample Residuals plot depicting simulation convergence

Tank Motion

'x-motion 18' and 'x-motion 30' are the two motion data input as a .csv file in this simulation replicating the low and high slosh conditions. As seen from Figure 6.15, tank is actuated for 6 seconds of 'physical time' and remains still for 4 seconds of the total simulated time.

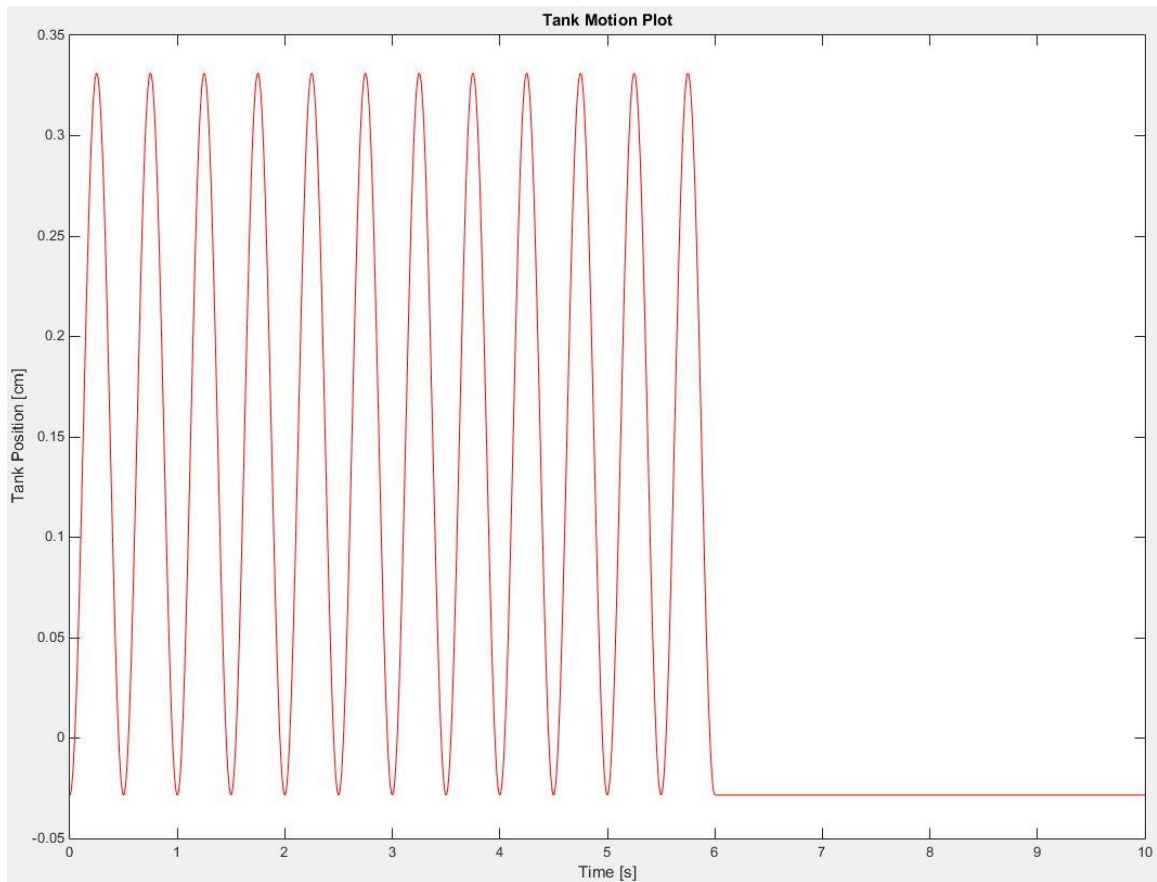


Figure 6.15 Tank motion during simulation plot

Free Slosh

First case of computational simulation revolves around free slosh. It presents the opportunity to layout a simulation template to be used for later cases involved in this research. To simulate low slosh condition, 'x-motion 18' is chosen as the Physics Value under 'Cylinder-Tank Wall-Region'. Same procedure is repeated for high slosh condition with the choice of motion as 'x-motion 30'.

Free Slosh comparison for low and high slosh conditions are presented in Figure 6.16. It can be inferred from the plot that force peaks are in sync during initial actuation and tend to go out of phase towards the end. This situation is caused by liquid motion under different amplitudes and hence the difference. Amplitude reduction for high slosh

condition occurs at a faster rate than low slosh condition with the slosh peaks remaining in sync.

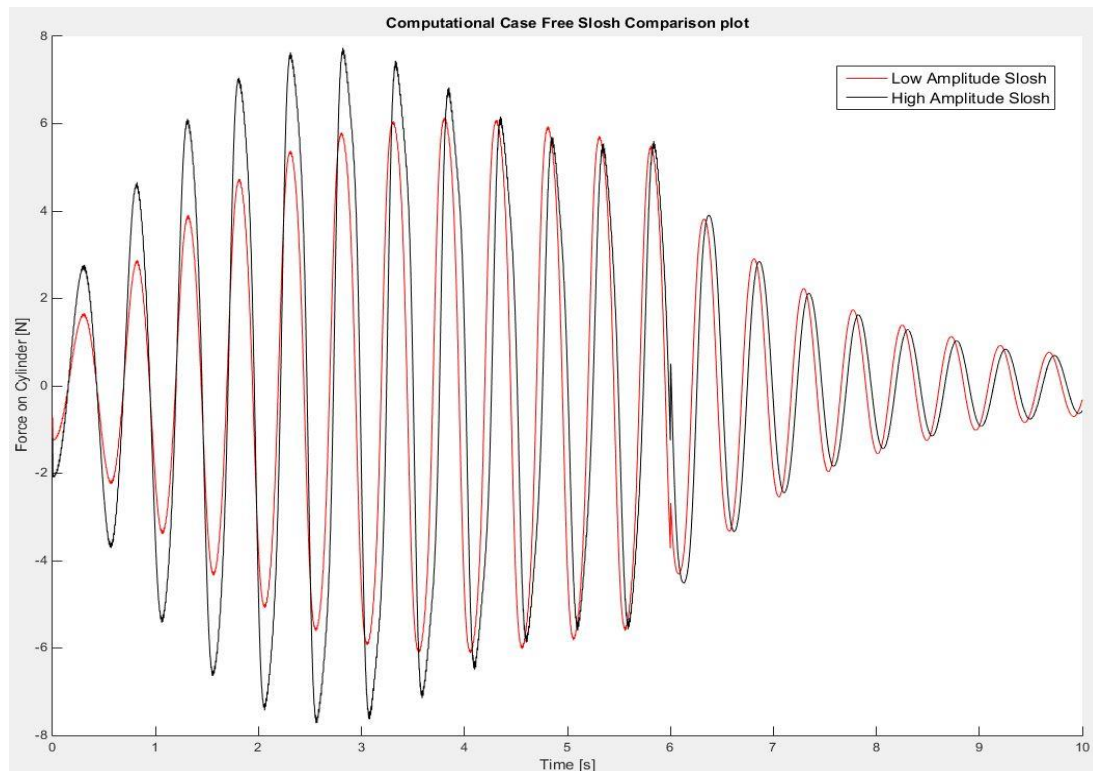


Figure 6.16 Computational free slosh comparison plot

Case Study: Low Amplitude (Inactive)

Owing to the difficulty presented by Overset Mesh, the membrane diameter is reduced from its original designed dimension. Hence a case study is conducted for membrane diameters of 160 mm, 165 mm, 170 mm and 175 mm to understand the influence of size variations on slosh reduction. The membrane as a whole is considered as a wall and hence STAR-CCM+ considers it to be one surface instead of a surface with gaps. This prohibits water from entering the gaps during the simulation. This condition replicates the experimental situation where the mesh is embedded within a polymer membrane preventing water from entering the gaps between the strips and is

unconstrained from the tank wall.

Figure 6.17 shows the comparison plot of different membrane diameters for low amplitude case study. On overview, the slosh peaks are synchronous with each other with no variations in sight.

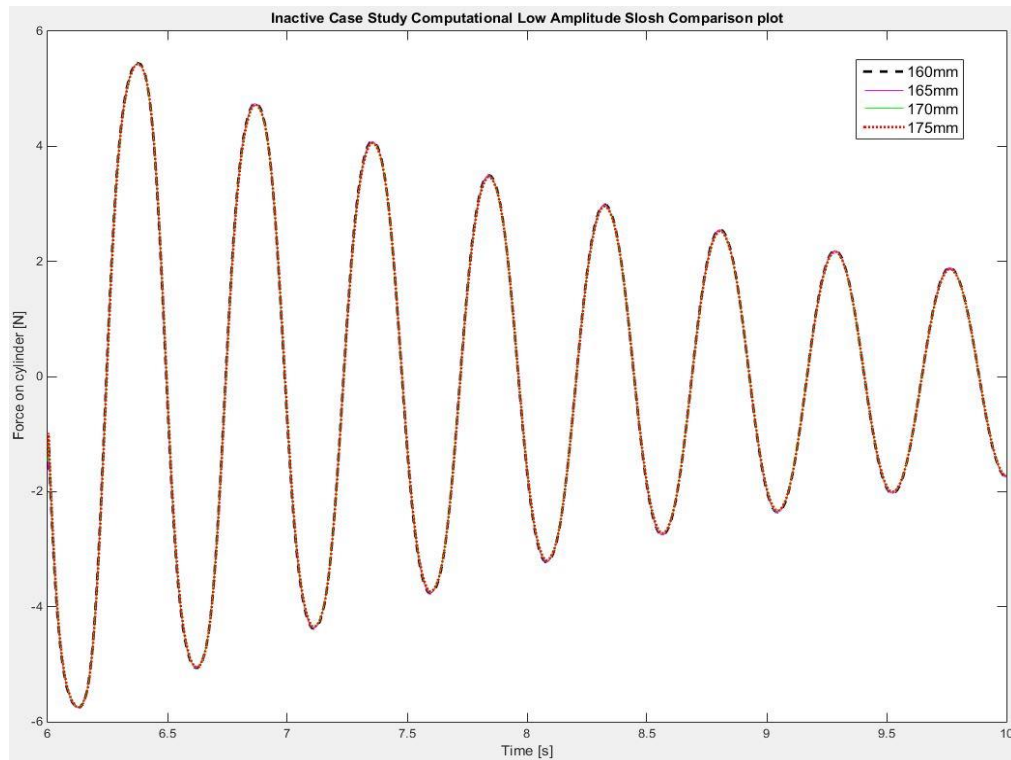


Figure 6.17 Computational low amplitude inactive case study plot

However, focusing in on slosh peak for a specific time frame reveals that there is indeed subtle variations in the plot. Figure 6.18 reveals the damping difference for different membrane diameter. At a particular peak height, diameter of 175 mm exhibits higher effectiveness in lowering the slosh amplitude than 160 mm diameter. Effectiveness of 165 mm and 170 mm diameter fall in-between the other ones with each of them following suit with respect to their size variations. Percentage difference between 160 mm and 175 mm is 0.83.

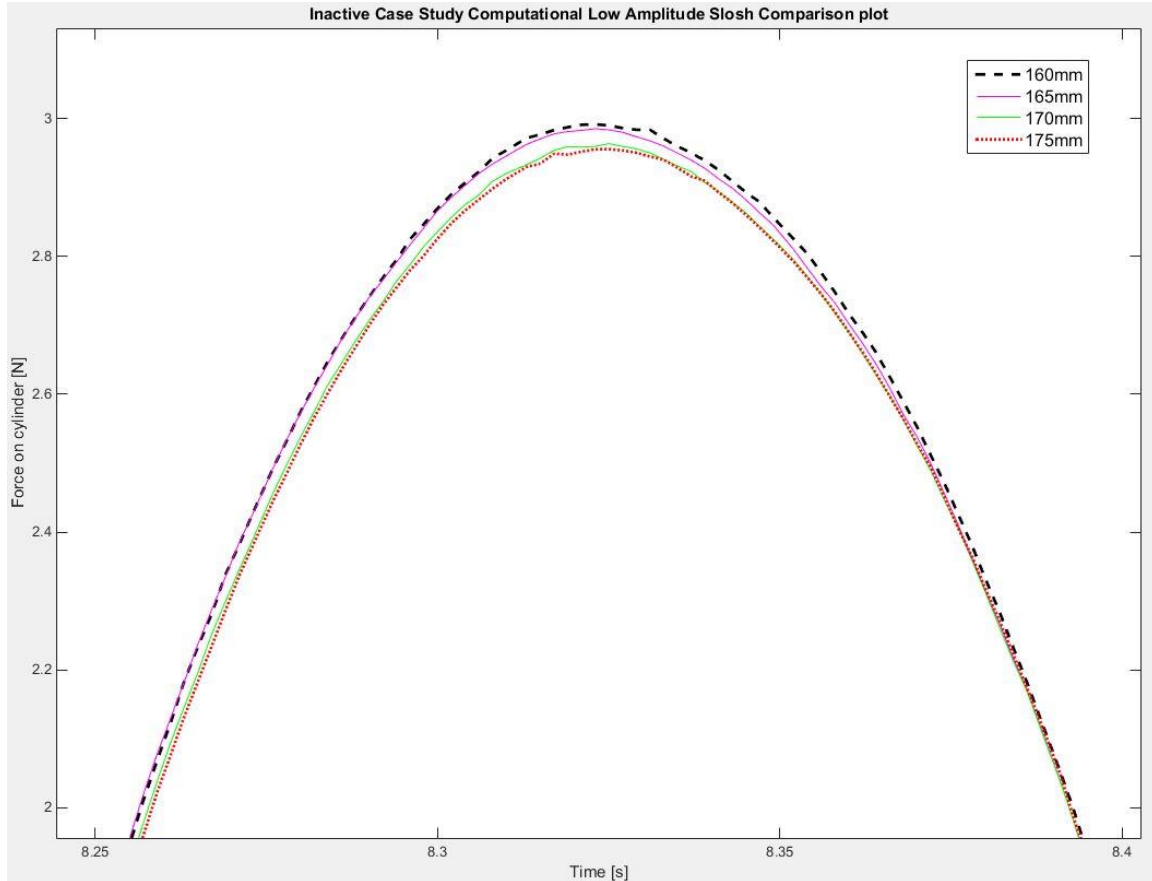


Figure 6.18 Slosh peak in focus for computational low amplitude inactive case study

Case Study: Low Amplitude (Active)

To simulate Active condition, mass of the membrane is altered in DFBI settings under Degree of Freedom node from 0.013 kg to 0.0133871 kg based on experiment calculation. This provides an overall increase of 2.97 % in membrane mass. To simulate low slosh condition, 'x-motion 18' is chosen as the Physics Value under 'Cylinder-Tank Wall-Region'. Other boundary conditions remain unaltered.

The plot below depicts the force results from active low slosh simulation condition. Again, no visible deviation and synchronous peaks in the plot is seen. This can be attributed to the fact that slosh wave amplitudes are low in this condition.

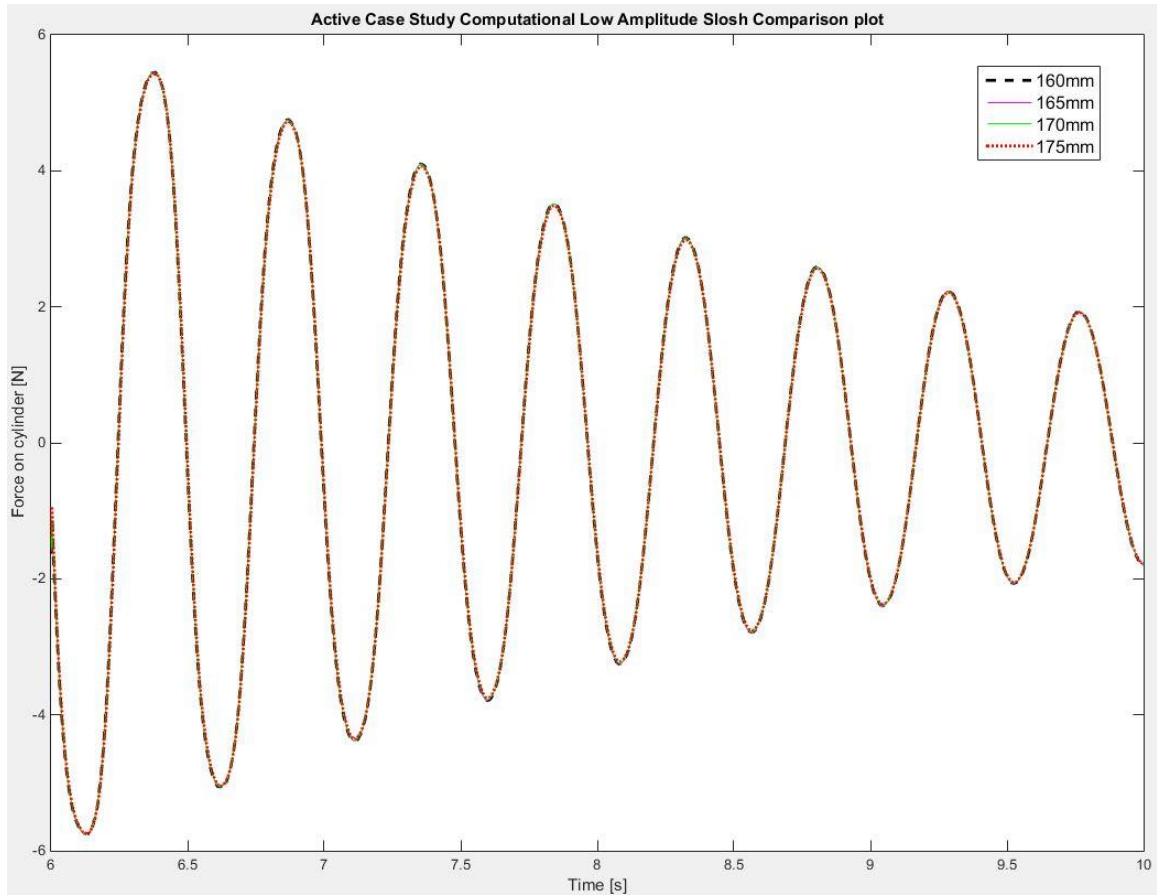


Figure 6.19 Computational low amplitude active case study plot

Focusing in on slosh peak for a specific time frame reveals once again that there is indeed subtle variations in the plot. Figure 6.20 reveals the damping difference for different membrane diameter. At a particular peak height, similar results from inactive condition is seen such as the diameter of 175 mm exhibiting better effectiveness in lowering the slosh amplitude than 160 mm diameter. Percentage difference between 160 mm and 175 mm is 61.38.

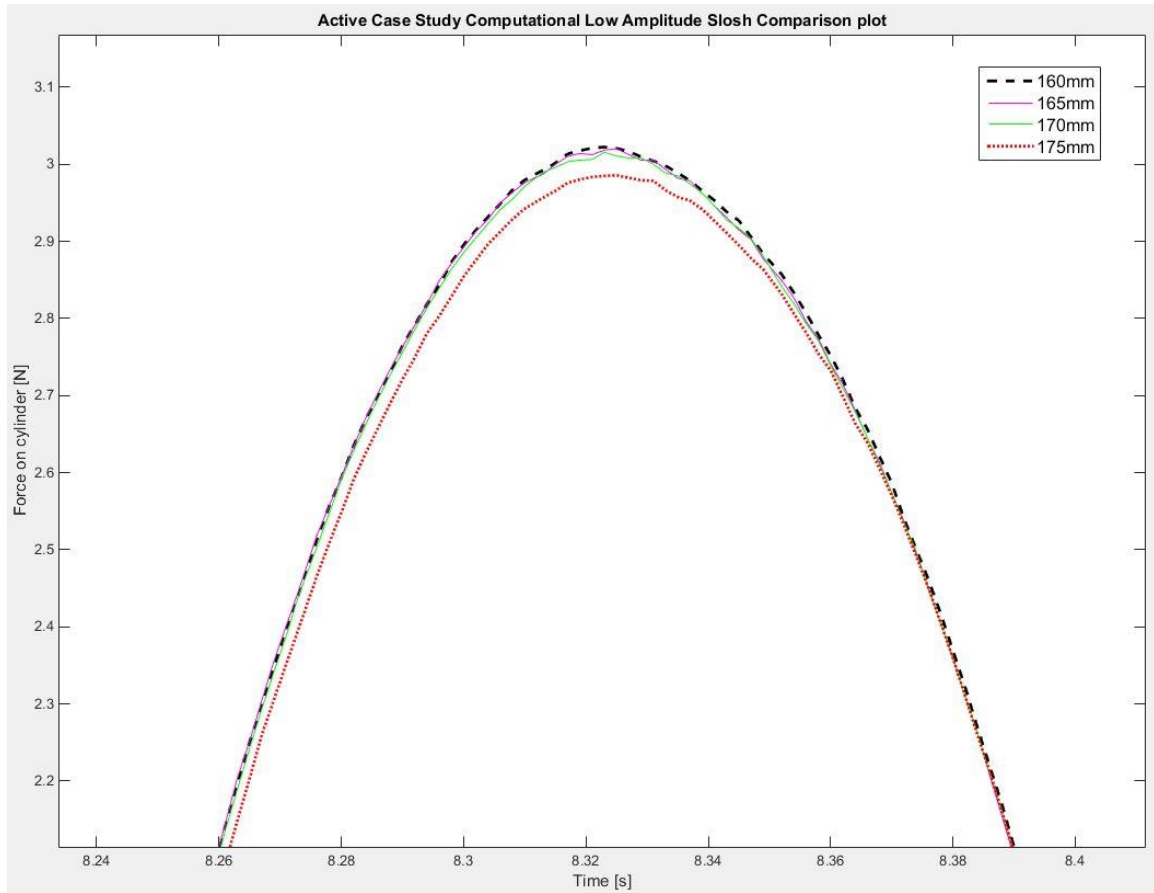


Figure 6.20 Slosh peak in focus for computational low amplitude active case study

Case Study: High Amplitude (Inactive)

Figure 6.21 shows the comparison plot of different membrane diameters for high amplitude case study. On overview, the slosh peaks are synchronous with each other with little variations in peak height, clearly seen, arising towards the end of simulation.

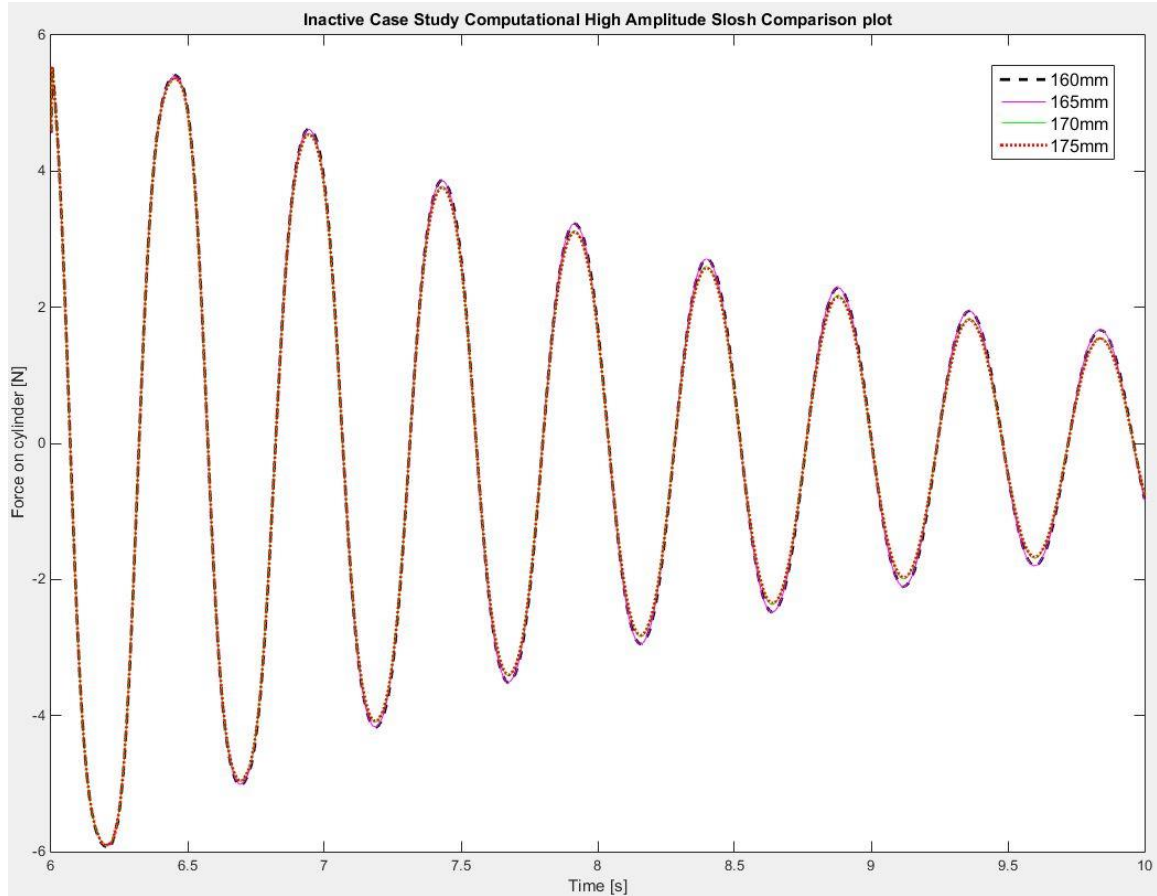


Figure 6.21 Computational high amplitude case study plot

Focusing in on slosh peak for a specific time frame reveals that there is indeed a considerable variation in the plot. Figure 6.22 reveals the damping difference for different membrane diameter. At a particular peak height, diameter of 175 mm exhibits higher effectiveness in lowering the slosh amplitude than 160 mm diameter. Effectiveness of 165 mm and 170 mm diameter fall in-between the other ones with each of them following suit with respect to their size variations. Also noticeable is that peak heights of 160 mm and 165 mm, 170 mm and 175 mm are nearly in synchronous with each other with a considerable peak height difference between the said pair. Percentage difference between 160 mm and 175 mm is 6.05.

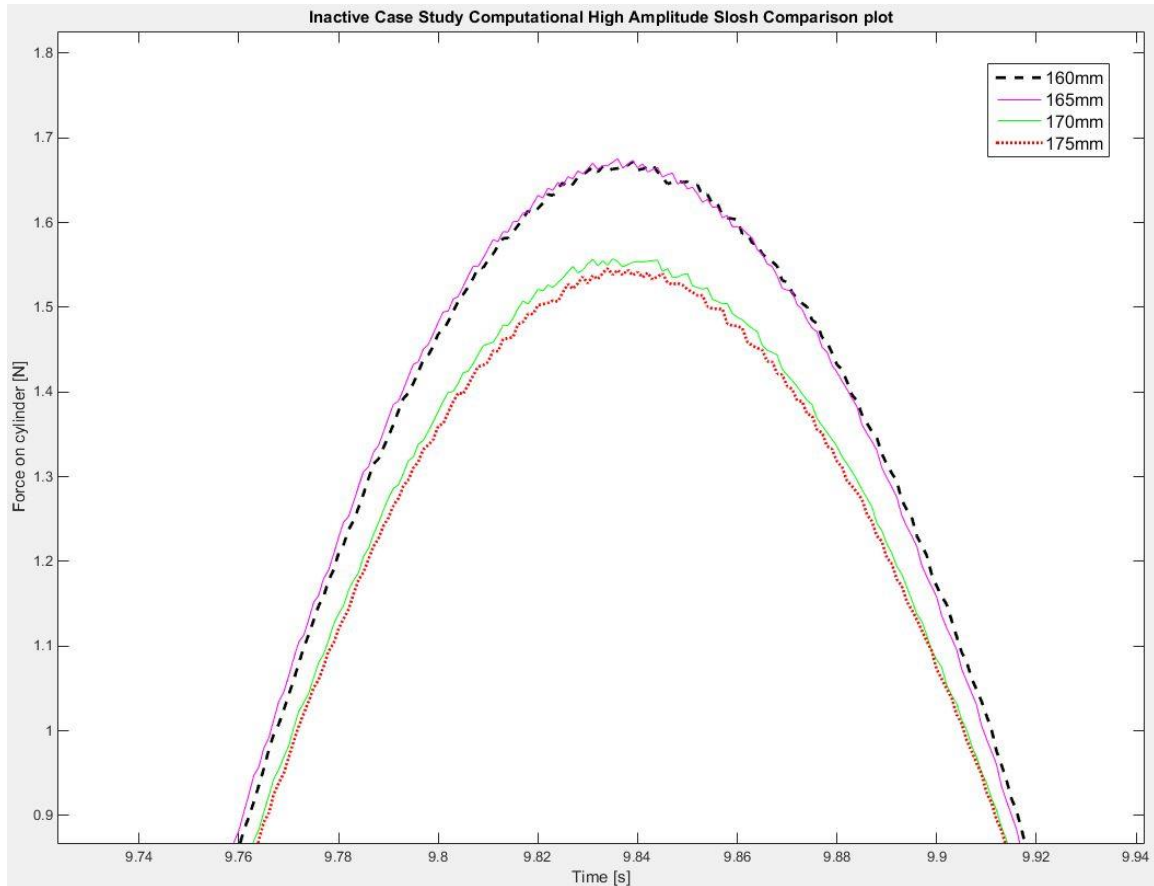


Figure 6.22 Slosh peak in focus for computational high amplitude case study

Case Study: High Amplitude (Active)

To simulate High Amplitude Active condition, ‘x-motion 30’ is chosen as the Physics Value under ‘Cylinder-Tank Wall-Region’ with the membrane set at 0.0133871 kg under DFBI node. This provides an overall increase of 2.97 % in membrane mass.

The plot below depicts the force results from active high slosh simulation condition. A visible deviation in the reduction of slosh amplitudes between the membranes of different diameters are seen. It can be inferred from the plot that the membrane diameter of 175 mm under high amplitude active condition provides better reduction in slosh amplitude than other diameter membranes. It can be attributed to the fact that at 175 mm the membrane allows for greater coverage of the free surface area of

the liquid under simulation conditions. Percentage difference between 160 mm and 175 mm is 65.24.

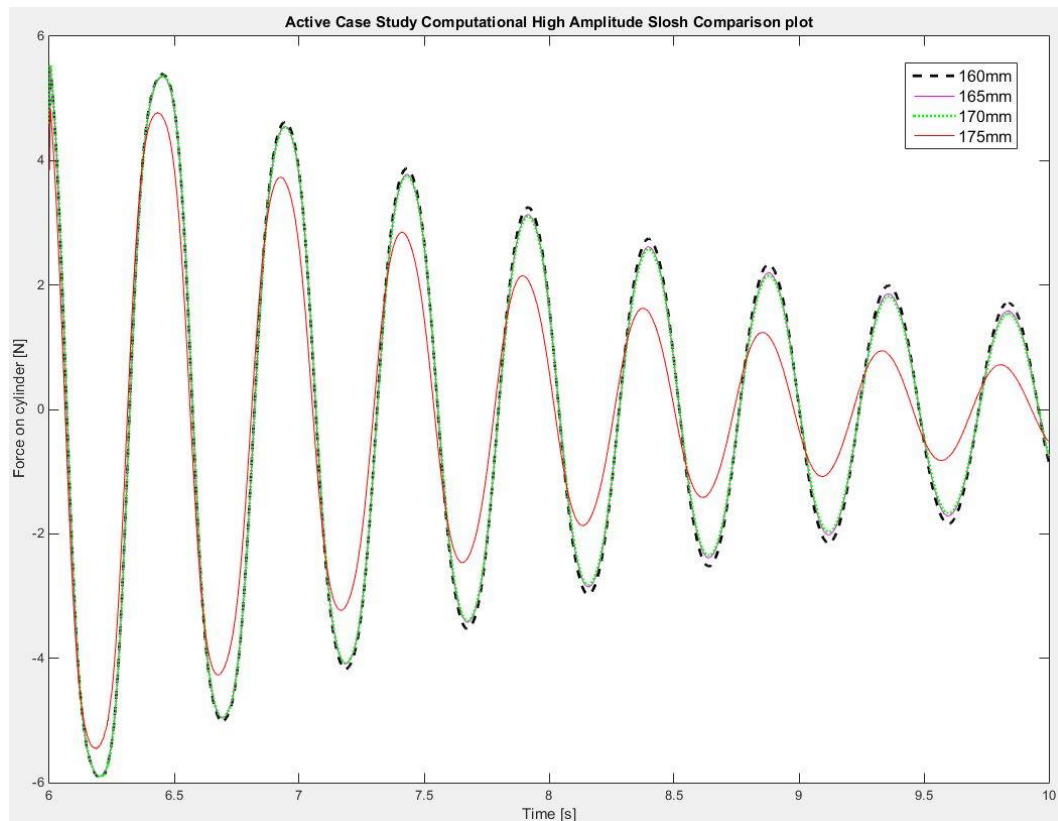


Figure 6.23 Computational high amplitude active case study plot

6.3. Comparison of Experimental and Computational Results

For comparison purposes, computational results of 175 mm membrane diameter is used against experimental results. The simulation does not take into account the forced frequency of the actuator system and represent only the natural frequency of the slosh.

6.3.1. Free Slosh Case Comparison

In Phase 1, experimental amplitude peaks begin out of phase with simulation amplitude peaks during the start of actuation. In Phase 2 and 3, the peaks start to co-relate after the actuation period. As seen from the plot, experimental low slosh condition has a

lower amplitude throughout the time period with a logarithmic decrement value of 0.0854 as compared to that of 0.0962 from simulation.

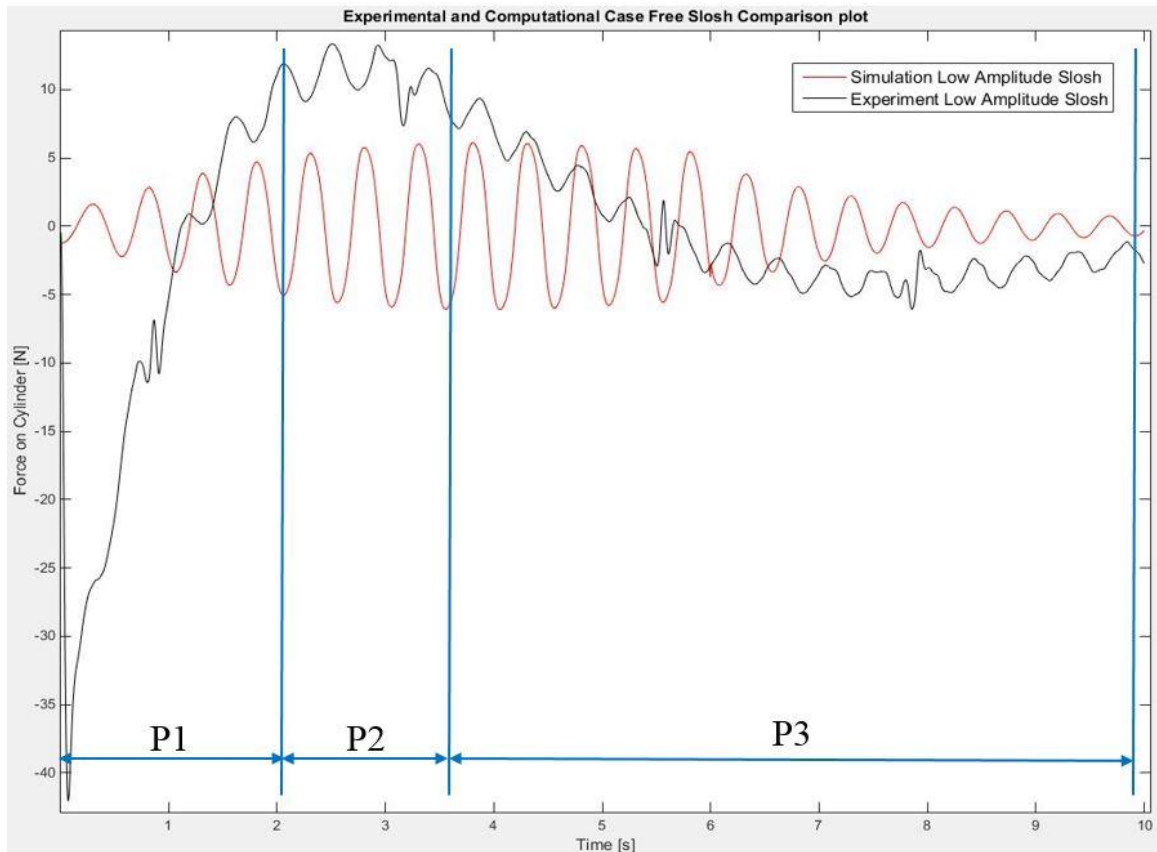


Figure 6.24 Low amplitude free slosh comparison plot

High amplitude condition shows a good co-relation between experimental and CFD setup with experimental slosh peaks remaining in-phase throughout the simulated time period. Simulated condition provides higher damping of slosh peaks with a logarithmic decrement value of 0.2158 as compared to 0.0266 from experimental condition. Natural damping of high slosh condition exceeds that of simulated condition with slosh peaks remaining at a higher amplitude.

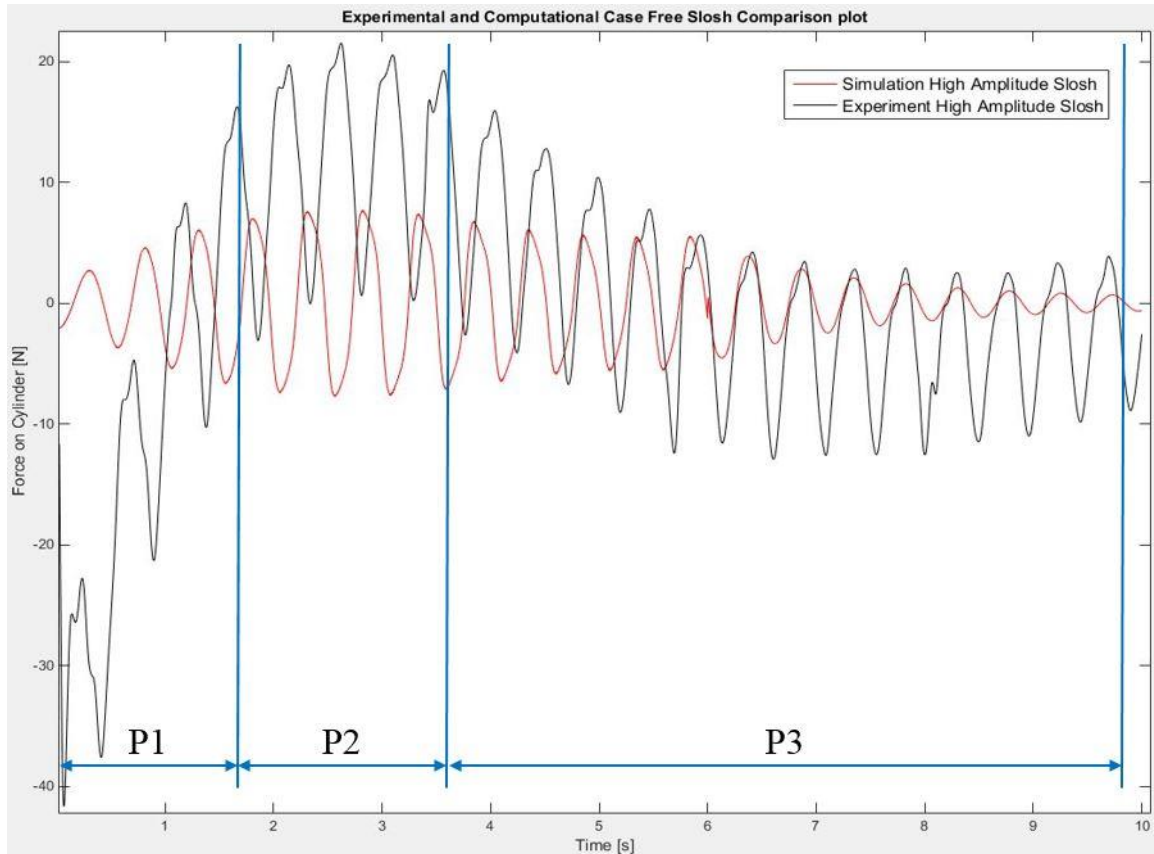


Figure 6.25 High amplitude free slosh comparison plot

6.3.2. Inactive Case Comparison

Slosh peaks remain in-phase until damping condition occurs with experimental membrane condition providing higher damping than simulated condition. Logarithmic decrement value of experimental sheet condition is 0.0838, membrane condition is 0.1421 and simulation value is 0.1332 respectively.

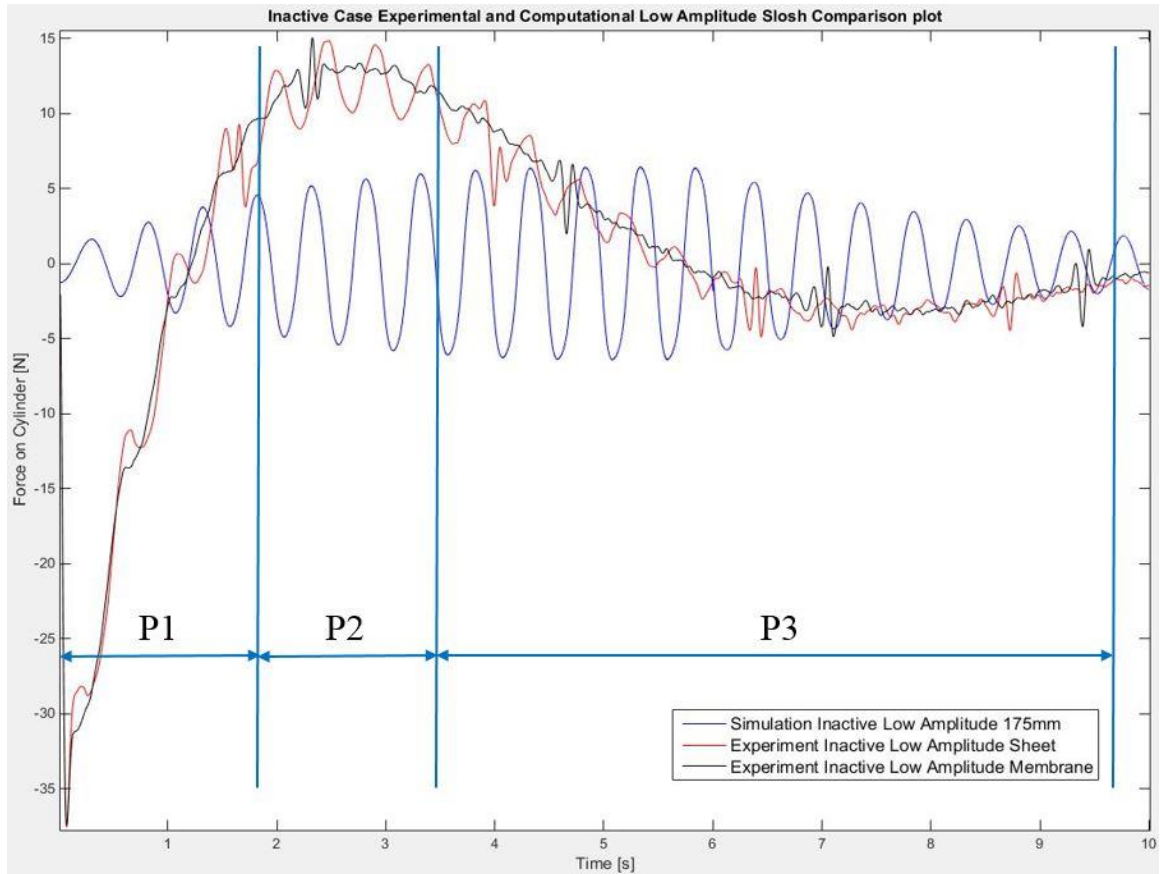


Figure 6.26 Inactive case low amplitude comparison plot

It can be inferred from the plot that under high amplitude inactive condition, peak amplitude value of experimental and simulated membrane are similar for all the three phases. This condition yields in-phase peaks until the end of actuation period.

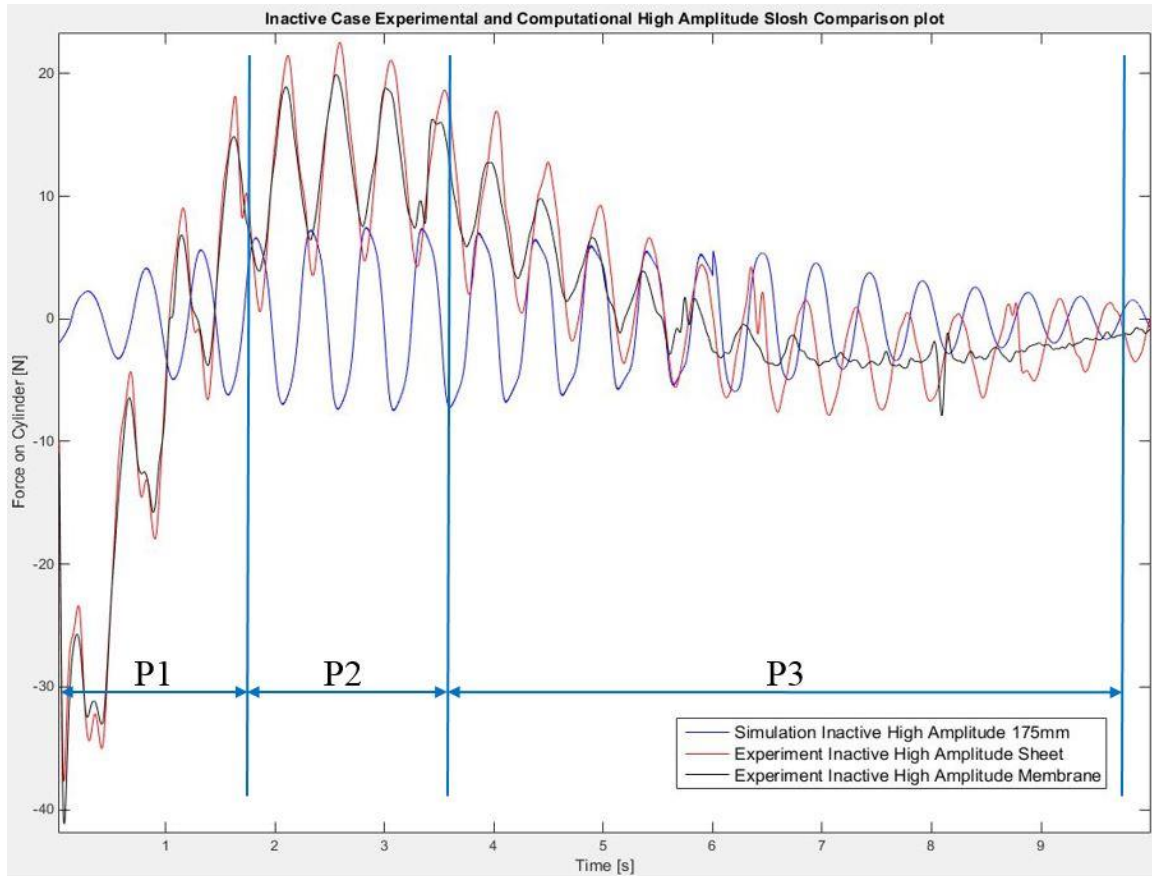


Figure 6.27 Inactive case high amplitude comparison plot

6.3.3. Active Case Comparison

It is clear from low amplitude comparison plots that experimental sheet and meshed membrane provides better damping as compared to that of simulated membrane. This can be attributed to the fact that in simulation, the membrane does not cover the entire surface area of liquid. Under high amplitude active condition, experimental meshed membrane provides superior damping than solid mesh and simulated membrane. From comparison plots it can be seen that meshed membrane is more rigid and thus provides better damping than other conditions.

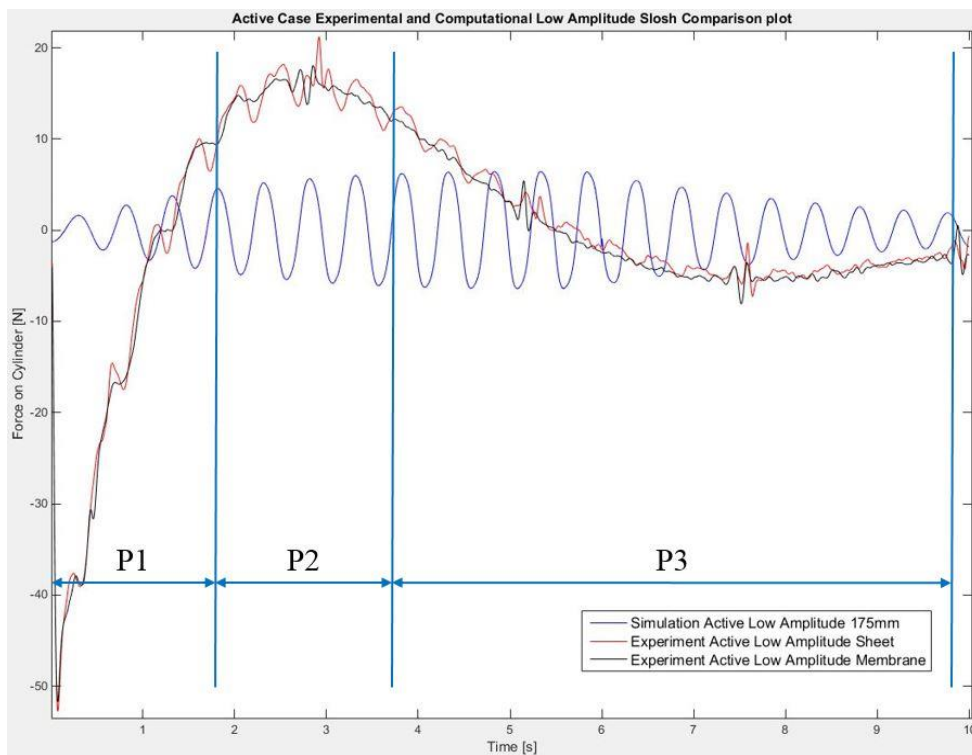


Figure 6.28 Active case low amplitude comparison plot

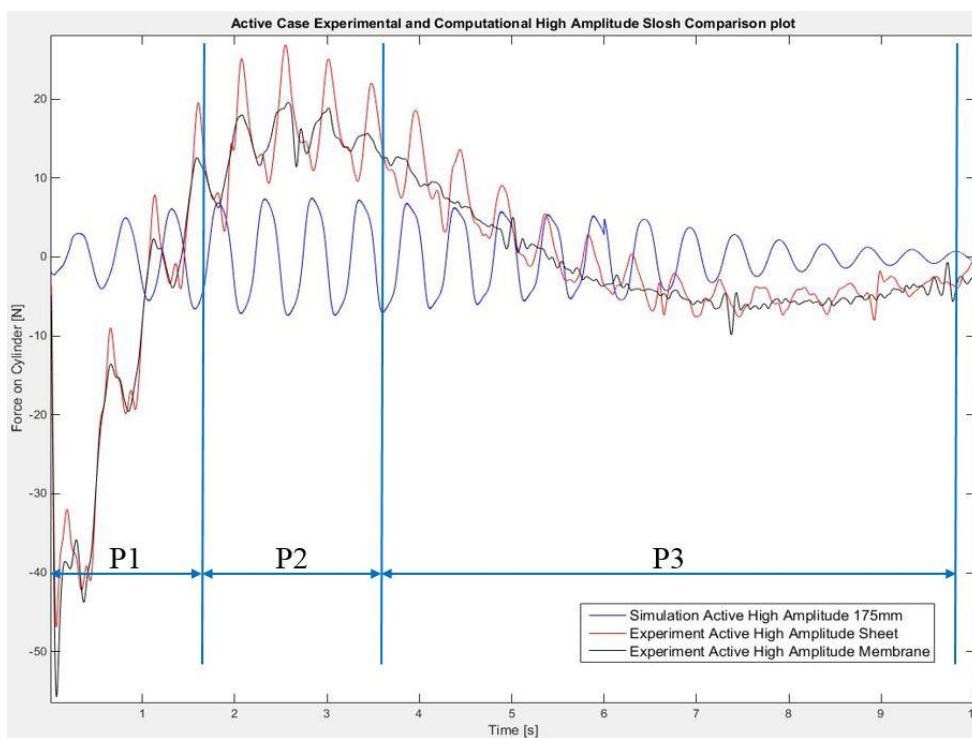


Figure 6.29 Active case high amplitude comparison plot

6.4. Damping Calculation

Damping is described as the dissipation of energy by a material experiencing cyclic stress conditions. A generally used method to measure the damping of a system in a time domain is logarithmic decrement. It represents the rate at which the amplitude of a free damped vibration decreases. In this research, damping is calculated from the plot of Force on Cylinder vs Time to obtain the damping ratio (ζ). The damping ratio represents the time taken by the remnant slosh to return to its equilibrium state.

From the Force on Cylinder [N] vs Time [s] plot, slosh peaks after 6 seconds of actuation is accounted for remnant slosh damping calculation. In this calculation,

- n is the number of peaks
- x_1 is the amplitude of the first peak after 6 seconds
- x_{n+1} is the amplitude of the $(n + 1)^{th}$ peak

Logarithmic decrement between the first and the $(n + 1)^{th}$ peak is defined as:

$$\delta = \frac{1}{n} \ln \left| \frac{x_1}{x_{n+1}} \right| \text{ and } \delta = \frac{2\pi\zeta}{\sqrt{1 - \zeta^2}}$$

Rearranging the above equation, damping ratio ζ (dimensionless) is obtained:

$$\zeta = \frac{\delta}{\sqrt{4\pi^2 + \delta^2}}$$

Table 6.2 Damping calculation summary for experimental low slosh condition

Case (Low Slosh)		n	Peaks (N)		Log Decrement δ	Damping Ratio ζ
			x_1	x_{n+1}		
Free Slosh		8	1.505335	0.760325	0.0854	1.36×10^{-2}
Inactive	Sheet	8	1.73859	0.888965	0.0838	1.33×10^{-2}
	Membrane	8	0.5633175	0.18071	0.1421	2.26×10^{-2}
Active	Sheet	8	1.219275	0.132795	0.2772	4.41×10^{-2}
	Membrane	8	0.912586	0.026503	0.4424	7.02×10^{-2}

Table 6.3 Damping calculation summary for experimental high slosh condition

Case (High Slosh)		n	Peaks (N)		Log Decrement δ	Damping Ratio ζ
			x_1	x_{n+1}		
Free Slosh		8	7.913015	6.396945	0.0266	4.2×10^{-3}
Inactive	Sheet	8	5.91449	2.41362	0.1120	1.78×10^{-2}
	Membrane	8	1.5746515	0.083955	0.3664	5.82×10^{-2}
Active	Sheet	8	3.5634755	0.299876	0.3094	4.92×10^{-2}
	Membrane	8	1.288655	0.066893	0.3698	5.88×10^{-2}

Table 6.4 Damping calculation summary for computational low slosh condition

Case (Low Slosh)		n	Peaks (N)		Log Decrement δ	Damping Ratio ζ
			x_1	x_{n+1}		
Free Slosh		8	3.814323274	1.7671807	0.0962	1.53×10^{-2}
Inactive	160	8	5.45728605	1.89441459	0.1323	2.10×10^{-2}
	165	8	5.4420577	1.89466765	0.1319	2.10×10^{-2}
	170	8	5.44327723	1.87269723	0.1334	2.12×10^{-2}
	175	8	5.42745831	1.87003618	0.1332	2.12×10^{-2}
Active	160	8	5.45782287	1.93724287	0.1295	2.06×10^{-2}
	165	8	5.44625416	1.93530873	0.1293	2.06×10^{-2}
	170	8	5.446872657	1.928162594	0.1298	2.07×10^{-2}
	175	8	5.437317046	1.002187682	0.2114	3.36×10^{-2}

Table 6.5 Damping calculation summary for computational high slosh condition

Case (High Slosh)	n	Peaks (N)		Log Decrement δ	Damping Ratio ζ	
		x_1	x_{n+1}			
Free Slosh	8	3.909567833	0.695858538	0.2158	3.43×10^{-2}	
Inactive	160	8	5.413002129	1.671900069	0.1469	2.34×10^{-2}
	165	8	5.39683263	1.675368902	0.1462	2.33×10^{-2}
	170	8	5.372594645	1.557264291	0.1548	2.46×10^{-2}
	175	8	5.371078815	1.544215663	0.1558	2.48×10^{-2}
Active	160	8	5.39653928	1.72383095	0.1427	2.27×10^{-2}
	165	8	5.371078815	1.546074737	0.1557	2.48×10^{-2}
	170	8	5.362856453	1.591332078	0.1519	2.42×10^{-2}
	175	8	4.779190967	0.724592167	0.2358	3.75×10^{-2}

Table 6.6 Percentage increase in damping ratio from Free Slosh

		% increase from Free Slosh			
		Experimental Low Slosh	Experimental High Slosh	Computational Low Slosh	Computational High Slosh
Active	Sheet	124.264	17.142	-	-
	Membrane	216.176	39.999	119.750	9.267

Table 6.7 Logarithmic Decrement comparison between Magnetoactive Micro-Baffles and Magneto-Active Propellant Management Device

			Log Decrement δ		
			Magnetoactive Micro-Baffles	Magneto-Active Propellant Management Device	% difference
Active	Sheet	Experimental Low Slosh	0.314	0.2772	-11.71
		Experimental High Slosh	0.354	0.3094	-12.59
	Membrane	Experimental Low Slosh	0.314	0.4424	+40.89
		Experimental High Slosh	0.354	0.3698	+4.46
		Computational Low Slosh	0.615	0.2114	-65.62
		Computational High Slosh	0.660	0.2358	-64.27

Percentage difference in damping between the Magnetoactive Micro-Baffles and Magneto-Active Propellant Management Device provides a good understanding between the two hybrid PMDs. Both these concepts involve floating PMDs with the differences in Micro-Baffle having a greater thickness than membrane and membrane providing a better coverage of liquid surface area in the tank than the baffle.

In experimental phase of the comparison, the Micro-Baffles move along with the liquid slosh motion but do not cover the entire liquid surface area in the tank during the test cases. This provided a positive difference towards membrane due to its greater surface contact with the liquid.

In simulation phase, the Micro-Baffles were arranged in an order and constrained along their six Degrees-Of-Freedom (DOF). Unlike the membrane the Micro-Baffle did not move along with the slosh motion and its added thickness provided a better resistance to the slosh motion. This resulted in a negative percentage difference to the membrane.

7. Conclusion

In this research study, initial design and development of Magneto-Active propellant Management Device (MAPMD) as a viable propellant management device along with proof of concept experiments is carried out.

The concept of a hybrid membrane acting as a semi rigid structural layer under the influence of an external magnetic field floating on top of the liquid surface is laid out. For a material to react under magnetic field, based on previously conducted studies, importance is given to the property of its permeability. Material selection study based on the physical property of permeability, and its availability is carried out and Metglas 2605SA1 was found adept for this research. The material obtained for the study resembled that of a sheet metal but with much smaller thickness. Manufacturing the membrane based on the initial design seemed to a tedious process as the material was found hard to be cut under Band Saw, knife edge and even scissor edges. Hence surface analysis of Metglas 2605SA1 was carried out under Scanning Electron Microscope to understand its composition and study the cut edges. It was noted that the irregular cut edges displayed shear deformation along the grain boundaries due to improper shearing force. This also had caused macro tears along the edges that were brittle. These macro tears were seen to be proceeding along the grain boundaries with no deformation to the cut surface. To cut the material, a pair of scissors with rigid shear edges were used to produce even cut edges.

Prior to conducting the experiment, the load cell used in the slosh test bed setup was calibrated and a coefficient was found which when integrated with the custom made LabVIEW code displayed the results directly in Newton. Experiments were then carried

out for three mentioned test cases with membrane models as a solid and as a meshed membrane. Computational Fluid Dynamics simulation was carried out in this research using STAR-CCM+. Initial mesh study was conducted to justify the simulation setup and convergence condition. However due to initial issues involving overset mesh, a case study involving membrane of different dimensions were conducted to study the effect of membrane size in slosh damping. To replicate the active condition in simulation, an experiment was made to calculate the force acting on the membrane due to the magnetic field produced by the electromagnet, but with air as the medium in-between. The setup was found to be favorable as both air and water possess similar relative permeability. The obtained result was compared to that of a calculated one and was found to be in the same order of magnitude. This force result was then converted into mass and added onto the simulation for replicating the experimental active condition setup.

The load cell used in the experiment setup was rated for 250 lbs or 1112 N, but the force measurements in experiments were in the range of +20 to -20 N. This led to the external noise peaks being amplified and more prevalent in the collected data. However, experiment and simulation results were found to be co-relating well.

For free slosh condition, simulation results provided higher damping ratio than that of the experiment. Under low amplitude conditions, the results were vice versa. In spite of forming a thin layer on top of the liquid surface, under active condition, both sheet and meshed membrane provided good damping to the slosh motion.

8. Recommendations for Future Work

As FUTEK LCM 300 Load Cell is rated for 250 lbs or 1112N, its accuracy should be studied and the resulting factor is to be accounted for in the future experiments. Issues with overset mesh conditions should also be explored. A better mesh geometry for simulations involving membranes with their edges closer to the tank wall should be considered. Membrane property is specified to be a wall condition in this simulation causing the solver to consider the membrane as one whole surface. A separate mesh study needs to be conducted providing better insights in meshing a membrane with weaved structure. This would allow the liquid to pass through the space between the individual strips. Also, the wall condition causes the membrane to move as a block showing no structural deformation during liquid motion. Further simulations involving coupling of structural solver of ABAQUS with that of STAR-CCM+ would allow for membrane structure deformation during multiphase simulation. Further experiments involving the membrane constrained to railings along the tank wall at different points along its edges would help in studying its efficiency at different tank attitudes. Further study of hybrid membrane concept under micro-gravity conditions with a powerful electromagnet would aid in cementing MAPMD as a viable propellant management device.

REFERENCES

- Abramson, H.N., "The Dynamic Behavior of Liquids in Moving Containers: With Applications to Space Vehicles Technology" NASA SP-106 Southwest Research Institute. 1966.
- Benson, David J., and Paul A. Mason. "Method for CFD Simulation of Propellant Slosh in a Spherical Tank." 2011.
- Bian, X., Perlin, M., Schultz, W. W., & Agarwal, M. (2003). Axisymmetric slosh frequencies of a liquid mass in a circular cylinder. *Physics of Fluids* (1994-present), 15(12), 3659-3664.
- Chatman, Y, Gangadharan, S.N., Schlee, K., Sudermann, J., Walker, C., Ristow, J., Hubert, C., "Mechanical Analog Approach to Parameter Estimation of Lateral Spacecraft Fuel Slosh", 49th AIAA/ ASME/ ASCE/ AHS/ ASC Structures, Structural Dynamics, and Materials Conference, 2008
- Devin Jr, Charles. "Survey of thermal, radiation, and viscous damping of pulsating air bubbles in water." *The Journal of the Acoustical Society of America* 31.12 (1959): 1654-1667.
- Dong, S. X., J. Y. Zhai, Jie-Fang Li, and D. Viehland. "Magnetoelectric effect in Terfenol-D/Pb (Zr, TiO)(3)/mu-metal laminate composites." (2006).
- Gangadharan, S. N. (2003). Parameter Estimation of Spacecraft Nutation Growth Model.
- Ginsburg, Camille M., Clark Reid, and Dmitri A. Sergatskov. "Magnetic Shielding for the Fermilab Vertical Cavity Test Facility." *Applied Superconductivity, IEEE Transactions on* 19.3 (2009): 1419-1422.
- Grayson, Gary D. "Variable-gravity anti-vortex and vapor-ingestion-suppression device." U.S. Patent No. 6,840,275. 11 Jan. 2005.
- Green, S. T., Burkey, R. C., & Sudermann, J. (2010, July). Time Frequency Analysis of Spacecraft Propellant Tank Spinning Slosh. In *46th AIAA/ASME/SAE/ASEE Joint Propulsion Conference & Exhibit* (p. 6978).
- H. Nouri and F. Ravelet. *Introduction à la simulation numérique des écoulements. Application au transfert thermique sur plaque plane avec StarCCM+.* Arts et Metiers ParisTech, 2013.
- Hermann Schlichting and Klaus Gersten. *Boundary-Layer Theory.* Springer, 2000.
- Kanda, Kimio. "Energy dispersive X-ray spectrometer." U.S. Patent No. 5,065,020. 12 Nov. 1991.

- Kynan Maley. Best practices: Volume meshing. CD-adapco - South East Asian Conference, 2012.
- Leuva, Dhawal, "Experimental Investigation and CFD Simulation of Active Damping Mechanism for Propellant Slosh in Spacecraft Launch Systems" (2011). Dissertations and Theses. Paper 91.
- Loads, Propellant Slosh. "NASA Space Vehicle Design Criteria Monograph (Structures)." NASA SP-8009, August 1968.
- Marsell, B., Gangadharan, S.N., Chatman, Y., Sudermann, J., Schlee, K., and Ristow, J., "A CFD Approach to Modeling Spacecraft Fuel Slosh", 47th AIAA Aerospace Sciences Meeting, Orlando, FL, 5-8 Jan. 2009
- Marsell, B., Gangadharan, S., Chatman, Y., & Sudermann, J. (2009, May). Using CFD techniques to predict slosh force frequency and damping rate. In Proceedings of the 50th AIAA/ASME/ASCE/AHS/ASC Structures, Structural Dynamics and Materials Conference, Palm Spring, California (Vol. 22).
- Mikell P. Groover and Emory W. Zimmers. CAD/CAM: Computer-Aided Design and Manufacturing. Prentice Hall, 1984.
- Mouhamad, Malick, et al. "Physicochemical and accelerated aging tests of Metglas 2605SA1 and Metglas 2605HB1 amorphous ribbons for power applications." Magnetics, IEEE Transactions on 47.10 (2011): 3192-3195.
- Neamțu, B. V., Geoffroy, O., Chicinaș, I., & Isnard, O. (2012). AC magnetic properties of the soft magnetic composites based on Supermalloy nanocrystalline powder prepared by mechanical alloying. Materials Science and Engineering: B, 177(9), 661-665.
- Paul G. Tucker. Unsteady Computational Fluid Dynamics in Aeronautics. Springer, 2014.
- Ramsay, Thomas N. "Floating absorber assembly for reduced fuel slosh noise." U.S. Patent No. 8,235,241. 7 Aug. 2012.
- Rosario, L. P., Sivasubramanian, B., Das, S., & Gangadharan, S. (2016.)Active Damping of Fuel Slosh Using a Hybrid Magneto-Active Propellant Management Device. 54th AIAA Aerospace Sciences Meeting, AIAA SciTech, 4-8 January 2016, San Diego, California, USA
- Ryu, Chulsung, Wooseok Seol, and Sangyeop Han. "Ablative baffle for a liquid rocket engine thrust chamber." U.S. Patent No. 7,036,303. 2 May 2006.

- Samal, P. K., and J. B. Terrell. "Mechanical properties improvement of PM 400 series stainless steels via nickel addition." *Metal Powder Report* 56.12 (2001): 28-34.
- Santhanam, Vijay, "Slosh Damping With Floating Magnetoactive Micro-Baffles" (2014). *Dissertations and Theses*. Paper 181.
- Sathya N. Gangadharan, "Parameter Estimation of Spacecraft Nutation Growth Model", H-1/H-4, John F. Kennedy Space Center, 2003.
- Sivasubramanian, B., Rosario, L. P., Krishnappa, S., & Gangadharan, S. (2015). A Hybrid Magneto-active Propellant Management Device for Active Slosh Damping in Spacecraft. In *56th AIAA/ASCE/AHS/ASC Structures, Structural Dynamics, and Materials Conference* (p. 1635).
- Varas, David, Ramón Zaera, and Jorge López-Puente. "Numerical modelling of partially filled aircraft fuel tanks submitted to Hydrodynamic Ram." *Aerospace Science and technology* 16.1 (2012): 19-28
- Vreeburg, J. P. (2005). Spacecraft maneuvers and slosh control. *Control Systems, IEEE*, 25(3), 12-16.
- Wolf, Lance Alan. "Baffle for suppressing slosh in a tank and a tank for incorporating same." U.S. Patent No. 6,220,287. 24 Apr. 2001.

A. Calculation of Logarithmic Decrement and Damping Ratio

Force on Cylinder vs Time plot is taken for the calculation of logarithmic decrement and damping ratio. Slosh peaks after 6 seconds of actuation is accounted for. This sample calculation is taken for Active membrane simulation condition for 175 mm membrane diameter,

- n is the number of peaks
- x_1 is the amplitude of the first peak after 6 seconds
- x_{n+1} is the amplitude of the $(n + 1)^{th}$ peak

Logarithmic decrement between the first and the $(n + 1)^{th}$ peak is defined as:

$$\delta = \frac{1}{n} \ln \left| \frac{x_1}{x_{n+1}} \right|$$

$$\delta = \frac{1}{8} \ln \left| \frac{4.779190967}{0.724592167} \right|$$

$$\delta = 0.02358$$

Calculation of damping ratio ζ (dimensionless):

$$\zeta = \frac{\delta}{\sqrt{4\pi^2 + \delta^2}}$$

$$\zeta = \frac{0.02358}{\sqrt{4 \times 3.14^2 + 0.02358^2}}$$

$$\zeta = 3.75 \times 10^{-2}$$

B. Magnitude of Convergence for Simulation Variables

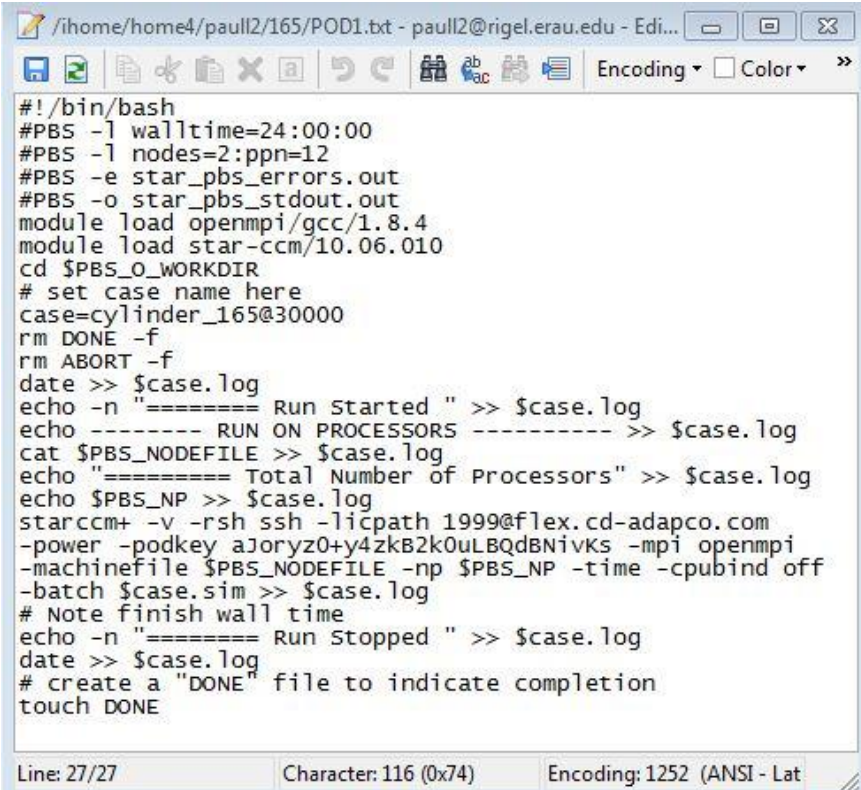
Magnitude of convergence values for variables such as Continuity, Momentum along x, y and z direction, turbulent dissipation rate, Turbulent Kinetic energy and water force on tank are presented in Table 8.1.

Table 8.1 Magnitude of convergence for simulation variables

Cases		Magnitude of convergence						
		Continuity	X-Momentum	Y-Momentum	Z-Momentum	Tke	Tdr	Water
Free Slosh	Low Amplitude	1e-4	1e-3	1e-4	1e-5	1e-3	1e-3	1e-3
	High Amplitude	1e-4	1e-4	1e-4	1e-5	1e-5	1e-4	1e-3
Inactive Membrane (Low Amplitude)	160mm	1e-3	1e-6	1e-6	1e-6	1e-9	1e-12	1e-4
	165mm	1e-3	1e-6	1e-6	1e-6	1e-9	1e-12	1e-4
	170mm	1e-3	1e-3	1e-3	1e-4	1e-4	1e-3	1e-3
	175mm	1e-3	1e-6	1e-6	1e-6	1e-9	1e-12	1e-4
Inactive Membrane (High Amplitude)	160mm	1e-3	1e-6	1e-6	1e-6	1e-9	1e-12	1e-4
	165mm	1e-3	1e-6	1e-6	1e-6	1e-9	1e-12	1e-4
	170mm	1e-3	1e-3	1e-3	1e-4	1e-4	1e-3	1e-3
	175mm	1e-3	1e-6	1e-6	1e-6	1e-9	1e-11	1e-4
Active Membrane (Low Amplitude)	160mm	1e-3	1e-6	1e-6	1e-6	1e-9	1e-12	1e-4
	165mm	1e-3	1e-6	1e-6	1e-6	1e-10	1e-12	1e-4
	170mm	1e-3	1e-3	1e-3	1e-4	1e-4	1e-3	1e-3
	175mm	1e-3	1e-6	1e-6	1e-6	1e-10	1e-12	1e-4
Active Membrane (High Amplitude)	160mm	1e-3	1e-6	1e-6	1e-7	1e-12	1e-12	1e-4
	165mm	1e-3	1e-6	1e-6	1e-7	1e-12	1e-12	1e-4
	170mm	1e-3	1e-3	1e-3	1e-4	1e-4	1e-3	1e-3
	175mm	1e-3	1e-5	1e-5	1e-6	1e-10	1e-12	1e-4

C. High Performance Computing (HPC) at ERAU

Majority of the simulations were run on a High Performance Computing (HPC) Cluster housed on the Daytona Beach campus of Embry-Riddle Aeronautical University. This cluster, Rigel, is comprised of 22 compute nodes, 44 physical CPUs gathering 280 cores. The individual servers composing Rigel are connected via high-speed Infiniband interconnects. This supercomputer has proven to be very useful for resource intensive simulations such as the stationary membrane case and the ones requiring an Overset Mesh. Using the computational power of the cluster directly through Star-CCM+ is possible but another way was preferred during this project. SSH connections were used for shell access and SFTP connections for file transfers –such as uploading the simulation or downloading the results.



```

#!/bin/bash
#PBS -l walltime=24:00:00
#PBS -l nodes=2:ppn=12
#PBS -e star_pbs_errors.out
#PBS -o star_pbs_stdout.out
module load openmpi/gcc/1.8.4
module load star-ccm/10.06.010
cd $PBS_O_WORKDIR
# set case name here
case=cylinder_165@30000
rm DONE -f
rm ABORT -f
date >> $case.log
echo -n "=====  

Run Started " >> $case.log
echo ----- RUN ON PROCESSORS ----- >> $case.log
cat $PBS_NODEFILE >> $case.log
echo "=====  

Total Number of Processors" >> $case.log
echo $PBS_NP >> $case.log
starccm+ -v -rsh ssh -licpath 1999@flex.cd-adapco.com
-power -podkey ajoryz0+y4zkB2k0uLBQdBNivks -mpi openmpi
-machinefile $PBS_NODEFILE -np $PBS_NP -time -cpubind off
-batch $case.sim >> $case.log
# Note finish wall time
echo -n "=====  

Run Stopped " >> $case.log
date >> $case.log
# create a "DONE" file to indicate completion
touch DONE

```

Line: 27/27 Character: 116 (0x74) Encoding: 1252 (ANSI - Lat)

Figure 8.1 Portable Batch System script

In general, a job is submitted simply by running the qsub command for a script file. An example of a typical control file (Portable Batch System script) for Star-CCM+ simulations as shown in Figure 8.1. After submitting a job, its progress and state can be monitored on a Terminal or PuTTY window as seen in Figure 8.2.

```
Console
Enter command: showq
Do not execute commands that require user-input or data transfer
Current directory: /home/home4/paul12/165

/ihome/home4/paul12/165$ qsub POD1.txt
12691.dbschn1.cm.cluster
/ihome/home4/paul12/165$ showq

active jobs-----
JOBID          USERNAME      STATE  PROCS   REMAINING      STARTTIME
12681          coderonm     Running  64     3:39:07  Thu Apr 14 00:20:15
12687          coderonm     Running  64     20:31:45  Thu Apr 14 17:12:53
12689           los         Running  80     22:30:00  Thu Apr 14 19:11:08
12686          coderonm     Running  32     4:21:12:29  Thu Apr 14 17:53:37

4 active jobs          240 of 269 processors in use by local jobs (89.22%)
                        21 of 22 nodes active (95.45%)

eligible jobs-----
JOBID          USERNAME      STATE  PROCS   WCLIMIT      QUEUETIME
12688          krishnk1     Idle    60     1:00:00:00  Thu Apr 14 19:00:21
12691          paul12       Idle    24     1:00:00:00  Thu Apr 14 20:40:28

2 eligible jobs

blocked jobs-----
JOBID          USERNAME      STATE  PROCS   WCLIMIT      QUEUETIME

0 blocked jobs

Total jobs: 6
```

Figure 8.2 Console window terminal